Angular Rate Sensing Using Nonlinear Microresonators Actuated by 2:1 Internal Resonance

by

Atabak Sarrafan

M.Sc., Sharif University of Technology, 2011

B.Sc., Islamic Azad University, 2008

Thesis Submitted in Partial Fulfillment of the
Requirements for the Degree of
Doctor of Philosophy

in the
School of Mechatronic Systems Engineering
Faculty of Applied Sciences

© Atabak Sarrafan 2018

SIMON FRASER UNIVERSITY

Fall 2018

All rights reserved.
However, in accordance with the *Copyright Act of Canada*, this work may be reproduced, without authorization, under the conditions for "Fair Dealing." Therefore, limited reproduction of this work for the purposes of private study, research, criticism, review and news reporting is likely to be in accordance with the law, particularly if cited appropriately.

Approval

Name:	**Atabak Sarrafan**
Degree:	**Doctor of Philosophy**
Title:	***Angular Rate Sensing Using Nonlinear Microresonators Actuated by 2:1 Internal Resonance***
Examining Committee:	**Chair:** **Amr Marzouk** Lecturer

Farid Golnaraghi
Senior Supervisor
Professor

Behraad Bahreyni
Supervisor
Associate Professor

Woo Soo Kim
Supervisor
Associate Professor

Siamak Arzanpour
Internal Examiner
Associate Professor

Joseph Cusumano
External Examiner
Professor
Engineering Science and Mechanics
Pennsylvania State University

Date Defended/Approved: September 28, 2018

Abstract

The goal of this research is to introduce nonlinear microresonator designs that utilize nonlinear modal interaction for application in angular rate sensing. This dissertation specifically looks at the application of nonlinear 2:1 internal resonance, as an actuation mechanism, in micro-electro-mechanical (MEMS) gyroscopes to measure angular input rate. Many MEMS Coriolis vibratory gyroscopes work based on matching the drive- and sense-mode frequencies. The mode-tuning condition cannot be preserved without sophisticated control electronics, due to inevitable fabrication defects and fluctuations in drive parameters. The proposed principle of operation can eliminate the mode-matching requirement in conventional MEMS gyroscopes, and widen the operational frequency region with, ultimately, high flat-top signals. Moreover, it reduces the common problem in MEMS gyroscopes known as cross-coupling by moving the drive mode away from the sense mode of operation.

In this thesis, we suggest and develop two microresonator designs in form of frame-shaped and H-shaped microdevices. The proposed microresonators resembled the nonlinear dynamics of spring-pendulum mechanism with forced and 2:1 internal resonances. The reduced-order modeling software was employed to design and characterize the nonlinear microresonators through comprehensive transient simulations. The simulation results revealed the sensitivity of the microresonators to the angular input rate while probing the 2:1 internal resonance. The designed microresonators were fabricated in a foundary process and tested to investigate the nonlinear modal interaction between the vibrational modes. The lumped mass-spring-damper models of the microdevice with electrostatic actuation and detection mechanism were derived and studied via two-variable expansion perturbation technique. Qualitative agreement between experiments and simulations was confirmed for both microresonators with distinct frequency ratios. Finally, the H-shaped microresonator, with closer frequency ratio to 2:1 and better nonlinear features, was mounted on the rate table for the performance evaluation. The experimental findings implied a full-scale range of sensitivity between 0 to 220 deg sec^{-1}. This work as a proof of concept showed that the output voltage of the microresonator linearly changed with an increase in the applied angular rates. This research proposed an alternative actuation mechanism that can provide new avenues to develop the next generation of nonlinear MEMS gyroscopes.

Keywords: 2:1 internal resonance; Angular rate measurement; MEMS; Microfabrication; Nonlinear mode coupling; Tuning fork structure.

Dedication

To my beloved wife Maria, and my dear parents Mahin and Nasser

Acknowledgments

First and foremost, I would like to express my deepest gratitude and respect to my advisor, Dr. Farid Golnaraghi, for his insightful guidance and continuous support throughout my doctorate studies. I genuinely feel fortunate to have had him as my mentor and advisor. He has been very generous with his knowledge and time and assisted me in each step of my research towards the completion of this dissertation. This work would not have been completed without his patience and foresight.

I would also like to thank Dr. Behraad Bahreyni for his valuable comments and technical recommendations to improve this dissertation. He has always been available and willing to discuss with me, even on his busiest days. He generously granted me to access his lab and equipment for testing and characterization of my devices. I would also like to thank Dr. Woo Soo Kim for his time, support and feedback on this research. I also learned a lot about nano- and micro-fabrication as his student. I would like to extend my most sincere thanks to my internal and external examiners Dr. Siamak Arzanpour and Dr. Joseph Cusumano for their time and invaluable feedback on my work.

I would like to acknowledge my friend and collaborator, Dr. Amr Marzouk, with whom I have shared wonderful memories and moments throughout this research. Special recognition must go to Dr. Soheil Azimi for his friendship and helpful discussions on the electronic side of this research. Also, my special thanks go to my dear friends and colleagues Oldooz Pooyanfar, Navid Noori and Bhargav Gadhavi for their continuous support during ups and downs.

At last but certainly not least, I am deeply indebted to my lovely wife, Maria, and my dear parents, Mahin and Nasser, for their unconditional love, endless support, and constant encouragement in my life and during my Ph.D. program.

Table of Contents

List of Tables

List of Figures

List of Acronyms

AC	Alternating Current
BW	Bandwidth
CC	Clamped Clamped
CF	Clamped Free
CVG	Coriolis Vibratory Gyroscope
DC	Direct Current
DE	Drive Electrode
DOF	Degree of Freedom
DRIE	Deep-Reactive Ion Etching
DPS	Degree Per Second
FEM	Finite Element Method
FTR	Force to Rebalance
IR	Internal Resonance
LIA	Lock-in Amplifier
MEMS	Micro-Electro-Mechanical Systems
MIDIS	MEMS Integrated Design for Inertial Sensors
MSD	Mass Spring Damper
MSEC	Milliseconds
PCB	Printed Circuit Board
PLL	Phase Locked Loop
RF	Radio Frequency
RPS	Radian Per Second
SCS	Single-Crystal Silicon
SE	Sense Electrode
SEC	Second
SEM	Scanning Electron Microscope
SF	Scale Factor
SMA	Standard Male
SOI	Silicon on Insulator
TDSI	Teledyne DALSA Incorporation
TF	Tuning Fork
TSV	Through-Silicon Via

Vpp	Peak-to-Peak Voltage
ZRO	Zero Rate Output

List of Symbols

C_1	Linear damper coefficient
C_2	Linear damper coefficient
C_{t1}	Torsional damper constant
C_{t2}	Torsional damper constant
C_x	Damping factor along the drive axis
C_y	Damping factor along the sense axis
F_1	The electrostatic force produced by drive electrode 1
F_2	The electrostatic force produced by sense electrodes 1 and 3
F_3	The electrostatic force produced by drive electrode 2
F_4	The electrostatic force produced by sense electrodes 2 and 4
F_d	Rayleigh's dissipation force
F_e	Electrostatic force
G	Nonconservative force or momentum
G_{amp}	The gain of pre-amp in lock-in amplifier setting
K	Stiffness
KE	Kinetic energy
K_1	Linear spring coefficient
K_2	Linear spring coefficient
K_{t1}	Torsional spring constant
K_{t2}	Torsional spring constant
K_x	Stiffness coefficient along drive direction
K_y	Stiffness coefficient along sense direction
L	Lagrangian of system
L_e	Length of the equivalent cantilever beam
M	Mass
M_1	Equivalent mass of simply supported beam with a proof mass
M_2	Equivalent mass of simply supported beam with a proof mass
M_b	Equivalent mass of equivalent cantilever beam
P	Output signal power of network analyzer
PE	Potential energy
Q	Mechanical quality factor
V_{AC}	Nondimensional AC voltage

V_{DC}	DC voltage
V_{ac}	AC voltage
V_{dc}	Nondimensional DC voltage
a_1	Nondimensional pendulum-mode amplitude
a_2	Nondimensional spring-mode amplitude
c	Rayleigh's damping coefficient
d	Rayleigh's damping coefficient
f_i	The natural frequency of the i^{th} mode in Hertz
f_x	The natural frequency of drive mode
f_y	The natural frequency of sense mode
g	Electrostatic/capacitive gap
l_0	Unstretched length of linear spring
m_1	Nondimensional mass
p_0	Permittivity of space
q	Generalized coordinate
r_1	Translational motion of mass M_1
r_2	Translational motion of mass M_2
t	Time
t_{si}	The thickness of silicon device layer
x	Translational displacement along drive axis
y	Translational displacement along sense axis
Θ_1	Nondimensional rotation
P_1	Nondimensional displacement
Ω	Nondimensionalizing frequency
Ω_1	Nondimensional excitation frequency
Ω_z	Input angular rate about Z-axis
Ω_{exc}	The frequency of forcing function
Ω_r	The frequency of AC voltage
γ_1	Nondimensional damping factor for spring mode
γ_{t1}	Nondimensional damping factor for pendulum mode
ε	Small dimensionless parameter
ξ	Stretched time variable
η	Slow time variable
θ_1	Rotational motion of masses M_1 and M_b

θ_2	Rotational motion of masses M_2 and M_b
μ_1	Nondimensional damping of spring mode
μ_{t1}	Nondimensional damping of pendulum mode
ρ_1	Nondimensional displacement
ρ_{si}	The mass density of silicon
σ_1	External forcing parameter
σ_2	Detuning parameter
τ	Nondimensional time
φ	Nondimensional input rotation
ψ_1	Nondimensional rotation
ω_1	The nondimensional natural frequency of pendulum mode
ω_2	The nondimensional natural frequency of spring mode
ω_{n_1}	The natural frequency of pendulum mode
ω_{n_2}	The natural frequency of spring mode
ω_{n_3}	The natural frequency of pendulum mode
ω_{n_4}	The natural frequency of spring mode

Chapter 1.

Introduction

1.1. Background

1.1.1. Internal resonance and its applications

Microresonators are the constituent elements of many micro-electro-mechanical systems (MEMS). Their diverse applications range from timing resonators, and radio frequency (RF) filters to various sensors including Coriolis vibratory gyroscopes (CVG) and gravimetric chemical sensors [1]. In most cases, microresonators are designed to work in a linear regime where the sensed output is proportional to driving input. However, unavoidable inherent actuation and structural nonlinearities are of interest in some cases. The presence of nonlinearities in system dynamics may cause nonlinear coupling among the vibrational modes. Nonlinear mode coupling has been recently investigated in micro and nanostructures [2]–[7]. Energy transfer through nonlinear mode coupling has been suggested for several applications, such as energy harvesting [2], mass sensing [8]–[10], and stabilizing oscillation in MEMS resonators for frequency references [11], [12]. One of the primary mechanisms of nonlinear mode coupling is an internal resonance between various modes of vibrations. The internal resonance can occur between vibrational modes of a system either in the same plane [13] or different planes [2], [4] with the ratio of 1:1 [2], 2:1 [4], and 3:1 [3].

The internal resonance phenomenon can serve various useful purposes because of its impressive dynamic properties. It is increasingly used due to its property of suppressing oscillation in a cantilever [14], enhancing the coupling effect in dynamical systems [15], and preventing disaster in a structure-fluid interaction system carrying a cylindrical liquid tank [16]. There is an abundance of theoretical and experimental research papers describing the 2:1 internal resonance in macro-scale systems, including control of flexible structures [17]–[20], pitch and roll modes interactions in ship dynamics [21], rotating machinery [22], cable-stayed bridges [23], energy harvesting systems [2], etc. However, few reports exist on its practical applications to micron-sized devices. To the

best knowledge of the author, use of the internal resonance in MEMS has been limited to band-pass filtering [24], mass sensing [8], and a mechanism to stabilize oscillations [3].

One of the areas which can fall under the umbrella of the 2:1 internal resonance and benefit from its unique characteristics, is the inertial measurement. Inertial measurement is an area where MEMS sensors have gained good acceptance from the market. Micromachined inertial sensors have experienced a continuous performance enhancement. They are increasingly mass produced due to the tremendous demand in many applications such as mobile devices, navigation, homing and control stabilization. Currently, many of the efforts are oriented toward improving precision and accuracy of micromachined gyroscopes, to achieve the performance of fiber-optic and ring laser gyroscopes (inertial grade performance, i.e., sub-degree-per-hour rate resolution and bias stability). These types of gyroscopes are used for the most critical and precision-demanding applications, e.g., military, tactical/inertial navigation and space applications [25]. However, precise fiber-optic and ring laser gyroscopes are all too expensive and too bulky to be used in most engineering applications [26]. Compared to conventional gyroscopes (i.e., fiber-optic and ring laser), MEMS gyroscopes are several orders of magnitude smaller and can be fabricated in large quantities by batch fabrication processes. Nevertheless, the MEMS gyroscopes face challenges due to their conventional actuation mechanism that can be addressed by the nonlinear modal coupling caused by the 2:1 internal resonance. The corresponding issues are explained in the next section.

1.1.2. Operating principle of Coriolis vibratory gyroscopes and challenges

MEMS gyroscopes are micro- or millimeter-scale sensors used to measure the rate of rotation of an object. They have attracted a great deal lot of attention during the last decades due to their small size, low cost, and low power consumption. With revolutionized MEMS technology, extensive research efforts have led to a broad range of gyroscope designs, fabrication and integration techniques. MEMS gyroscopes are extensively employed in numerous applications ranging from ride stabilization and rollover in automotive, consumer electronics such as video-camera stabilization, virtual reality and inertial mouse for computers, robotics applications, and a wide range of military applications [27]. Many existing MEMS gyroscopes operate based on the principle of rotation-induced Coriolis acceleration measurement using a single vibrating proof mass.

The equations of motion of a simplified mass-spring-damper (MSD) model are provided to understand the operational principle of a MEMS gyroscope [28];

$$\begin{cases} M\ddot{x} + C_x\dot{x} + K_x x = F_e + 2M\Omega_z\dot{y} \\ M\ddot{y} + C_y\dot{y} + K_y y = -2M\Omega_z\dot{x} \end{cases} \quad (1.1)$$

where M is the mass of the resonating proof mass; x and y are translational displacements along the drive and sense directions, respectively; C_x and C_y are damping factors; K_x and K_y are stiffness coefficients; F_e is the electrostatic force in the drive direction; and Ω_z is the constant input angular rate about the z-axis, which is orthogonal to the drive and sense axes. The two terms $2M\Omega_z\dot{y}$ and $2M\Omega_z\dot{x}$ are the rotation induced Coriolis forces, which show the coupling between the drive direction and the sense direction. The proof mass is driven at or near the resonant frequency of the drive mode by an external harmonic force. When the gyroscope is subjected to the angular rate Ω_z, a Coriolis force with the same frequency as the driving signal is induced along the sense direction. If the drive and sense natural frequencies match, the maximized coupling Coriolis force excites the system into resonance in the sense direction. The rotation induced motion in the sense direction is proportional to the applied angular rate. Consequently, the input angular velocity can be inferred by measuring the oscillation amplitudes of the proof mass along the sense axis. The resonant frequencies of the sense and drive modes are matched to gain sensitivity of MEMS Coriolis vibratory gyroscopes. Matching natural frequencies amplifies the output of the gyroscope since the Coriolis force causes resonance in the sense mode. This principle of operation is termed as mode matching. Operation of the MEMS vibratory gyroscopes with this condition has proven to be rather challenging.

The inherent tolerances and defects associated with microfabrication technologies, such as lithography, deposition, and etching steps, significantly affect the geometry and dynamic properties of MEMS gyroscopes. As a result, a perfect frequency tuning is not feasible without the implementation of sophisticated control systems. Even in the ideal scenario of a mode-matched system, the vibratory gyroscopes usually confront other difficulties. It is evident that the bandwidth (BW) of the Coriolis vibratory gyroscope reduces as the natural frequencies of the drive and sense modes move towards each other since the Coriolis force acts along the steepest edge of the sense mode response characteristics [28]. This issue is usually handled by keeping the resonance frequencies of the two modes close to each other, but not perfectly tuned. Nevertheless, the MEMS

vibratory gyroscopes operating based on mode-matching or near mode-matching condition are quite sensitive to fluctuations in oscillatory system parameters. A few-Hz of frequency shift between the operating frequency and the sense resonant frequency in a high-quality factor (Q) CVG (with low structural damping) could contribute to a considerable gain drop in the gyroscope output [29]. In practice, this might cause noisy output signals and sensitivity loss of the micro CVG.

The perfect mode matching also results in another significant problem facing micromachined vibratory gyroscopes known as mechanical cross-coupling or crosstalk. In practice, the drive and sense axes of a CVG are not perfectly aligned orthogonal to each other, due to unavoidable tolerances in the fabrication processes. This misalignment introduces the unwanted coupling between the drive and sense modes in the presence of Coriolis coupling. This effect and accompanying mode tuning result in false output response from the sensing mechanism in the absence of a rate input. This response is defined as the zero-rate-output (ZRO) or rate bias of the gyroscope. Misalignment of a driving axis with respect to the predefined drive axis could result in high quadrature signal. The high quadrature signal causes an offset at the gyroscope output, and even it may cause saturation in the readout electronics [28].

1.2. Motivation and objectives

The goal of this research is to introduce nonlinear microresonator designs that utilize nonlinear modal interaction for application in angular rate sensing. In particular, tuning fork microresonator designs exhibiting the nonlinear 2:1 internal resonance (IR) are of interest, and investigated theoretically and experimentally. In such microresonators, the design topology duplicates the nonlinear dynamics of the wellknown spring-pendulum system affected by forced and 2:1 internal resonances. The proposed tuning fork microresonator designs can be thought of demonstration of spring-pendulum systems in MEMS. In these microresonators, the rule of thumb is to allow two desired modes of vibration of the microresonators (a) to be coupled through quadratic nonlinearities, and (b) to be tailored to establish 2:1 frequency ratio between them through adjustment of the structural geometry. The quadratic coupling terms and 2:1 internal resonance in the presence of external forced excitation cause pumping the energy from the higher-frequency mode to the lower-frequency mode. The standard features of such internally

resonant systems with 2:1 frequency ratio are as follow: a) 2:1 frequency ratio between two modes of vibration; b) quadratic nonlinearities couple the two modes; and c) the direct resonant of the mode with higher natural frequency. Fulfillment of these requirements results in energy bridging of much of input mechanical energy from the mode with higher frequency to the one of lower natural frequency. The response of the system with this operating phenomenon can be found at half the excitation frequency. This operational mode can be beneficial in a way to reduce the mechanical cross-coupling or crosstalk between the input and output signal due to the significant separation between input and output frequencies.

In cases where the frequency ratio is quite close to 2:1, this nonlinear characteristic of the device forms almost flat-top resonant frequency curves. These nonlinear resonant curves are somewhat valuable in the MEMS Coriolis vibratory gyroscopes since the idea of employing 2:1 internal resonance in microresonators can eliminate the mode-tuning condition. The flat-top frequency region is defined as the operational region of the gyroscope. Under these conditions, the nonlinear coupling terms will be responsible for facilitating the energy transfer between the drive and sense modes. The proposed nonlinear strategy can be explained using Figure 1.1. This figure illustrates the dynamic response of two types of Coriolis vibratory gyroscopes, (a) mode-matched and (b) desired with 2:1 internal resonance, versus the excitation frequency. The mode matching condition is acquired by matching the resonant frequency of the sense (A) and drive (B) modes. Nevertheless, the fabrication nonidealities and fluctuations in operating conditions result in a frequency shift between the natural frequency of the drive and sense modes (Figure 1.1(a)). This unwanted effect induces the sensitivity loss in the gyroscope output. The issue can be rectified with the use of the nonlinear 2:1 internal resonance in MEMS gyroscopes. This phenomenon in the case of 2:1 frequency ratio between the sense (A) and drive (B) modes, i.e., $f_B \approx 2f_A$, ensures that the resonant frequency of the drive mode (B) lies within the operating region of the sense mode (A). The nominal operation is in the flat part, where the signal gain is relatively high, and the sensitivity of the signal gain to the driving frequency fluctuations is low.

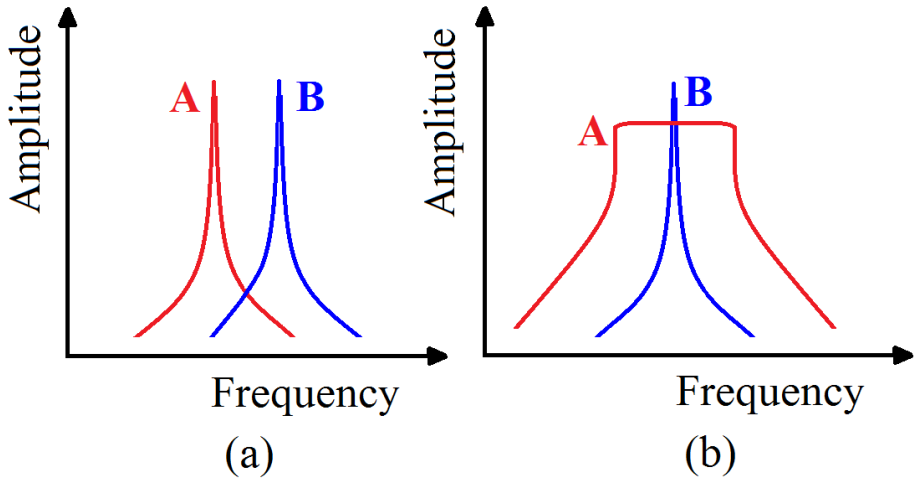

Figure 1.1. Dynamic response of (a) mode-matched and (b) internally resonant 2-DOF vibratory gyroscope in the sense (A) and drive (B) directions.

In this dissertation, the nonlinear dynamics of the tuning fork microresonators are investigated using lumped MSD modeling and two-variable expansion perturbation technique. The microresonator designs are fabricated using a foundry MEMS fabrication process. After successful fabrication of the designed micro-devices, precise characterization techniques and experimental test-beds are exploited to verify and evaluate the operation of the devices in two different operational modes as (a) resonator and (b) angular rate sensor. Nonlinear 2:1 internal resonance is discussed and validated through extensive simulations and experiments. The simulation and experimental results confirm the effectiveness of the 2:1 internal resonance in tuning fork microresonator designs for rotation rate measurement purposes. The microresonators designs employing 2:1 internal resonance can pave the way for the development of nonlinear Coriolis vibratory gyroscopes with (1) no mode matching requirement, (2) large operating region in the sense-mode frequency responses and (3) reduced cross-coupling and mechanical interference between the drive and sense modes.

1.3. Thesis outline

This dissertation is divided into seven chapters as follows:

Chapter 1 gives an introduction to the 2:1 internal resonance and its applications, Coriolis vibratory gyroscopes, and challenges in their principle of operation. Furthermore, the motivation of this thesis is provided.

Chapter 2 presents state-of-the-art on the 2:1 internal resonance in macro- and micro-scaled devices. Moreover, the acquired techniques to overcome mode-tuning condition in Coriolis vibratory gyroscopes are reported.

Chapter 3 focusses on the design topology of feasible micro-devices incorporating nonlinear 2:1 internal resonance. The step-by-step design procedures using the reduced-order model software are explored and exemplified for a MEMS T-beam and two MEMS tuning forks (frame-shaped and H-shaped). The design process in the reduced-order simulation software is followed by linear and nonlinear analysis to obtain natural frequencies, structural mode shapes, nonlinear features, and angular-rate sensing evaluation. Besides the design process, the description of the foundry fabrication technology is described.

Chapter 4 demonstrates the analytical and experimental investigations on the 2:1 internal resonance in the fabricated frame-shaped tuning fork microresonator. A detailed mathematical model of the device is derived. Simulated and experimentally-achieved nonlinear frequency response curves and saturation plots are thoroughly discussed.

Chapter 5 includes a detailed nonlinear analysis on an H-shaped tuning fork microresonator. The steps summarized above for the frame-shaped design are also followed for the H-shaped microdevice analysis.

Chapter 6 describes the experimental test setup to evaluate the performance of the microresonator when subjected to angular input rate. The experimental findings and discussions are also provided in detail.

Chapter 7 summarizes the work in this dissertation and gives conclusions. The chapter concludes with recommendations and perspectives for future work direction.

Chapter 2.

Literature review

Since Sethna [30] reported the internal resonance phenomenon, many researchers have studied various nonlinear macro-sized systems tuned to internal resonance [31]–[36]. For instance, around three decades ago, Haddow et al. [32] studied the effects of nonlinearities inherent in an L-shaped beam configuration when forced at a frequency close to the natural frequencies of the system. The system was assumed to possess two DOFs, and the first two natural frequencies were in the ratio of approximately 2:1. In the mathematical model, the quadratic nonlinearities were retained. The system exhibited saturation effects, the jump phenomenon, and the existence of non-periodic solutions. The internal resonance has also been the subject of research in a broad range of nonlinear systems, including pitch and roll modes interactions in ship dynamics [21], rotating machinery [22], cable-stayed bridges [23], energy harvesting systems [2], etc.

The use of internal resonance and saturation phenomena in nonlinear control has been extensively studied by numerous researchers [37]–[41]. Golnaraghi was one of the first known researchers who utilized IR to control disturbance induced oscillations in a nonlinear system [37]. Golnaraghi [37] and Tuer et al. [42] proposed active control strategies based on internal resonances for controlling the free vibrations of oscillatory systems. They introduced a controller taking the form of a second-order system that was coupled to the plant via quadratic or cubic nonlinear terms. Upon proper tuning of the controller's natural frequency, the nonlinear terms acted as an energy bridge and a state of exchange of energy was established between the plant and the controller, resulting in a beat in the response of the total system. When the controller absorbed most of the plant's energy, a damping mechanism was activated to prevent the energy from returning to the plant. Queini and Golnaraghi [39] implemented this IR control strategy by developing a circuit that emulated the equations of a controller with quadratic coupling terms. This circuit was built with analog electronic components, and it was used to regulate the free vibrations of a DC motor by employing a position feedback mode. The potential of the internal resonance vibration controller has been further explored by Tuer et al. [17], Tuer [43], Duquette et al. [18], and Duquette [44], where the controller was tested on a clamped-free beam. In these studies, attached to the tip of the primary beam (the beam to be controlled)

was a regulated DC (direct current) motor with a second rigid beam/mass configuration attached to the motor shaft at an angle 90° to the primary beam. This configuration gave rise to dynamics nonlinearities, which were necessary for the operation of the controller. The natural frequencies of the system could be altered by adjusting the position gain of the regulator, and therefore, an internal resonance condition could be established. In addition, velocity feedback was used to the regulated DC motor as the artificial damping, which was essential for obtaining the desired transient response. The proposed control technique, in these studies, was unconventional in that the principles of operation were dynamically based [45].

In recent years, researchers have been attracted by exciting features of nonlinear 2:1 internal resonance to exploit them and develop next generation of nonlinear MEMS transducers. A few researchers have reported experimental verification of the internal resonance in MEMS. Samanta et al. [4] exploited a strong nonlinear mode coupling between various vibrational modes to demonstrate experimentally two different types of internal resonances in an atomically thin MoS_2 resonator. Ramini et al. [7] described a systematic experimental approach through electrothermal modulation to tune the ratios among the natural frequencies of a MEMS arch resonator. They also successfully presented the activation of several nonlinear modal interactions due to mainly 2:1 and 3:1 internal resonances as well as veering. Antonio et al. [3] verified experimentally a frequency stabilization mechanism through 3:1 internal resonance. They demonstrated that very low-frequency noise performance was possible in the nonlinear regime. Sarrafan et al. [46] reported on the design and characterization of an H-shaped microresonator exhibiting nonlinear modal interactions due to 2:1 internal resonance. They successfully demonstrated the continuous transfer of energy between two anti-phase orthogonal mode shapes of the microdevice. In another research, Sarrafan et al. [47] designed and characterized a frame-shaped tuning fork microresonator. They experimentally demonstrated even in the presence of fabrication defects, and nonideal frequency ratio, the 2:1 internal resonance could occur in two separate regions of nonlinear frequency response curves.

A few researchers have paid attention to the theoretical study of the nonlinear dynamics of vibrating microresonators with internal resonance. Vyas et al. [48] analyzed the response of a pedal microresonator operating on the principle of nonlinear modal interactions arising due to a 1:2 internal resonance between torsional (an out-of-plane

motion of pedal) and flexural (an in-of-plane motion of pedal) modes. In a similar work, Vyas et al. [24] designed an electrostatically actuated T-beam microresonator operated on the principle of 1:2 ratio internal resonance in which the higher frequency mode auto parametrically excited the lower mode through inertial quadratic and cubic nonlinearities. Hacker and Gottlieb [49] derived a two-field continuum based model for a non-uniform atomic force microscopy micro-cantilever near internal resonance conditions. Moreover, they showed that a step-like heterogeneity in the cantilever longitudinal direction led to states for both 3:1 and 2:1 internal resonances. Souayeh and Kacem [50] investigated the nonlinear dynamics of nanoelectromechanical cantilever arrays due to 3:1 internal resonance using a comprehensive analytical multiphysics model. Gutschmidt and Gottlieb [51] employed a consistent nonlinear continuum model to probe the nonlinear dynamic behavior of an array of *N* nonlinearly coupled microbeams near the array's pull-in point. They showed the region near the pull-in point was governed by several 3:1 internal and combination resonances. Hassanpour et al. [52] addressed the nonlinear dynamics of an internally resonant beam-type MEMS structure due to stretching of the beam excited by attached electrostatic comb-drive actuators. Younis and Nayfeh [53] investigated into the response of a microbeam in case of 3:1 internal resonance condition. They used a nonlinear model to account for the mid-plane stretching, a DC electrostatic force, and an AC harmonic load.

There also have been reports on experimental verification of theoretical models describing the internal resonance in MEMS. Kirkendall et al. [8] demonstrated the use of nonlinear jump phenomena due to internal resonance in harmonically driven quartz crystal resonator operating as a mass sensing paradigm. They modeled the nonlinear behavior of the device through a system of coupled Duffing equations. Van der Avoort et al. [54] described 2:1 internal resonance in a micro dog-bone resonator experimentally and analytically. They studied the limited power handling of the device due to coupling between the in-plane length-extensional resonance mode and one or more out-of-plane bending modes. Daqaq et al. [55] developed a rigorous model of an electrically-actuated torsional micromirror. For a specific voltage range, they observed a 2:1 internal resonance between the first two modes. They believed that due to this internal resonance, the mirror exhibited complex dynamic behavior, which degraded the micromirror's performance. They formulated a simple design rule to avoid this problem.

Although the internal resonance has been noticeably appearing in the literature at a rapid pace, the application of this nonlinear phenomenon in microsystems has remained limited [8], [24], [25]. The 2:1 internal resonance can be more efficiently utilized to enhance the performance of microsensors including MEMS Coriolis vibratory gyroscopes. Gyroscopes have traditionally used the angular momentum stored in a spinning wheel or the Sagnac effect in counterpropagating light beams in ring laser cavity or fiber optic coil [56]. Nowadays, many MEMS rate gyroscopes are based on working principle of the vibrating gyroscope, in which at least two structural modes of vibrations are dynamically coupled through the Coriolis acceleration. Consequently, mechanical energy can be exchanged between fundamental modes of vibration whenever the sensor undergoes a rotation. The IEEE Gyro and Accelerometer panel coined the term Coriolis vibratory gyroscopes (CVGs) to describe such devices [56]. In a CVG, the first mode (drive mode) is excited at its resonant frequency, providing vibrational energy to the whole mechanical structure. When the sensor rotates, the second mode of vibration (sense mode) starts to vibrate because of the Coriolis coupling. By measuring the amplitude of the motion along the secondary mode, it is possible to infer about the angular rate of rotation of the sensor. The sensitivity of the CVG is strictly related to the amplitude of the motion along secondary mode. Therefore, it is necessary to enhance the energy transfer between the primary and secondary modes to gain sensitivity.

Ideally, the sensitivity is maximized when the resonant frequencies of the two structural modes are matched (mode-matching condition). Considering this mode of operation, the system is susceptible to variation in system parameters causing a shift in the resonant frequencies [57]. Under high-quality factor conditions the gain is high; however, the bandwidth is extremely narrow. For example, a 1% fluctuation in frequency matching between the drive and sense modes can produce an error of 20% in the output signal [58]. Since the Coriolis force and the sense mode oscillation amplitude are directly proportional to the drive-mode response, it is desired to enhance the drive-mode amplitude by increasing the Q-factor with vacuum packaging. Increasing a gyroscope's drive-mode Q-factor is also beneficial in such a way that it reduces necessary driving voltages, consequently decreasing contamination of electrical signals by parasitics and improving the sensor power consumption [59]. Nevertheless, the bandwidths of the drive and sense frequency responses become incredibly narrow; leading to much tighter mode-matching requirements and limited bandwidth of angular-rate detection [60].

Attaining a perfect frequency matching during fabrication is rather infeasible because of inherent tolerances and defects associated with manufacturing processes. Moreover, maintaining the frequency matching during the operation of the sensor is very difficult, since parameter fluctuations induced by temperature changes cause additional mistuning. Performance robustness against mistuning can be obtained by enlarging the bandwidth of sense mode, typically by reducing its quality factor (i.e., increasing damping), but this comes at the price of reduced sensitivity, which is not always acceptable [25]. Therefore, to increase the sensitivity of the CVG, it is necessary to optimally design the structure parameters and improve the fabrication process for high mechanical factor (Q-factor) and small difference of resonant frequency between the driving and detecting modes.

Post-processing techniques have been proposed in the literature to reduce mismatching between resonant modes such as controlling process variations more accurately by allowing extra fabrication steps in which polysilicon is selectively deposited [61], [62] or etched [63], laser trimming [64], ion beam milling [65], and softening the spring constant of the secondary structural mode by exploiting local thermal stressing effects [66]. These strategies share the same drawback of requiring, to some extent, a manual intervention, so that are not very suitable for batch fabrications. Moreover, mechanical balancing methods (e.g., ion beam milling and laser trimming) are time-consuming, expensive, and difficult to perform on a small-size MEMS gyroscope [67]. Softening the spring constant of the structural modes also can be implemented by applying different DC bias voltages separately to the drive and sense electrodes to decrease the small mismatch between the resonant frequencies [68]–[70]. However, as the mismatch decreases, the mechanical coupling between the two modes makes the operation more and more unstable [71].

Many researchers have also focused on developing other practical approaches to match the resonant frequencies of the CVGs. One scheme is to design symmetric suspensions for mode-matching and to compensate for temperature-dependent output drift. Even the drive and sense mode frequencies of an asymmetric gyroscope are matched with accurate design, but these matching could not be conserved as the operating temperature varies [68]. Extensive research has been carried out on the design of decoupled and symmetric suspensions and resonator systems for the mode-matching and minimizing temperature dependence [72]–[75]. However, the requirement for mode-

matching is well beyond fabrication tolerances, and none of the symmetric suspension designs can provide a degree of mode-matching without active tuning schemes.

Mode-matching requirements cannot be met without feedback control, even with the symmetric designs under the presence of the mentioned perturbations [75]. Therefore, sophisticated control electronics is required to maintain the operation in the region of the resonance peak. In the past twenty years, many researchers have focused on advanced control electronics to compensate for frequency mismatch between the drive and sense modes [76]–[80]. Sung et al. [77] suggested automatic mode control using PLL-based (phase locked loop) double oscillation loop and tested on a MEMS gyroscope of the parallel-type sensing electrode to automatically tune the resonant frequencies to be identically matched. Antonello et al. [25] presented a mode-matching controller based on an extremum-seeking controller that maximizes the amplitude of sense-mode vibrating motion by adjusting the sense-mode stiffness, which can be implemented by using a few analog electronic components. Different control strategies also have been investigated on mode-matched control of MEMS vibratory gyroscopes such as phase-domain analysis [79], fuzzy sliding mode control [80], digital close control loop [81], adaptive control [67] and on robustness enhancement (i.e., enlarging bandwidth) such as H_∞ control design [82]. It is apparent that utilizing control systems to enhance the performance of a MEMS CVG is unavoidable; however, the small size of the MEMS gyroscopes puts a big challenge on controller design and micro-fabrication [83].

Robustness enhancement against fabrication and operating condition fluctuations is feasible through ensuring that the vibration frequency of the primary mode lies within the bandwidth of the second mode (i.e., enlarging the bandwidth of secondary mode) [25]. The bandwidth enhancement can be achieved by a form of feedback control called force-to-rebalance (FTR) mode of operation.[33], [84], [85]. The FTR allows increasing the bandwidth of the mode-matched gyroscope through maintaining the sense-mode amplitude at zero by applying a rebalancing force which includes Coriolis and quadrature signals [86]. Several classes of MEMS rate gyroscope designs introduced and experimentally demonstrated where the inherent robustness against structural and environmental parameter variation had been achieved structurally [87]–[92]. Accordingly, it is verified that the complexity from the control electronics can be shifted to the structural design of the gyroscope dynamical system [29]. One possible design concept is to design non-resonant multi-degree of freedom (MDOF) of the sense mode oscillatory systems, for

example, 3-DOF design concept aiming to utilize resonance in either the drive mode or the sense mode to improve sensitivity while maintaining the robust operational characteristics [93]. Hence, the flat regions between the peaks of drive or sense modes define the operational frequency region, and resonant frequencies are designed to overlap with the flat operating region. The other feasibility is based on forming multiple drive-mode oscillators, distributed symmetrically around the center of a supporting frame with incrementally spaced resonant frequencies [75]. This design concept provides wider drive-mode bandwidth in vibratory MEMS gyroscopes. There are also different designs allowing interchangeable operation in robust wide-bandwidth and precision mode-matched [87], high-bandwidth highly-sensitive MEMS gyroscope with 2-DOF sense mode [89], and MDOF vibratory gyroscope with double sense-modes [91].

The sensitivity loss due to fabrication imperfections in MEMS gyroscopes based on harmonic oscillators is also overcome by using a nonlinear dynamics phenomenon termed as parametric resonance or parametric amplification [94], [95]. It is an actuation mechanism without the mode-matching requirement. Parametric amplification is a nonlinear effect, due to the modulation of the equivalent spring constants. To generate a parametric resonance response, the actuation force can be produced by a set of non-interdigitated comb fingers [96]. One of the most notable peculiarities of these systems is that large responses can be made even if the excitation frequency is far away from the natural frequency. Using this actuation mechanism, the system can achieve a wide bandwidth of operation without sacrificing the sense mode gain. It offers a robust microsensor that is less sensitive to parameter variations [97], [98], has excellent noise rejection [99]–[101], and even can reduce quadrature error signal which strongly constraints the maximum gain of sensing circuit [99], [100].

In 2015, Marzouk [102] successfully implemented the idea of utilization of 2:1 internal resonance in a macro-scaled T-beam for angular rate sensing. He demonstrated that the output displacement of the resonator linearly changed with an increase in the angular input rate. Motivated by this recent work, this dissertation aims to extend and apply the same idea from macro- to micro-devices. The actuation mechanism can be extremely beneficial in the performance enhancement of Coriolis vibratory gyroscopes in different ways. It can omit frequency matching. Moreover, it generates high, flat-top operational region in the sense-mode frequency response, thus less sensitive to fluctuations in the driving frequency. Finally, it reduces the effect of mechanical interference/cross coupling.

Chapter 3.

Nonlinear microresonator design and fabrication

3.1. Nonlinear 2:1 internal resonance

The mechanical vibrations are classified into several categories according to the relationship between the external forcing frequency and the natural frequencies of the system. In the case where one or more external periodic forcing functions are applied to the system, the vibration is called *forced*. When the frequency of the external force is set at one of the natural frequencies of the system, the oscillation amplitude is maximum. The resonance is referred to as *primary resonance*. Technically, mechanical engineers tend to either avoid primary resonance or exploit it in their systems. When a system has nonlinearities, which exhibit in the equations of motion, the system may resonate at a frequency different from the frequency of the forcing function. One of these resonance situations is called *internal resonance*. It is also known as *auto-parametric resonance* in nonlinear vibrations since the specific relationship between the natural frequencies of the system enforces the system into resonance.

Internal resonance can cause nonlinear modal interactions between the directly excited modes of vibration through external harmonic forcing functions and the indirectly excited modes. This phenomenon exists when the linear natural frequencies of the system are commensurable or nearly commensurable and nonlinear terms couple the structural modes [103]. For example, the equations of motion of a 2-DOF system take the form [104]

$$\begin{cases} \ddot{y} + \gamma_y \dot{y} + \omega_y^2 y = \dot{x}^2 \\ \ddot{x} + \gamma_x \dot{x} + \omega_x^2 x = F\cos(\Omega_{exc} t) + 2\dot{x}\dot{y} \end{cases} \tag{3.1}$$

where $2\dot{x}\dot{y}$ and $\dot{x}^2$ can represent the quadratic Coriolis and centripetal nonlinearities, respectively. If the linear natural frequencies are defined as ω_y and ω_x, internal resonance occurs through quadratic nonlinearities when $\Omega_{exc} \sim \omega_x$ and $\omega_x \sim 2\omega_y$. In this case, the nonlinear quadratic coupling terms cause auto-parametric excitation of the lower-frequency mode by the higher-frequency mode. In other words, it pumps the energy from the mode with higher natural frequency into the mode of lower natural frequency. The

amount of energy that is transferred depends on the type of quadratic nonlinearities, the amplitude of external force, modal Q-factors, the frequency ratio between the vibrational modes, etc. There exists an interesting phenomenon termed *saturation* in internally resonant systems with 2:1 frequency ratio in the presence of quadratic coupling nonlinearities. When the system is excited at a frequency near the higher natural frequency, the structure responds to the frequency of excitation, and the amplitude of the response increases linearly with the amplitude of excitation. However, when the high natural frequency mode reaches a critical value, this mode saturates and all additional energy transfers to the low natural frequency mode. The mode with the lower resonant frequency then starts to oscillate at half the excitation frequency. Many researchers found this nonlinear characteristic interesting and utilized it in the suppression of unwanted oscillations [18], [38], [39].

3.2. Design strategy

The design idea stems from nonlinear dynamics of the classical spring-pendulum system excited by the forced resonance and the 2:1 internal resonance. The schematic of a spring-pendulum system is illustrated below

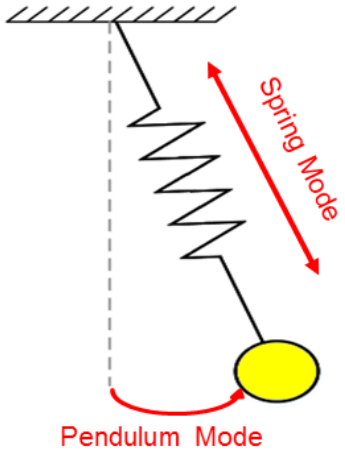

Figure 3.1. Model of the spring-pendulum system.

The dynamics of the system can be considered as the planar motion of a mass attached to the end of a massless linear spring. Assume that a harmonic force $F(t)$ with the frequency of Ω_{exc} is applied to the system along the spring direction. In this system, internal resonance occurs when the requirements for the external and 2:1 internal

resonances are met (i.e., (1) the frequency of the harmonic force $F(t)$ equals the natural frequency of spring extensional mode and (2) the natural frequency of the spring extensional mode is approximately twice as the natural frequency of the angular pendulum mode). Many investigators have studied the nonlinear dynamics and chaotic motions of the spring-pendulum systems excited by external and internal resonances [105], [106].

To design an equivalent structure at micro scale, MEMS design engineers need to explore devices which can couple translational motions (spring mode) with linear natural frequency 2ω to rotational movements (pendulum mode) of linear natural frequency ω. Then, with sufficiently large harmonic driving forces, nonlinear mode coupling occurs, and mechanical energy spills over from the translational mode to the rotational mode. There exists a source of structural nonlinearity in the problem which is the nonlinear coupling between the large radial and angular motions of the spring-pendulum system. In this chapter, three microresonator designs with the same dynamical characteristic as the spring-pendulum system are designed and discussed using reduced-order modeling software, *Architect*™[1] *CoventorWare*©[2].

3.3. Nonlinear analysis via Architect™ CoventorWare©

The simulation of the 2:1 internal resonance phenomenon proved to be a rather significant challenge. The *Architect*™ module in *CoventorWare*© was the only tool could demonstrate the coupling of energy between the modes of the structures in reasonable computation times (i.e., several hours to days). The electromechanical structure of the microresonators is designed using *Architect*™ module in a *CoventorWare*© environment. The *Architect*™ parametric libraries allow system-level designers to simulate and rapidly evaluate multiple design configurations using a top-down, system-level approach. In the following sections, a step-by-step methodology is provided to design and assess nonlinear features and rate sensitivity in three internally resonant microresonator designs.

[1] Architect is a Trademark of Synopsys.

[2] CoventorWare is copyrighted by Coventor Incorporation.

3.3.1. T-beam design

The T-shaped structure has been under increasing focus in recent years, especially as filters, actuators, mass sensors and gyroscopes [24], [48], [107], [108], [102]. The schematic of a T-shaped resonator is shown in Figure 3.2. The T-beam structure comprises two beams: a clamped-clamped (CC) beam whose ends are anchored to fixed supports and a clamped-free (CF) beam attached orthogonally to the middle of the CC beam. This structure possesses a nonlinear behavior due to the presence of quadratic and cubic nonlinearities, arising from its geometry.

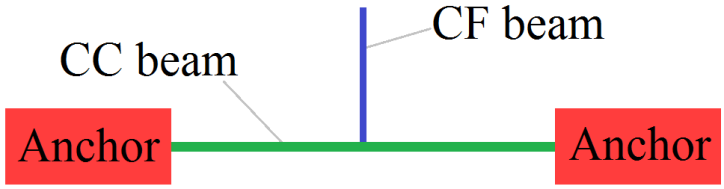

Figure 3.2. Schematic of the T-shaped microresonator.

The high-level schematic of the detailed structural design in Architect™ environment is shown in Figure 3.3(a). The schematic includes three 1-segment nonlinear beams, two beam side electrodes, two anchors, an alternating current (AC) source, a direct current (DC) source, two constrained mechanical bus connectors, an input angular rate function about Z-axis, and a reference frame. The schematic is then processed, and a 3D view of the device is created based on silicon-on-insulator (SOI) process as demonstrated in Figure 3.3(b). The microresonator and the drive electrodes are made of silicon. However, they are pictured with different colors to be distinguishable from each other. The design parameters of the microresonator are presented in Table 3.1, where L_i and w_i are the length and width of the beams, i=CC, and CF; L_d is the length of the drive electrode facing the CC beam, and g is the gap width. The device geometry is adjusted to have the desired natural frequencies in a frequency ratio of 2:1. The drive electrode is biased with DC voltage of 100 V to enhance the linear component of the electrostatic force. The resonator device is excited by the two beam side electrodes through the actuation voltage of $V_{DC}+V_{ac}\sin(\Omega_{exc}t)$, where V_{DC} is the polarization voltage and V_{ac} and Ω_{exc} are the amplitude and frequency of the AC actuation signal, respectively. The resulting motions of the device are captured through two mechanical bus connectors. To speed up the simulation, the translational movement along the Z-axis, and angular

rotations about the X- and Y- axes are grounded in the mechanical bus connectors. The assumption is because the desired modes of the microresonators take place in the X-Y plane. Small-signal frequency analysis is performed to achieve the natural frequencies and structural mode shapes of the microdevice, depicted in Figure 3.4. The natural frequencies can be found at f_1 =1.4145 MHz (pendulum mode) and f_2 =2.8419 MHz (spring mode). The pendulum mode describes the angular rotation of the CF beam tip about the Z-axis, and the spring mode is associated with the translational displacement of the middle of the CC beam along the Y-axis. Based on the AC analysis, the frequency ratio can be computed as f_2/f_1 =2.0091.

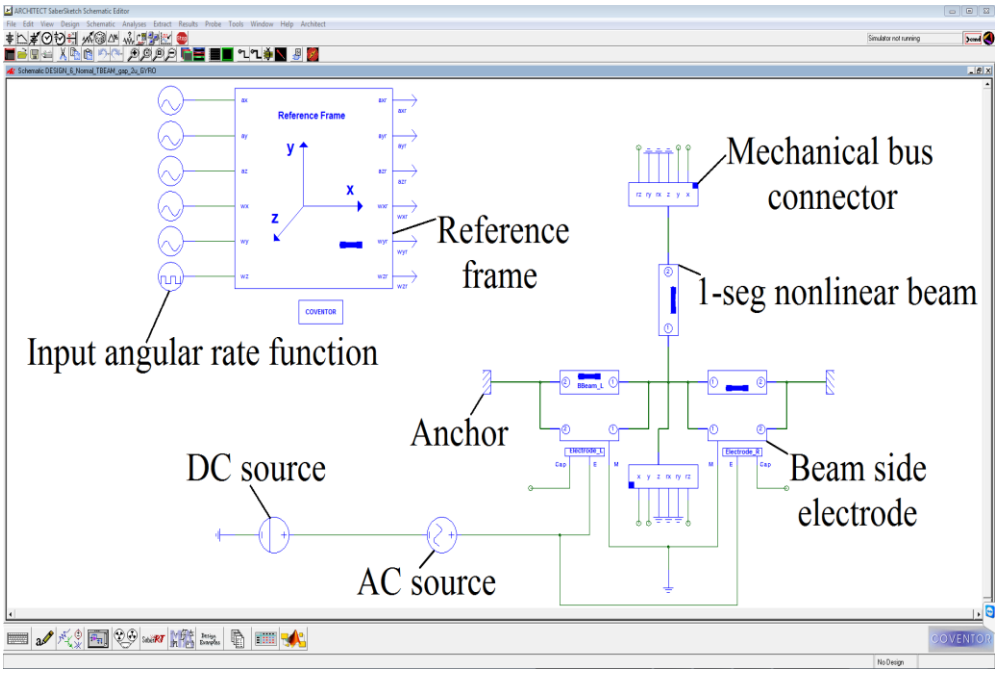

(a)

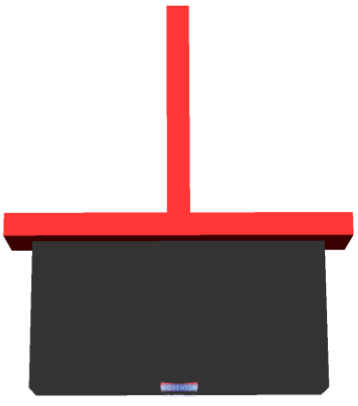

(b)

Figure 3.3. (a) Complete system schematic of the T-shaped microresonator in CoventorWare© Architect™, (b) 3D view of the built model in Architect™ Scence3D.

Table 3.1. The T-beam design dimensions in Architect™ schematic.

Symbol	Value (μm)
L_{CC}	120
w_{CC}	8
L_{CF}	80
w_{CF}	8
L_d	100
g	2

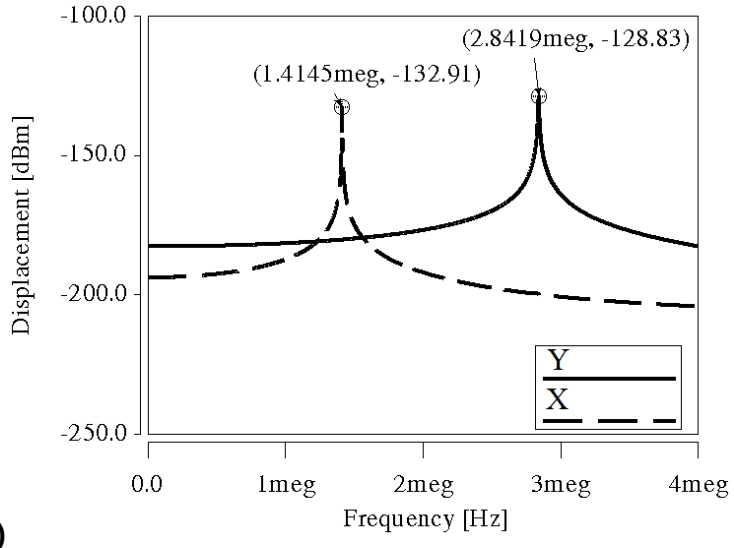

(a)

(b)

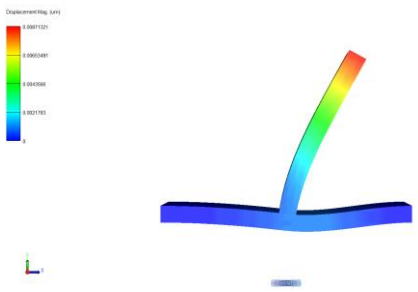

(c)

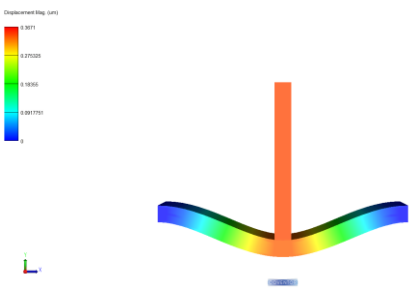

Figure 3.4. (a) Modal analysis of the T-beam microresonator simulated using Architect™. (b) The pendulum mode shape with natural frequency 1.4145 MHz. (c) The spring mode shape with natural frequency 2.8419 MHz. (blue-no displacement and red-maximum displacement)

Comprehensive transient simulations are carried out to probe the nonlinear characteristics of the T-beam microdevice. To reduce the time required for each transient simulation, the Q-factors of the desired modes are needed to be artificially set at low

values to complete the simulation in reasonable times. The Q-factors for the pendulum and spring modes are set at 1000 and 500, respectively. Using low Q-factors requires the application of larger drive voltages to reach the minimum displacement threshold to trigger the 2:1 internal resonance. The Rayleigh's damping method is employed to specify the Q-factors above in the transient simulations (a=52.39, b=1.12×10^{-10}). Trapezoidal integration method is selected with truncation error of 0.001 in the transient simulation settings. Each simulation run on a personal computer with an Intel Core i5-3450 processor and 16GB of RAM took about 3 hours to reach steady-state, corresponding to one pair of data points in Figure 3.5(a) and Figure 3.6 (i.e., the data in Figure 3.6 required 3×16×3=144 hours of calculations besides the time needed to update the parameters in between steps).

Figure 3.5(a) exhibits the steady-state amplitudes of the spring mode (Y) and the pendulum mode (X) versus various driving voltages V_{ac}=0-50 V, where V_{DC}=100 V and Ω_{exc}=2f_1≈2.8292 MHz. It should be mentioned that the amplitudes X and Y are collected from the x and y output ports of the mechanical bus connectors attached to the tip of the CF beam and the middle of the CC beam, respectively. From this figure, it can be noticed that the amplitude of the spring mode (Y) increases linearly with the changes in the drive voltages V_{ac}. However, the amplitude of the pendulum mode is zero. When the drive voltage reaches the critical threshold value (V_{ac}~22.5 V), the amplitude Y saturates, and all excess of energy pumps into the amplitude X. This observation confirms the occurrence of the saturation phenomenon in which much of the input or excitation energy transfer from the higher frequency mode (spring mode) to the lower frequency mode (pendulum mode). Figure 3.5(b) demonstrates the time-domain responses of the spring-mode (Y) and the pendulum-mode (X) amplitudes associated with region ***A*** in Figure 3.5(a), where the loading setting is as follows; V_{DC}=100 V, V_{ac}=30 V and Ω_{exc}=2f_1≈2.8292 MHz. The figure shows that the mode with lower frequency (pendulum-mode) starts to pick up energy from the higher frequency mode after around 1 msec, confirming the nonlinear mode coupling.

The simulated nonlinear frequency response curves of the spring (Y) and the pendulum (X) modal amplitudes for different actuation levels are exhibited in Figure 3.6. This figure is achieved by saving the steady-state amplitude of the signals (X and Y), while the excitation frequency Ω_{exc} is swept around the natural frequency of the spring mode f_2. The figure discloses that the spring mode (Y) resonates at the frequency of excitation Ω_{exc}, while the pendulum mode (X) responds at half the excitation frequency Ω_{exc}/2, i.e., in the vicinity of the pendulum resonant frequency f_1. Furthermore, it reveals the transfer of

energy between the vibrational modes due to nonlinear mode coupling and generating broad operational region in the pendulum-resonant curves.

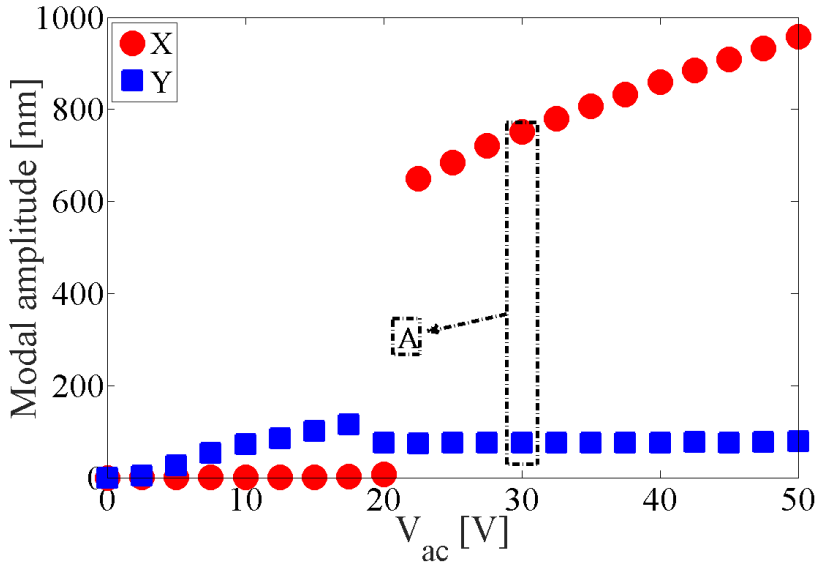

(a)

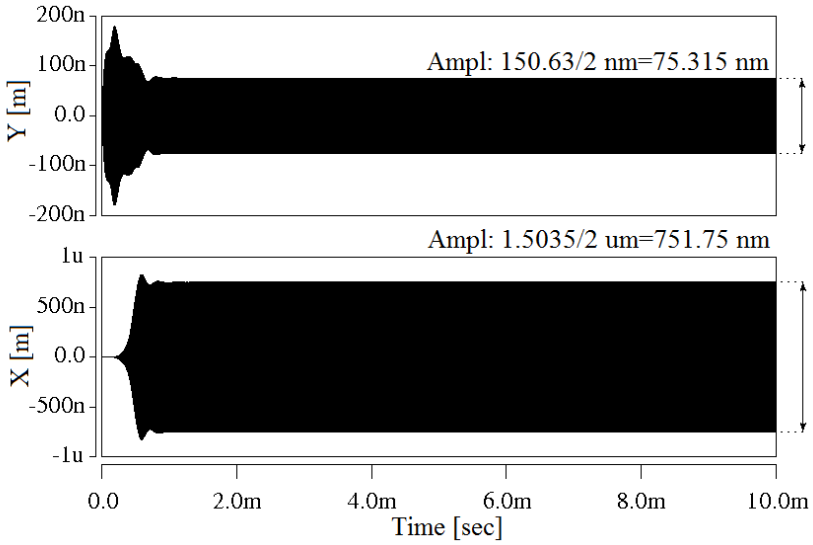

(b)

Figure 3.5. Transient simulation results obtained using Architect™ for the T-beam microresonator, where V_{DC}=100 V and Ω_{exc}=2.8292 MHz. (a) the steady-state modal amplitudes of X and Y extracted from repeated transient simulations for V_{ac}=[0 50] V. (b) the oscillation amplitudes of the spring-mode (*Y*) and the pendulum-mode (*X*) for region *A* corresponding to V_{ac}=30 V.

These nonlinear characteristics of the microresonator (i.e., the pendulum mode with the wide operational region and high-amplitude resonant curves) can be exploited

efficiently to reduce the sensitivity of MEMS CVGs to fluctuations in the drive frequency. It is also noteworthy that the effect of mechanical cross-coupling/mechanical interference can be reduced since the pendulum natural frequency is away from the spring natural frequency (i.e., $f_2 \approx 2f_1$). The observation is despite the fact in mode-matched CVGs, where the sense mode is forced to resonate at the natural frequency of the drive-mode or the excitation frequency. Figure 3.6 also implies that an increase in the voltage V_{ac} can enlarge and control the operational region over which the pendulum-mode participates in the modal interactions. Although, significant AC levels might cause pull-in effect and functionality loss.

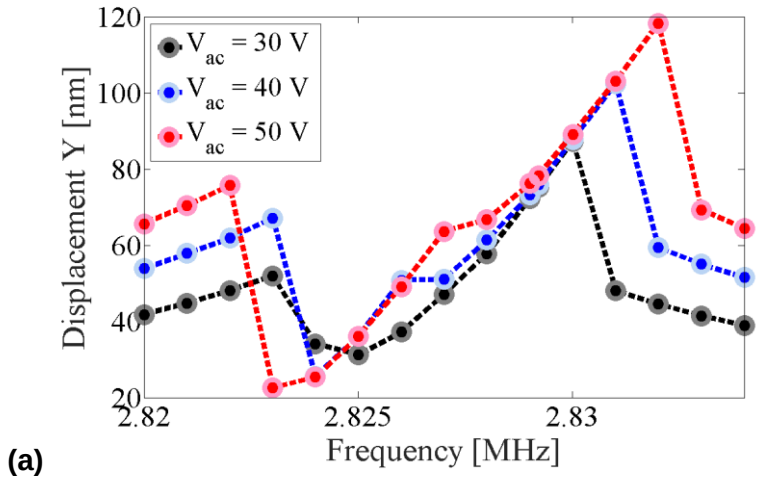

(a)

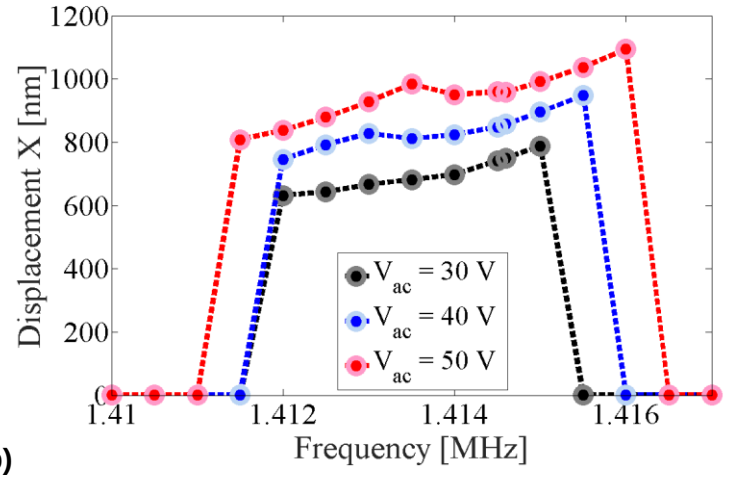

(b)

Figure 3.6. Simulated nonlinear frequency response curves for the T-beam microresonator achieved via Architect™ (a) the spring mode and (b) the pendulum mode.

As seen from the transient simulations, the T-beam microresonator is capable of exhibiting the nonlinear mode coupling between the so-called extensional spring and rotational pendulum modes. The following step is to analyze the dynamic response of the microresonator when exposed to the angular input rate along the Z-axis. The microresonator is excited through the drive electrode with V_{DC}=100 V, V_{ac}=25 V and $\Omega_{exc}=2f_1$~2.8292 MHz. The input rate profile is defined as a ramp function with 5-msec delay and a constant angular acceleration of 1910 deg/sec^2. Consideration of the time delay in the profile is essential to let the system settle at steady state after the modal interactions. The implementation of such a high-angular acceleration (i.e., 1910 deg/sec^2) seems to be infeasible in an experiment with available commercialized rate tables in the market. Nevertheless, setting smaller values for the angular acceleration in the simulations will be incredibly tedious, especially when it comes to the application of the high angular rates. This is because the simulations need more time to settle and reach steady-state condition.

To observe the effect of the angular input rate on the output signals (*X* and *Y* amplitudes), tighter condition on truncation error setting in Architect™ is required. The truncation error needed to be reduced to 0.00001. This value is much smaller than the previous value for the calculation error, i.e., 0.001. Consequently, the simulation time significantly increases in this state of analysis. Figure 3.7 depicts the dynamical behavior of the microresonator as subjected to the angular velocity Ω_z =±1.5 rad sec^{-1} (RPS) (or ±86 deg sec^{-1} (DPS)). The amplitudes along the spring (*Y*) and pendulum (*X*) modes before and after application of the angular velocity can be seen in Figure 3.7(a) and Figure 3.7(b). As it can be found out from the figure, the input rate is effective after 5 msec of delay in the ramp function. The envelope of the spring and pendulum modal amplitudes (X and Y signals) grow with an increase in the angular rate. Once the rotational velocity ends up at the target value and stays for 10 msec, the modal amplitudes become steady. The signal amplitudes before and after the input rate were taken in the time interval [4 5] and [75 80] milliseconds (msec), respectively. It is worth mentioning that the excitation frequency of the microresonator can be chosen from any frequency values in the operational region of the pendulum mode (wide-bandwidth resonant area) depending on the AC driving levels V_{ac}.

The full range of the microresonator sensitivity to the rate Ω_Z= [-200 200] DPS (or [-3.5 3.5] RPS) is shown in Figure 3.8. The spring and pendulum modal amplitudes linearly

change by further application of the angular input rate until the microresonator sensitivity reaches its upper limit for the angular rates greater than ±143 DPS. The non-zero bias in the signals (*X* and *Y*) corresponds to the oscillation generated by the nonlinear mode coupling due to the 2:1 internal resonance.

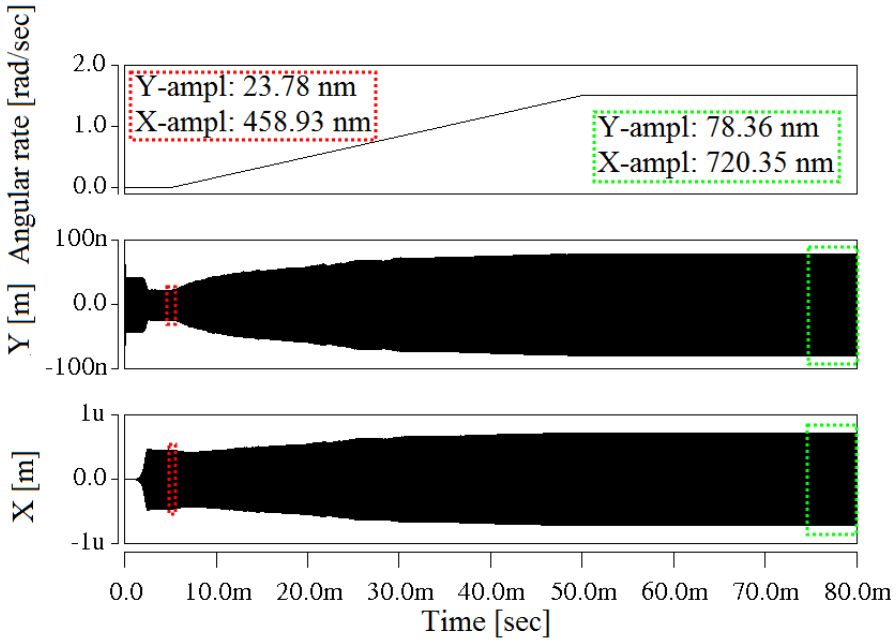

(a)

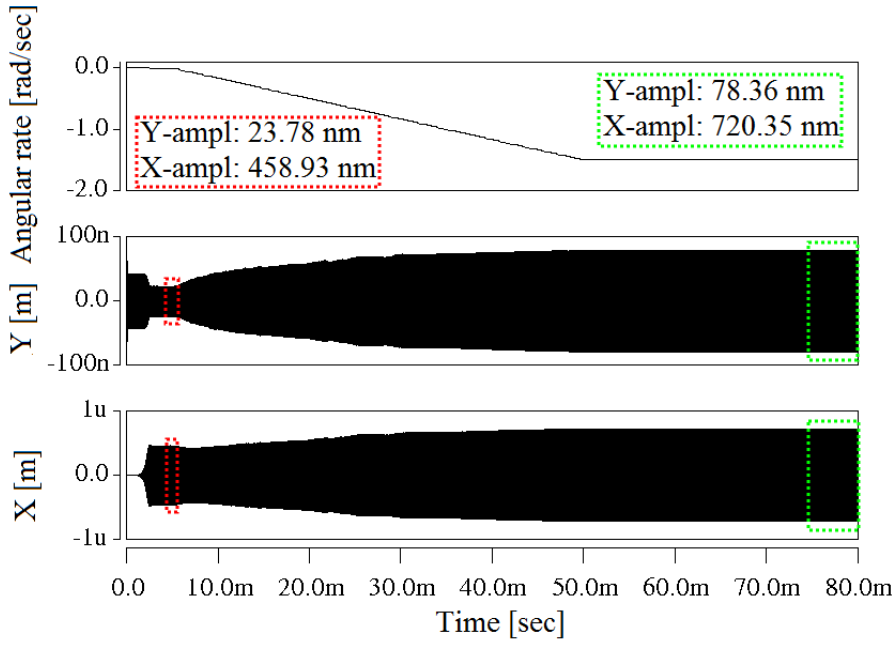

(b)

Figure 3.7. Time-domain analysis (Architect™) for the T-beam microresonator, when the applied angular velocity Ω_Z equals to (a) 1.5 RPS (or 86 DPS) and (b) -1.5 RPS (or -86 DPS).

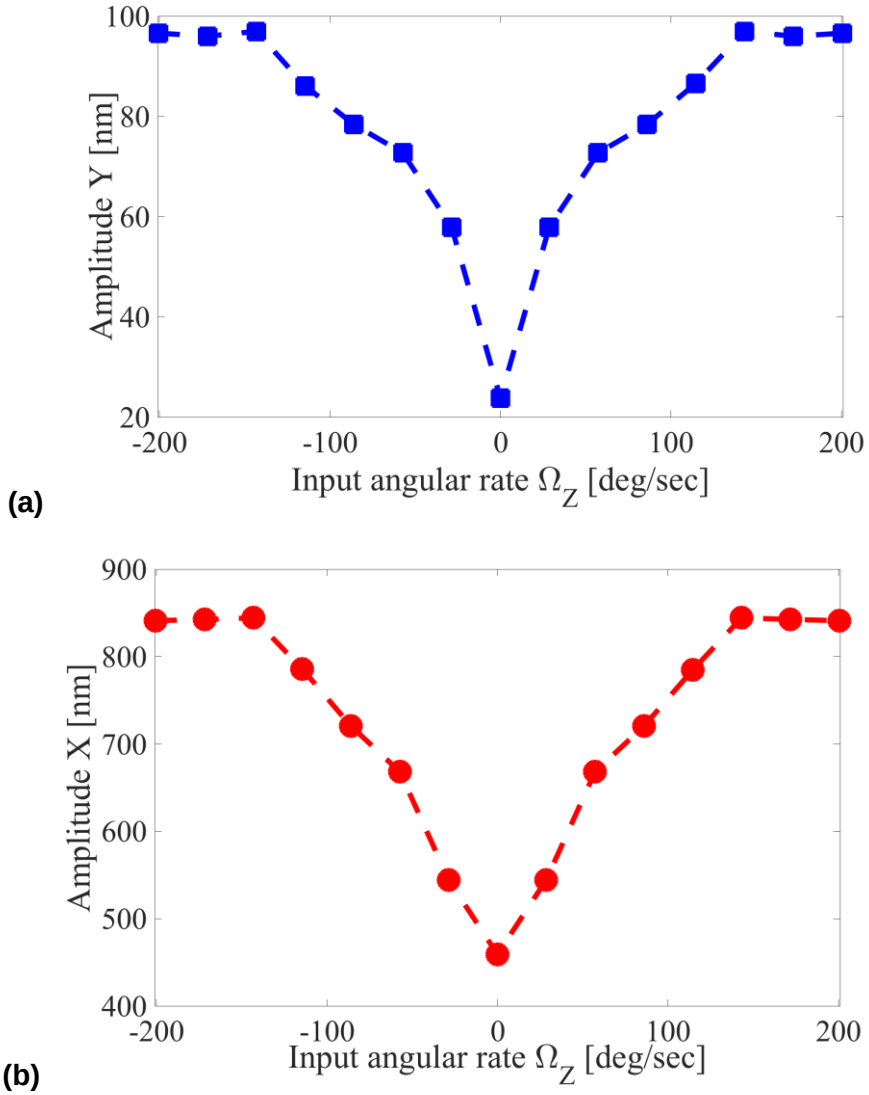

Figure 3.8. Simulated sensitivity plots acquired using Architect™ for the T-beam microresonator, when exposed to the input rate Ω_Z = [-200 200] DPS. (a) the spring mode and (b) the pendulum mode.

3.3.2. Frame-shaped tuning fork design

Despite the easy fabrication and ability to be driven deep into the nonlinear regime, the T-shaped microresonator design is not considered as a suitable candidate for MEMS Coriolis vibratory gyroscope applications. The reasons are as follows;

- Asymmetric structure design.
- Sensitivity to fabrication process since a slight change in the geometry of the CC and CF beams will significantly detune the frequency ratio from 2:1.

- Any small disturbance applied to the CC beam will result in generation of unwanted oscillations in the CF beam.
- Low structural mass when compared to tuning fork (TF) designs.

Considering these decisive factors brings up dual-mass tuning fork designs with anti-phase resonant modes to our attention. The dual-mass tuning fork designs are well known to be relatively immune to vibration because of their differential operation and common-mode rejection [109]. Beside all these, for our purpose, they can dynamically act as the spring-pendulum mechanism to facilitate the nonlinear modal interactions as explained in the following sections. The schematic of the TF microdevice is illustrated in Figure 3.9. This design has two identical two-DOF resonators labeled as the left and the right resonator, Figure 3.9(a). Each resonator is free to move in the X-Y plane. The device comprises two identical proof masses which are connected to the two vertices of T-shape like linkage, and the center bar of the T-shape linkage is attached to the anchor. The proof masses are supported by some flexural beam springs and centrally anchored. The flexural beam suspensions include the anchor beams (from the anchor to the base beam), the base beams (connecting two parallel tuning fork beams), and the tuning fork beams (from the proof mass to the base beam). The microdevice is surrounded by a collection of symmetrically distributed parallel plate electrodes. The system has two drive electrodes (DE) to load the device into resonance. The vibration sensing system has four sensing electrodes (SE) to detect the oscillations. The design parameters in Figure 3.9(b) are explained in Table 3.2.

The proof masses can move in either opposite directions (tuning fork mode) or together in the same direction (the hula mode) along the X- and Y-axes. The dimension of the tuning fork beams and the anchor beams mostly determine the natural frequency of the tuning fork mode or the hula mode along the X-direction. The natural frequency of the tuning fork mode (or the hula mode) along the Y-axis depends on the geometry of the base beams and the anchor beams. With tuning fork mode of operation, the proof masses move in opposite directions, i.e., 180° phase difference with respect to each other. Therefore, the base beams remain essentially static and only small shear stresses are transmitted through the anchor to the substrate [110]. If the anchor beams are thick and rigid, the masses move independently. The topology forms a mechanically decoupled resonator design. In the linear regime, where the driving level is below a specific threshold, the motion of the proof masses along the Y-axis is assumed to be translational. Practically,

driving the device deep into nonlinear regime can induce large deformations of the base and tuning fork beams, causing rotation of the proof masses about the center of the anchor [111]. As a result, the masses can undergo rotational motion around the anchor while they can also experience translational movement in the tuning fork mode or the hula mode along the X-direction. From a theoretical point of view, this resembles the classical mechanical system of the spring-pendulum mechanism. The translational mode (hula or tuning fork) along the X-axis can be considered as the spring mode, and the rotational mode of the proof masses about the anchor (hula or tuning fork) can be evaluated as the pendulum mode. Overall, the dynamic of the microresonator, in case of nonlinear operation, is equivalent to the dynamics of two decoupled spring-pendulum systems.

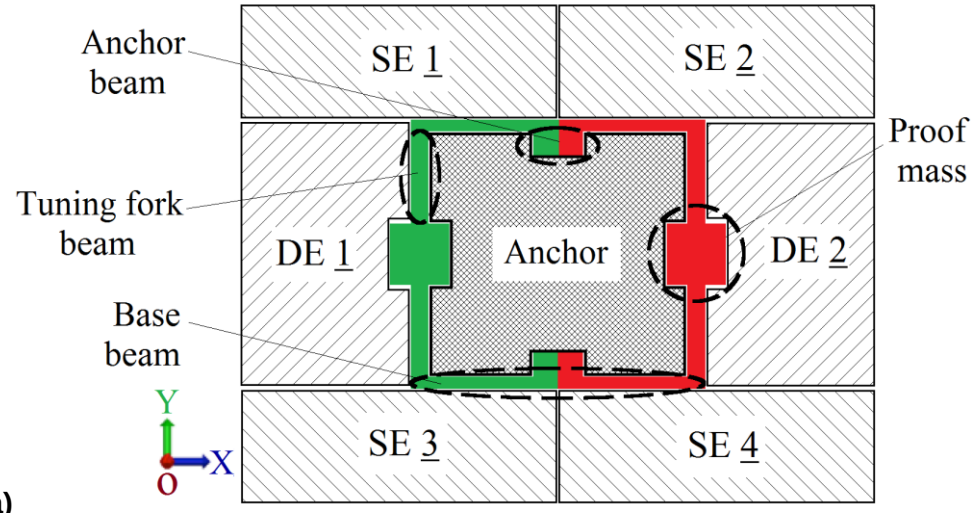

(a)

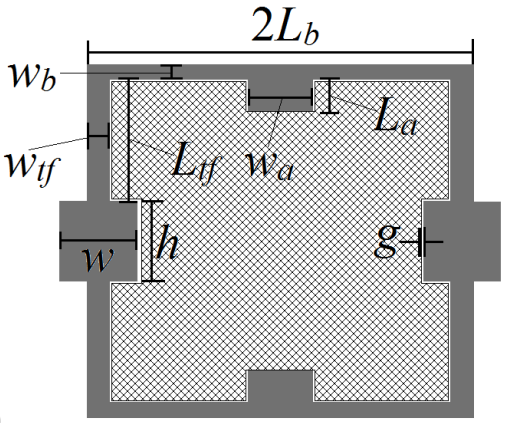

(b)

Figure 3.9. Schematic diagram of the frame-shaped tuning fork microresonator; (a) Outline of the device. (b) The TF design parameters. In part (b), solid gray is the moveable device. Electrical contact pads are an anchor, sense electrodes (SE) 1-4 and drive electrodes (DE) 1 and 2.

Table 3.2. Design parameters of the frame-shaped tuning fork microresonator.

Symbol	Quantity
L_a	The length of the anchor beam
w_a	The width of the anchor beam
L_b	The length of the base beam
w_b	The width of the base beam
L_{tf}	The length of the tuning fork beam
w_{tf}	The width of the tuning fork beam
w	The width of the proof mass
h	The height of the proof mass
g	The electrostatic gap

The nonlinear characteristics and rate sensitivity of the frame-shaped TF microresonator are explored through comprehensive transient simulations in Architect™. The electromechanical model of the microresonator is formed by connecting multiple mechanical and electrical elements as illustrated in Figure 3.10. The schematic consists of ten 1-seg nonlinear beams, four beam side electrodes, two nonlinear rigid plates, two rigid plate side electrodes, eight constrained mechanical bus connectors, two anchors, an AC voltage source, a DC voltage source, a fixed reference frame and an input angular rate function along the Z-axis. Figure 3.10(b) shows the 3D model of the schematic, which is built based on MEMS Integrated Design for Inertial Sensors (MIDIS) process design kit [112]. This fabrication technology offers a minimum feature size of 1.5 μm for the device layer and vacuum-encapsulated silicon devices. These features of the manufacturing process are of great importance in this research because the 2:1 internal resonance can be probed by producing large electrostatic drive forces with 1.5 μm of the electrostatic gap. Moreover, the experiments can be accomplished without the need to use a vacuum chamber and pumping system. The MIDIS process is thoroughly described at the end of this chapter. The adjusted dimension of the microresonator can be found in Table 3.3. In this table, L_s is the length of the SE facing the base beam and L_d is the length of the DE facing the proof mass. The geometry of the microresonator is determined by a trial and error process to tailor the natural frequency of the modes of interest to be in a 2:1 frequency ratio. The drive and sense electrodes are biased at 90 V using the DC voltage source. The electrostatic drive forces are inserted into the microresonator structure through DE 1 and DE 2, which are provided with in-phase AC voltages.

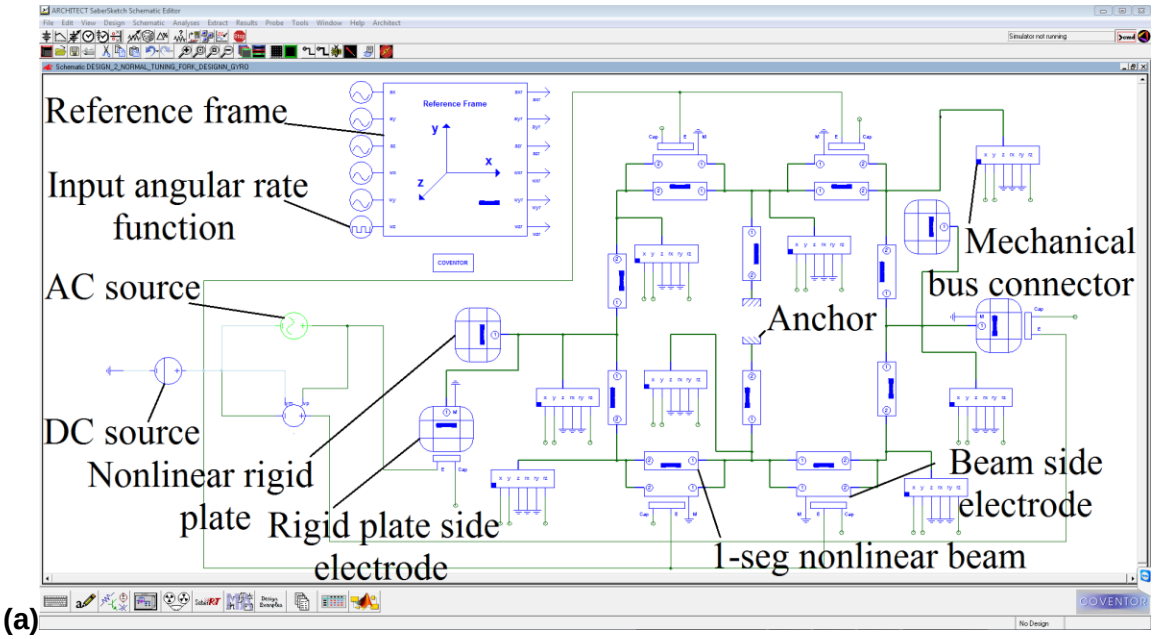

(a)

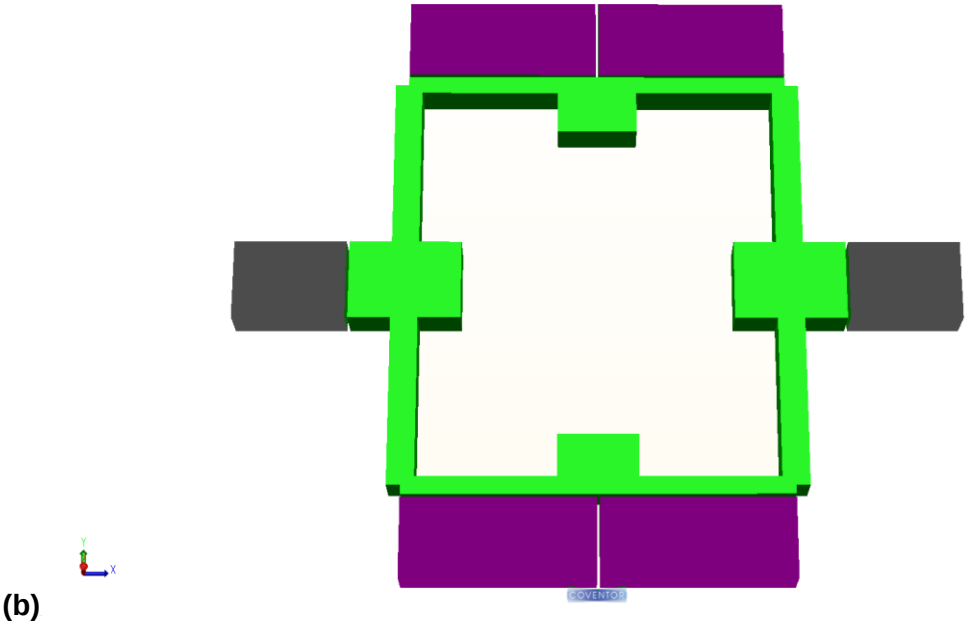

(b)

Figure 3.10. (a) Complete system schematic of the frame-shaped microresonator in CoventorWare© Architect™, (b) 3D view of the built model in Architect™ Scence3D.

The resulting oscillations induced by the nonlinear modal interactions are measured through SE 1-4 and output ports of the mechanical bus connectors. The mechanical bus connectors give the translational and angular motions of the pinned junctions along the X-, Y- and Z-axes in meter and radian, respectively. As it can be noticed from the schematic, some of the output ports of the mechanical bus connectors

are grounded. According to the author's experience, this is a crucial step to speed up the transient simulations in the nonlinear analysis. Using the nonlinear elements for nonlinear vibration investigations is unavoidable. The nonlinear elements in Architect™ library can handle large displacements generated by large electrostatic and Coriolis forces. Nevertheless, they add to the complexity of the problem. If the planar structural modes are desirable, the unused ports in the mechanical bus connectors (displacements and rotations) can be safely grounded.

Table 3.3. The frame-shaped design dimensions in Architect™ schematic.

Symbol	Value (μm)
L_a	26.5
w_a	50
L_b	240
w_b	11
L_{tf}	102
w_{tf}	17
w	70
h	50
g	1.75
L_s	119
L_d	50

The natural frequencies and corresponding mode shapes of the microresonator are acquired through small-signal frequency analysis, Figure 3.11. Here, the pendulum mode is defined as the anti-phase oscillation of the proof masses along the Y-axis, Figure 3.11(b), and the spring mode is an anti-phase oscillation of the proof masses along the X-axis, Figure 3.11(c). The natural frequency of the pendulum and spring modes are, respectively, as follow; f_1 =519.5 kHz, f_2 =1.0438 MHz, and the frequency ratio f_2/f_1 =2.0092. The Q-factors of the pendulum and spring modes are considered to be 1000 and 500, respectively. Rayleigh's damping approach is employed to enter the pendulum and spring-mode Q-factors into the transient analysis setting (a=20.28, b=3.04×10^{-10}). Trapezoidal integration method is set with truncation error of 0.001 to solve the reduced-order equations. Each simulation run on a personal computer with an Intel Core i5-3450 processor and 16GB of RAM took about 10 hours to reach steady-state, corresponding to one pair of data points in Figure 3.12 or Figure 3.13 (i.e., the data in Figure 3.13 required 3×22×10=660 hours of calculations in addition to the time needed to update the

parameters in between steps). Although the nonlinear analysis in Architect™ is time-consuming, it will be shown in the following chapters that it can predict the nonlinear properties of the microresonators to an acceptable degree.

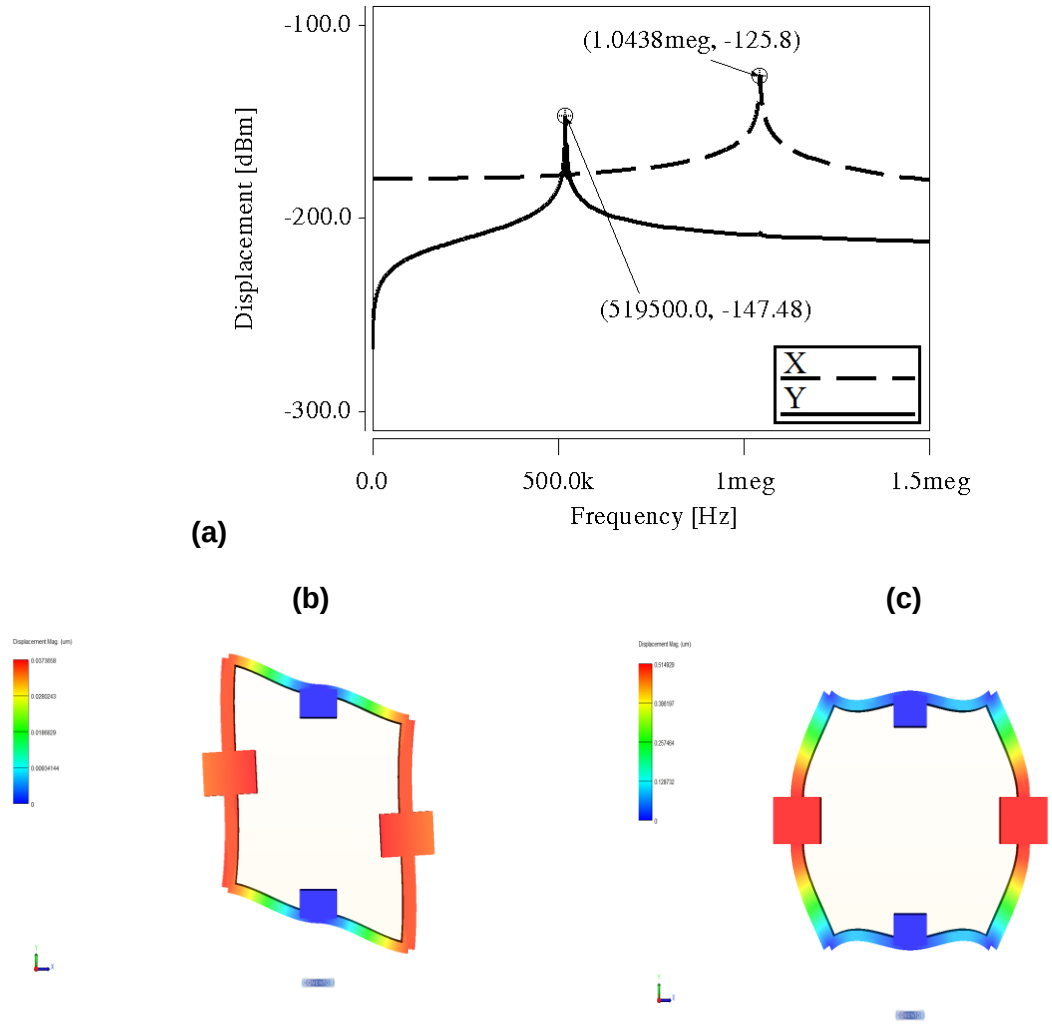

Figure 3.11. (a) Modal analysis of the frame-shaped microresonator simulated using Architect™. (b) The pendulum mode shape with natural frequency 519.5 kHz. (c) The spring mode shape with natural frequency 1.0438 MHz. (blue-no displacement and red-maximum displacement)

The steady-state amplitudes of the pendulum-mode (*Y*) and the spring mode (*X*) as a function of the AC actuation voltages V_{ac} are exhibited in Figure 3.12(a). This figure is obtained when the AC voltage is swept from 0-50 V, and the excitation frequency is set at Ω_{exc}=1.0388 MHz. For each data point in the figure, the steady-state amplitudes of the vibrational modes (*X* and *Y*) are captured for each AC drive voltage. It can be observed

that the saturation phenomenon occurs in this nonlinear system. Because, the spring-mode amplitude (X) proportionally changes with the rise in the value of AC voltage, while the spring-mode amplitude (Y) remains constant at zero. As the AC voltage reaches a specific threshold, i.e., V_{ac} =25 V, the pendulum response starts growing. For a better understanding of the nonlinear mode coupling, the case where V_{ac}=30 V is separately demonstrated in Figure 3.12(b). It implies that there is an energy channeling between the spring mode of amplitude X and the pendulum mode with amplitude Y after about approximately 13 msec.

The nonlinear frequency resonant curves of the microresonator are achieved by sweeping the excitation frequency Ω_{exc} in the neighborhood of the higher-mode resonant frequency (spring mode with the natural frequency f_2). The simulated resonant curves are shown in Figure 3.13. The data points in this figure are the steady-state amplitudes of the pendulum and spring modes for the AC voltages V_{ac}=30, 40 and 50 V. The results indicate that the mode with lower frequency (pendulum mode) resonates at half the excitation frequency ($\Omega_{exc}/2$) and the higher-frequency mode (spring mode) responds at the excitation frequency (Ω_{exc}). As it can be understood from Figure 3.13(b), a rise in the actuation voltage V_{ac} can significantly enlarge the operational region of the pendulum mode. This point can be verified by looking at the nonlinear resonant curves for the case of V_{ac}=30 V and V_{ac}=50 V. Similar to the T-shaped microresonator, the frame-shaped TF microresonator can be considered as a candidate to be utilized as the rate sensor incorporating the 2:1 internal resonance. It can produce the nonlinear resonant frequency curves with high gain, and wide operational region in the pendulum mode.

The dynamical behavior of the microresonator is investigated as the device undergoes rotation along the Z-axis. For the same transient simulation setting (i.e., truncation error=0.001), the sensitivity of the microresonator is not figured. Truncation error has to be specified as 0.00001 to resolve this issue. This error setting and a large number of the nonlinear mechanical elements in Architect™ schematic justify the long hours of simulation for the case of angular sensitivity analysis. A ramp function with the slope of 1910 deg/sec^2 is exerted on the microresonator. This rate profile is set up for the microresonator when it experiences the following loading setting; V_{ac}=40 V, V_{DC}=90 V and Ω_{exc}=1.0388 MHz. The delay of 36 msec exists before the input rate implementation. This time delay is needed to allow the vibrational mode amplitudes to reach the steady-state condition.

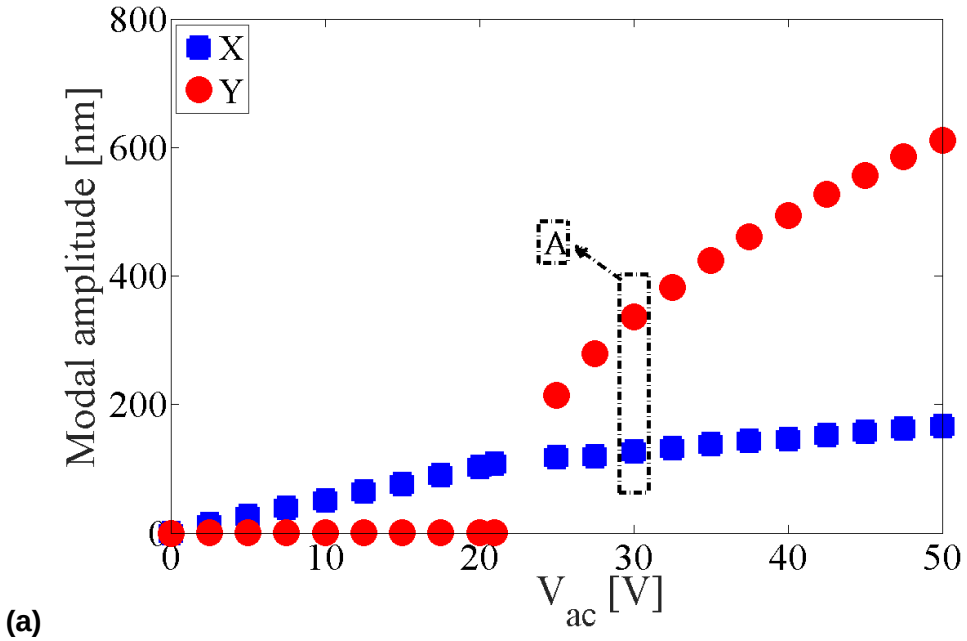

(a)

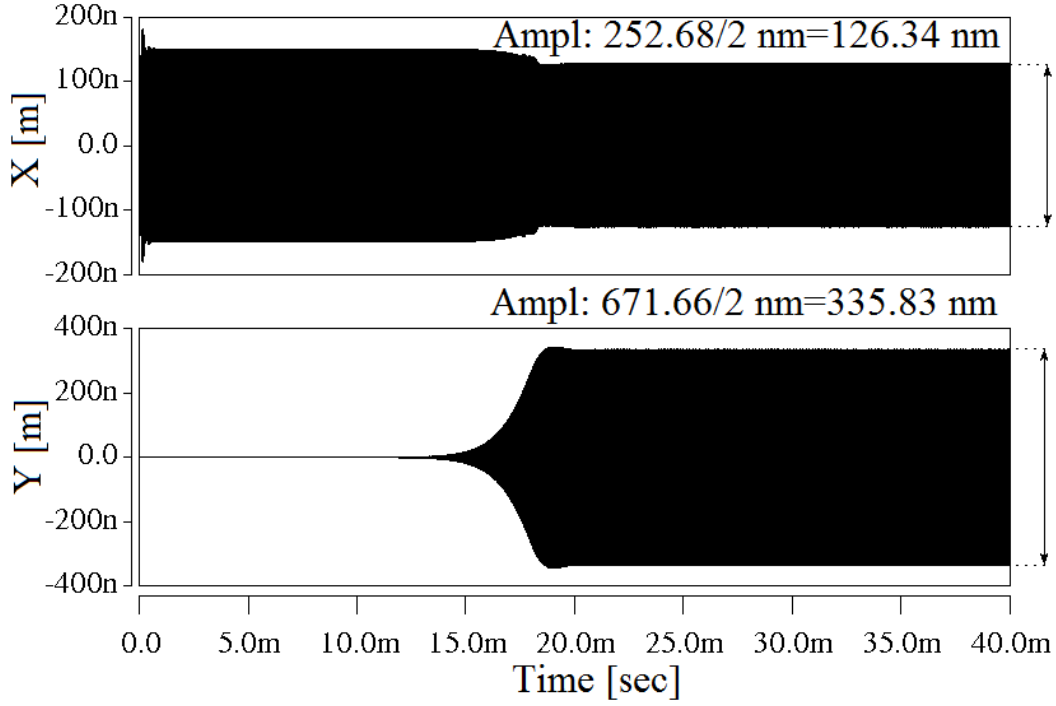

(b)

Figure 3.12. **Transient simulation results obtained using Architect™ for the frame-shaped microresonator, where V_{DC}=90 V and Ω_{exc}=1.0388 MHz. (a) the steady-state modal amplitudes of X and Y extracted from repeated transient simulations for V_{ac}=[0 50] V. (b) the oscillation amplitudes of the spring-mode (*X*) and the pendulum-mode (*Y*) for region *A* corresponding to V_{ac}=30 V.**

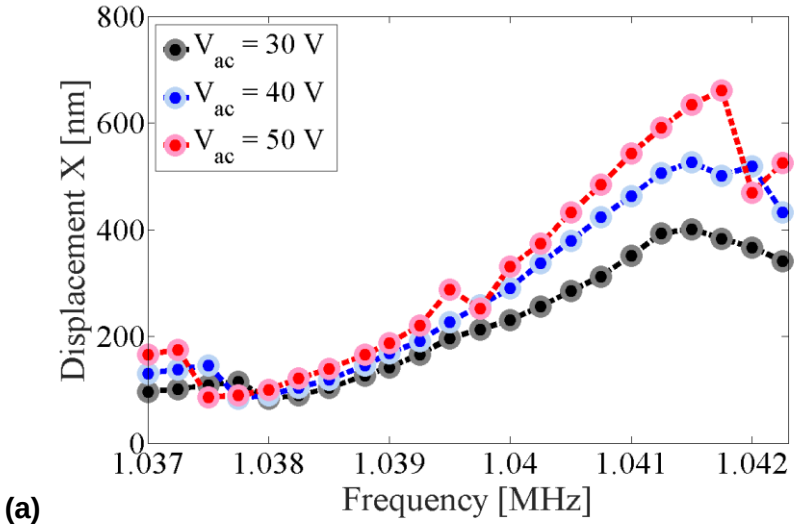

(a)

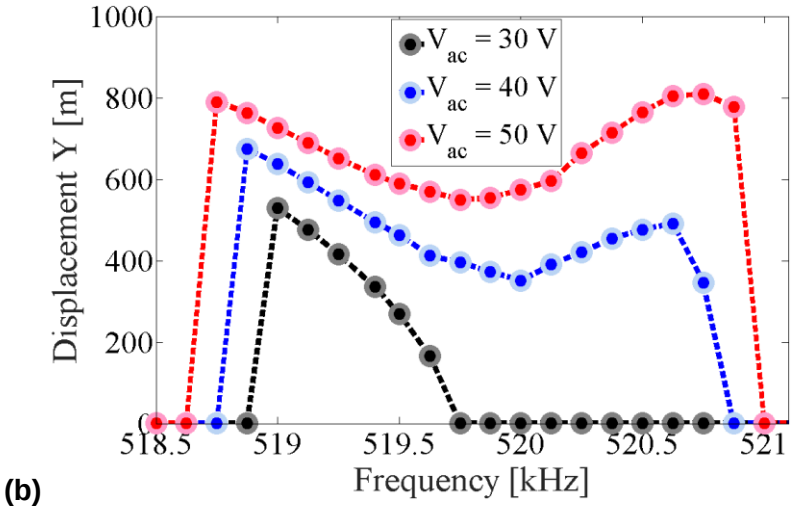

(b)

Figure 3.13. Simulated nonlinear frequency response curves for the frame-shaped microresonator achieved via Architect™ (a) the spring mode and (b) the pendulum mode.

The sensitivity of the microresonator when it rotates with the input angular velocity of Ω_Z=±3 RPS (or ±172 DPS) is shown in Figure 3.14. The steady-state amplitudes of the spring and pendulum modes before and after the effect of the rate can be realized for the time interval [34 36] and [131 136] msec, respectively. From the figure, it can be apparently inferred that there is a growth in the signal envelope in the modal amplitudes when subjected to the angular rate. The same study is accomplished for a broader range of angular velocities Ω_Z= [-229 229] DPS (or [-4 4] RPS) and the resulting dynamical behavior of the microresonator is demonstrated in Figure 3.15.The results indicate the linear

sensitivity in the range of -172 DPS≤ Ω_Z ≤172 DPS for the microdevice. The pendulum and spring-mode responses start to be insensitive to the rotational rate after Ω_Z=172 DPS.

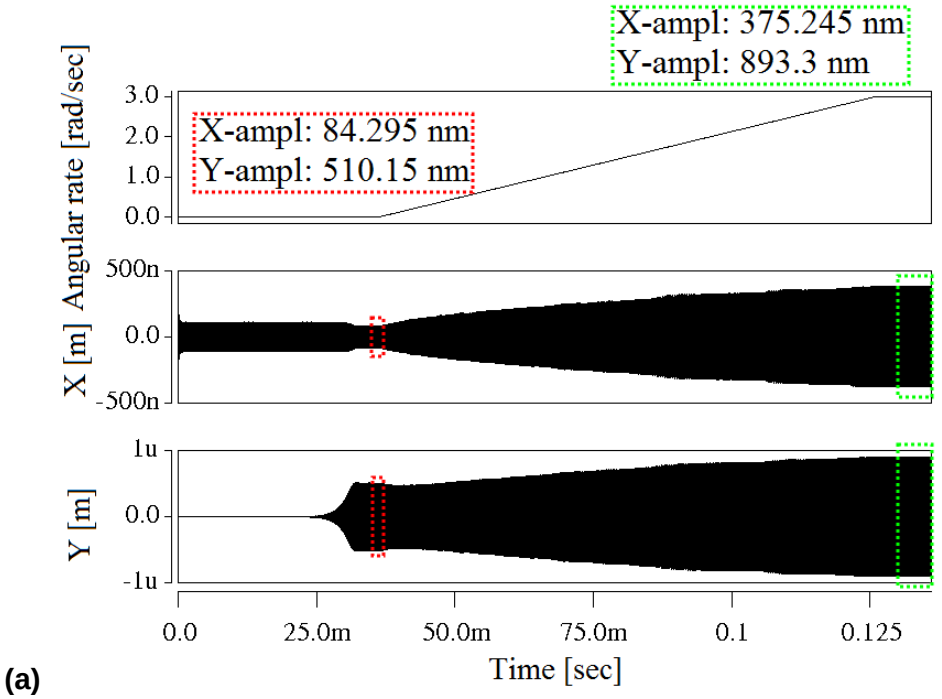

(a)

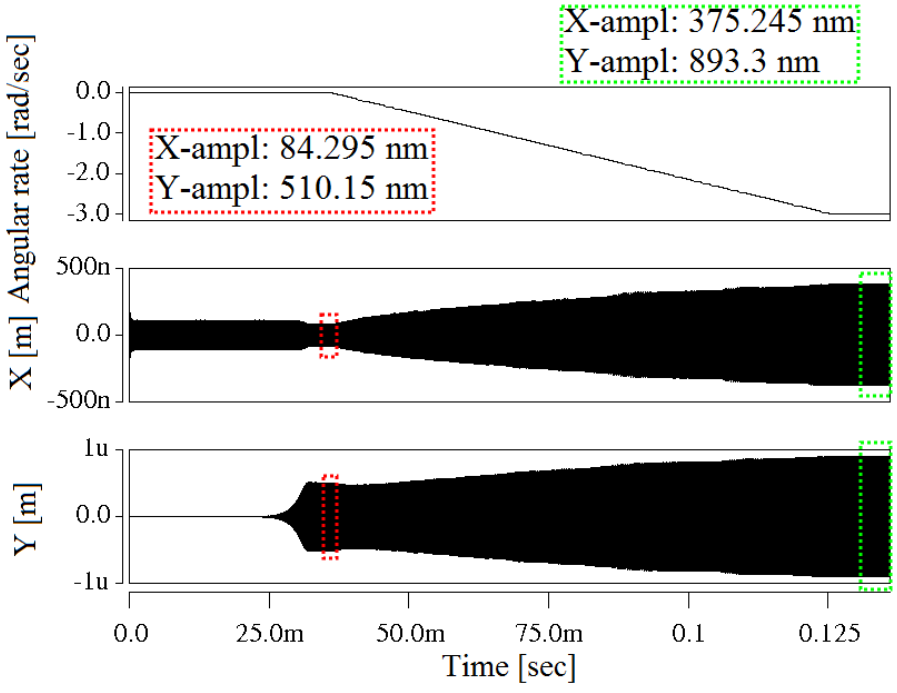

(b)

Figure 3.14. Time-domain analysis (Architect™) for the frame-shaped tuning fork microresonator, when the applied angular velocity Ω_Z equals to (a) 3 RPS (or 172 DPS) and (b) -3 RPS or (-172 DPS).

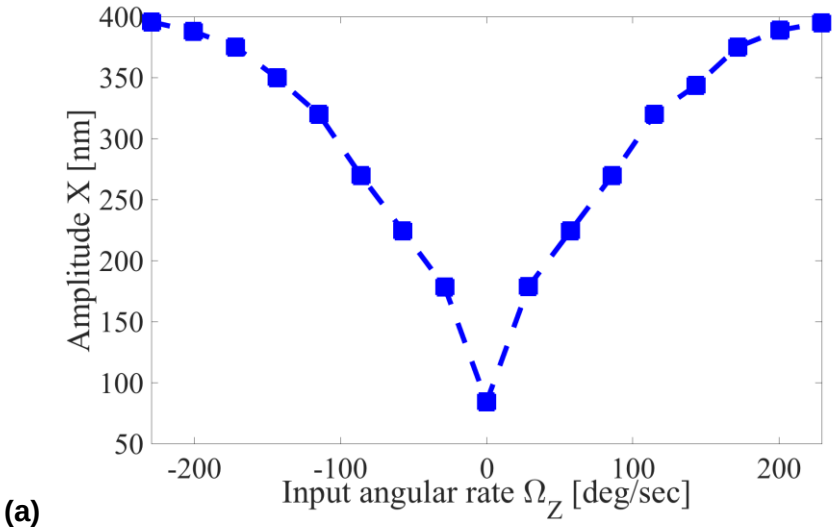

(a)

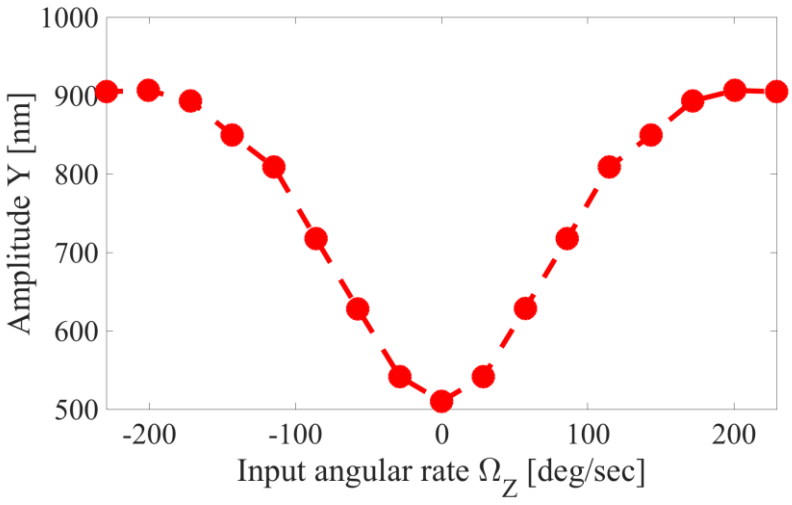

(b)

Figure 3.15. Simulated sensitivity plots acquired using Architect™ for the frame-shaped tuning fork microresonator, when exposed to the input rate Ω_Z=[-229 229] DPS. (a) the spring mode and (b) the pendulum mode.

3.3.3. H-shaped tuning fork design

To demonstrate, yet another realization of the spring-pendulum mechanism in MEMS, an in-plane H-shaped tuning fork microresonator design is introduced. Figure 3.16 shows the top view of the structure. This design consists of two identical 2-DOF resonators, as the left (green) resonator and the right (red) resonator as illustrated in Figure 3.16 (a). Each 2-DOF resonator dynamically can act as a spring-pendulum mechanism under the impact of proper harmonic forcing levels. The top and bottom

coupling beams secure the resonators. Therefore, one can analyze the dynamics of the device by two spring-pendulum mechanisms joined through the coupling beams.

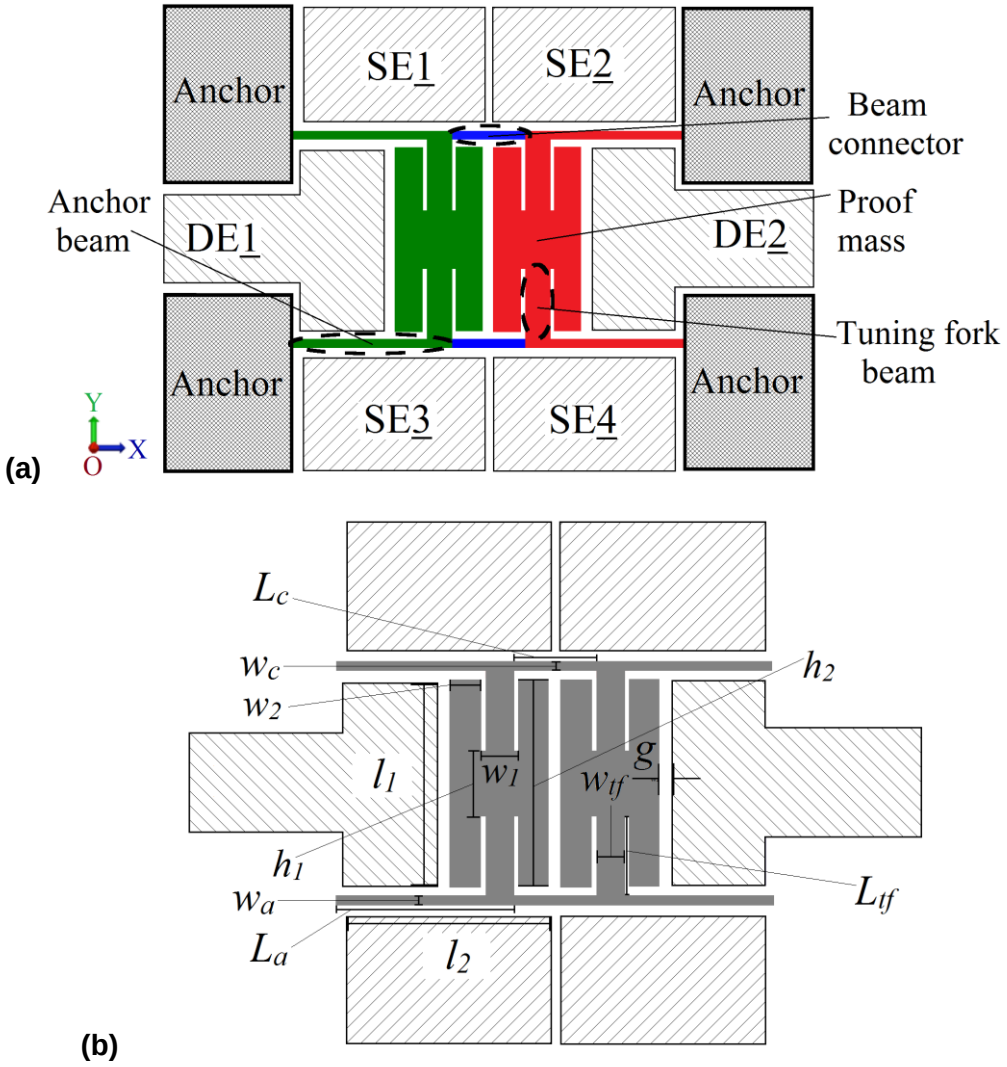

Figure 3.16. Schematic of the H-shaped tuning fork microresonator. (a) outline of the device. (b) the TF design parameters.

The device utilizes twin proof masses that are mechanically connected through beam suspensions to form an H-shaped structure. The H-shaped proof masses can move in the radial direction and rotate about the anchor, simultaneously. The flexural beam suspensions consist of the anchor beams, the tuning fork beams, and the coupling beams. The microdevice is enclosed by series of symmetrically placed parallel plate electrodes; two drive electrodes (DE) 1 and 2 and four sense electrodes (SE) 1-4. The design parameters in Figure 3.16 (b), are explained in Table 3.4. Similar to the previous

microresonator designs, transient analysis with Architect™ helps us to study the nonlinear dynamics and rate sensitivity of the H-shaped tuning fork microresonator.

Table 3.4. Design parameters of the H-shaped tuning fork microresonator.

Symbol	Quantity
L_a	The length of the anchor beam
w_a	The width of the anchor beam
L_c	The length of the coupling beam
w_c	The width of the coupling beam
L_{tf}	The length of the tuning fork beam
w_{tf}	The width of the tuning fork beam
w_1, w_2	The widths of the proof mass
h_1, h_2	The heights of the proof mass
l_1	The length of the drive electrodes 1 and 2
l_2	The length of the sense electrodes 1-4
g	The electrostatic gap

The detailed structure design is started from a high-level schematic as shown in Figure 3.17. The schematic incorporates twelve 1-segment nonlinear beams, eight beam side electrodes, two nonlinear rigid plates, two rigid plate side electrodes, an AC source, a DC source, eight constrained mechanical bus connectors, a reference frame, and an input angular rate function. Then, the schematic is processed, and a 3D view of the device is created according to the MIDIS process as shown in Figure 3.17(b). The design parameters are presented in Table 3.5. The dimensions of the structure are designed and tailored such that the linear natural frequency of the mode along the X-axis (spring mode) is twice the linear natural frequency of the mode along the Y-direction (pendulum mode). The drive and sense electrodes are biased with DC voltage of 70 V. Adjusting the DC bias voltage can be considered as a tool to tune the frequency ratio between the vibrational modes. The small-signal frequency analysis is carried out to find the natural frequencies and the structural mode shapes, Figure 3.18. It determines the natural frequencies at f_1=525.95 kHz (pendulum mode) and f_2=1.0548 MHz (spring mode). Accordingly, the frequency ratio is f_2/f_1 ~2.0055. The *Q*-factors are set to 500 and 1000 for the spring and pendulum modes, respectively. To implement the desired Q-factors for simulations, values of modal damping are calculated using Rayleigh's damping method (a=11.5938, b=3.0151$\times 10^{-10}$). Trapezoidal integration method is selected with truncation error of 0.001 in the transient simulation settings. Each simulation run on a personal computer with an

Intel Core i5-3450 processor and 16GB of RAM took about 7 hours to reach steady-state, corresponding to one pair of data points in Figure 3.19 or Figure 3.20 (i.e., the data in Figure 3.20 required 3×28×7=588 hours of calculations in addition to the time needed to update the parameters in between steps).

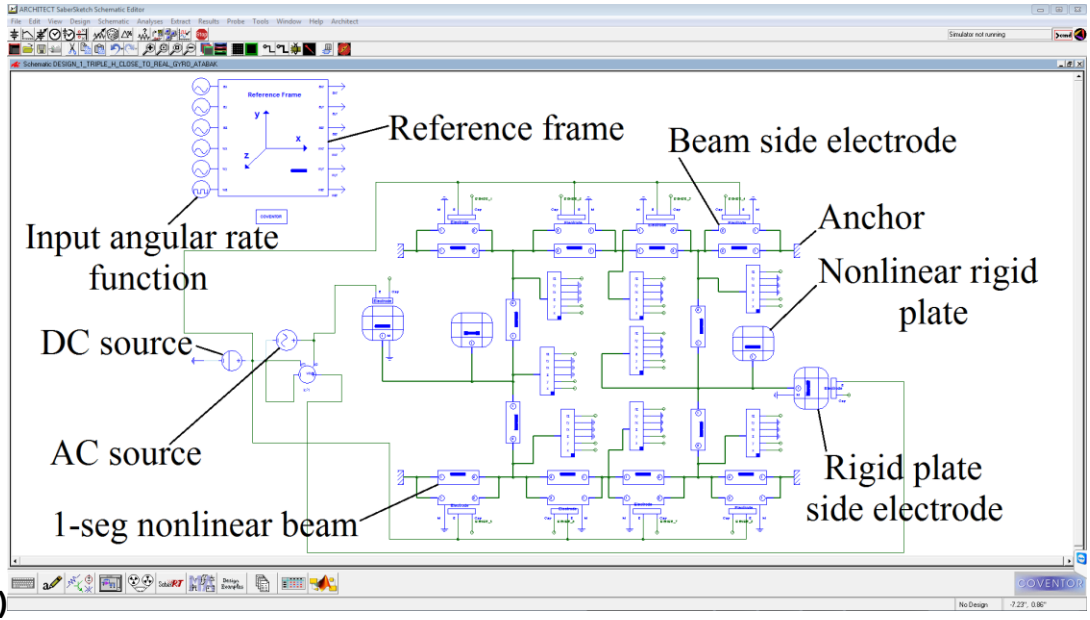

(a)

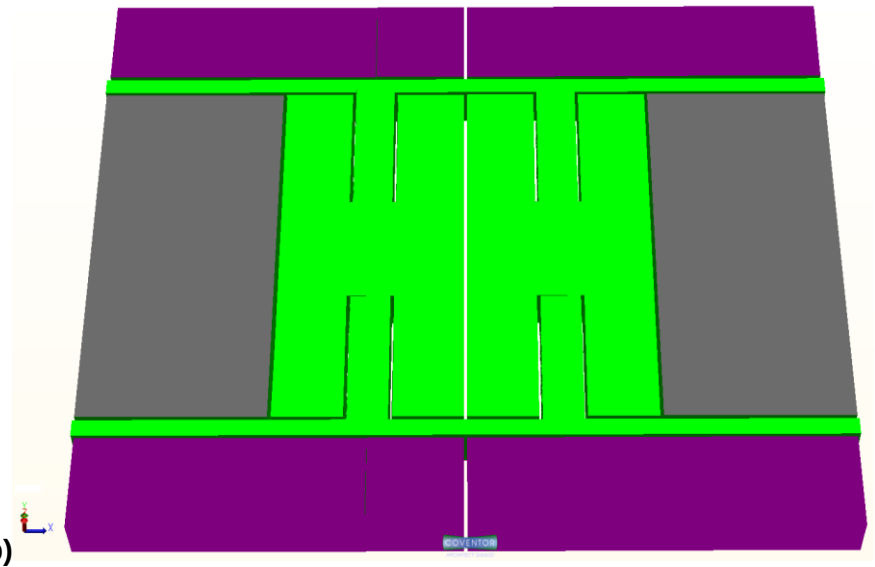

(b)

Figure 3.17. (a) Complete system schematic of the H-shaped microresonator in CoventorWare© Architect™, (b) 3D view of the built model in Architect™ Scence3D.

Table 3.5. The H-shaped design dimensions in Architect™ schematic.

Symbol	Quantity (μm)	Symbol	Quantity (μm)
L_a	159	h_1	60
w_a	9	w_2	36
L_c	78	h_2	206
L_{tf}	75	l_1	206
w_{tf}	21	l_2	195
w_1	25	g	1.75

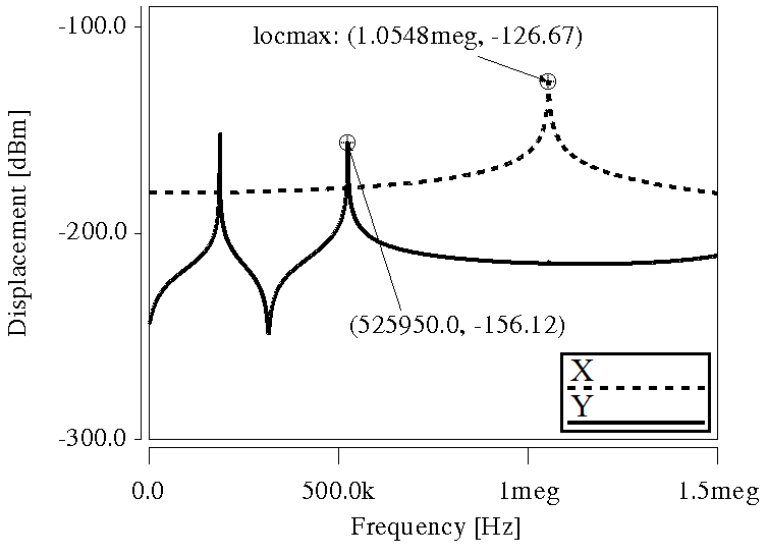

(a)

(b)

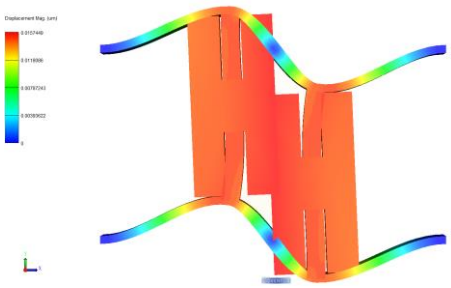

(c)

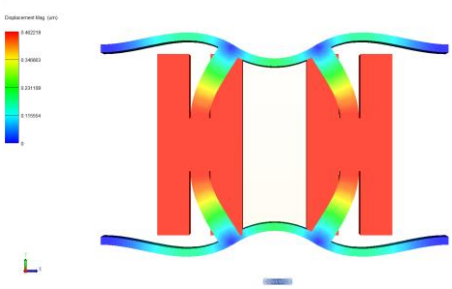

Figure 3.18. (a) Modal analysis of the H-shaped microresonator simulated using Architect™. (b) The pendulum mode shape with natural frequency 525.95 kHz. (c) The spring mode shape with natural frequency 1.0548 MHz. (blue-no displacement and red-maximum displacement)

The presence of the saturation phenomenon, and consequently quadratic couplings, in the H-shaped microresonator dynamics, can be confirmed in Figure 3.19. The figure illustrates the X-(spring) and Y-(pendulum) modal amplitudes as the AC voltage is changed from 0-40 V while the forcing frequency is secured at 1.052 MHz. It reveals

that the linear changes in the spring-mode amplitude (X) stop at V_{ac}=10 V. Instead the pendulum-mode response (Y) jumps from zero-static equilibrium and grows further by an increase in the actuation levels. The time-domain responses associated with the region A in Figure 3.19(a), i.e., for the case of V_{ac}=30 V, are demonstrated in Figure 3.19(b). It implies the energy transfer from the spring-mode (X) to the pendulum-mode (Y) after 1.75 msec.

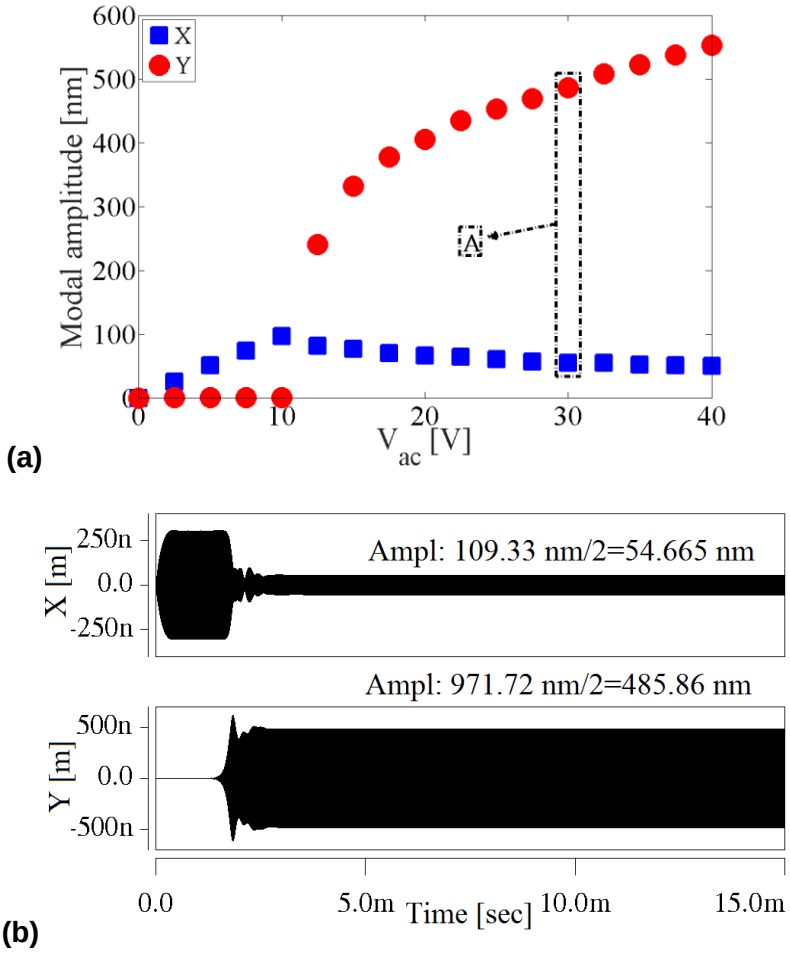

Figure 3.19. Transient simulation results obtained using Architect™ for the H-shaped microresonator, where V_{DC}=70 V and Ω_{exc}=1.052 MHz. (a) the steady-state modal amplitudes of X and Y extracted from repeated transient simulations for V_{ac}=[0 40] V. (b) the oscillation amplitudes of the spring-mode (X) and the pendulum-mode (Y) for region $\underline{A}$ corresponding to V_{ac}=30 V.

Figure 3.20 shows the nonlinear frequency response plots for various AC levels V_{ac} = 30, 40 and 50 V. This figure is achieved by measurement of the steady-state amplitudes of the signals (X and Y) for different excitation frequencies. It should be

mentioned that the excitation frequency is changed in the vicinity of the spring mode resonant frequency (f_2=1.0548 MHz). However, the vibrational modes respond differently. The spring-mode in Figure 3.20(a) resonates at the frequency of the excitation, although the pendulum-mode amplitudes shown in Figure 3.20(b) are captured at half the excitation frequency. This dynamical behavior is similar to the previously discussed microresonator designs. All share the same property, which can be explained by nonlinear vibrations generated by forced and 2:1 internal resonances.

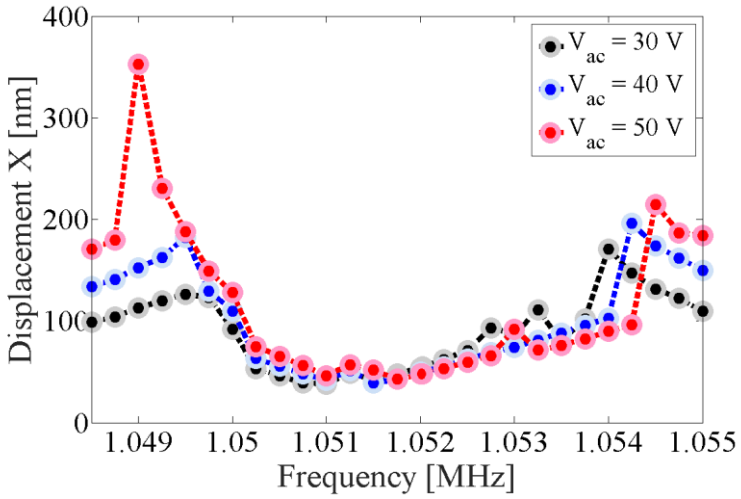

(a)

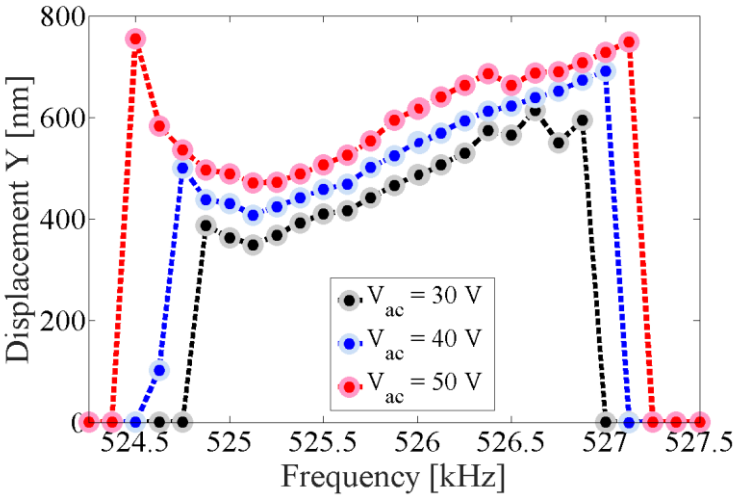

(b)

Figure 3.20. Simulated nonlinear frequency response curves for the H-shaped microresonator achieved via Architect™ (a) the spring mode and (b) the pendulum mode.

The truncation error in the transient setting is reduced to 0.00001 to run the time-domain simulations for examining the rate sensitivity. Figure 3.21 (a) and (b) exhibit the dynamical behavior of the microresonator as it is opposed to the input rate of Ω_Z= 1.5 RPS

(86 DPS) and Ω_Z= -1.5 RPS (-86 DPS), respectively, when V_{ac}=20 V. The assigned rate profile can be seen in the figure, which is constructed by 20-msec delay, a ramp function with constant angular acceleration 1910 deg/sec^2). As it can be observed in both cases, the microresonator reacts to it with an increase in the spring- and pendulum response amplitudes.

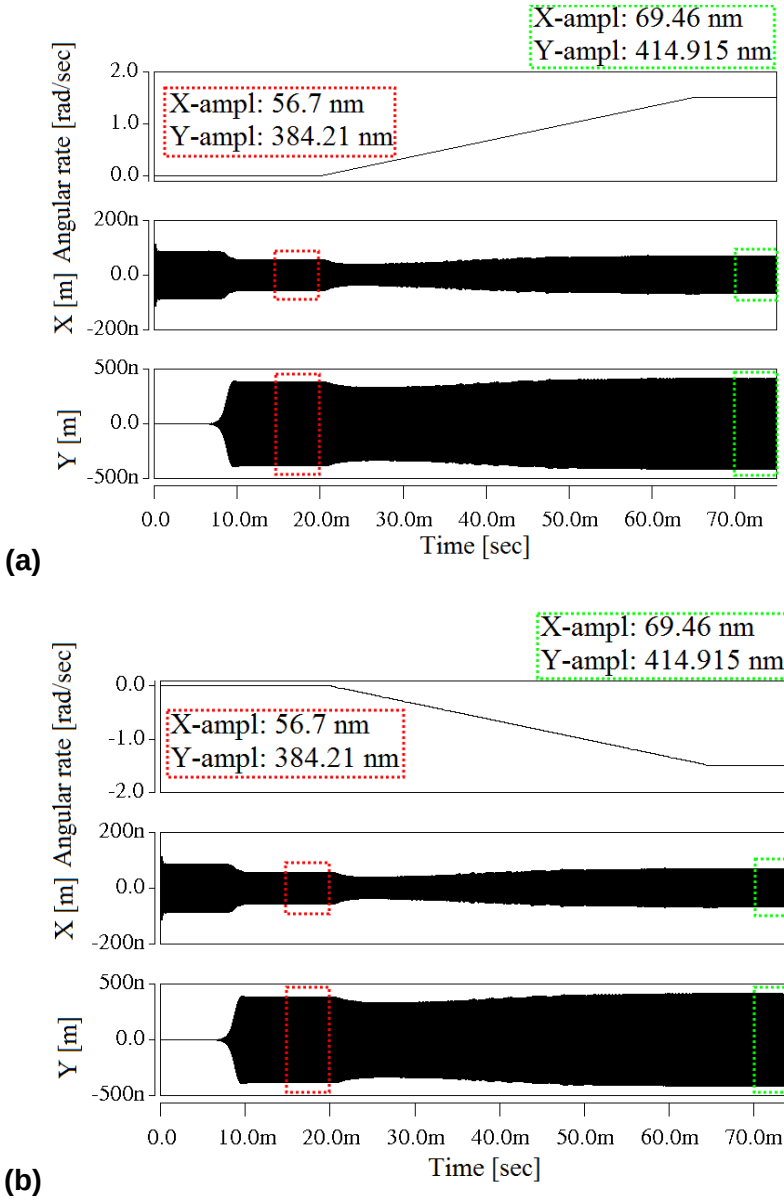

Figure 3.21. Time-domain analysis (Architect™) for the H-shaped tuning fork microresonator, when the applied angular velocity Ω_Z equals to (a) 1.5 RPS (or 86 DPS) and (b) -1.5 RPS (or -86 DPS).

And finally, the full-range of angular rate sensitivity of the microresonator for Ω_Z= [-100.3 100.3] DPS (or [-1.75 1.75] RPS) is demonstrated in Figure 3.22. Figure 3.22(a) shows the dynamical behaviour of the spring mode when subjected to the angular velocity and Figure 3.22(b) exhibits the pendulum mode under impact of the angular rate. Obviously, the steady-state modal amplitudes of the spring-(*X*) and pendulum (*Y*) modes keep increasing until the applied angular rate reaches to ±100.3 DPS which can be thought of the operational limit of the microresonator as an angular sensor.

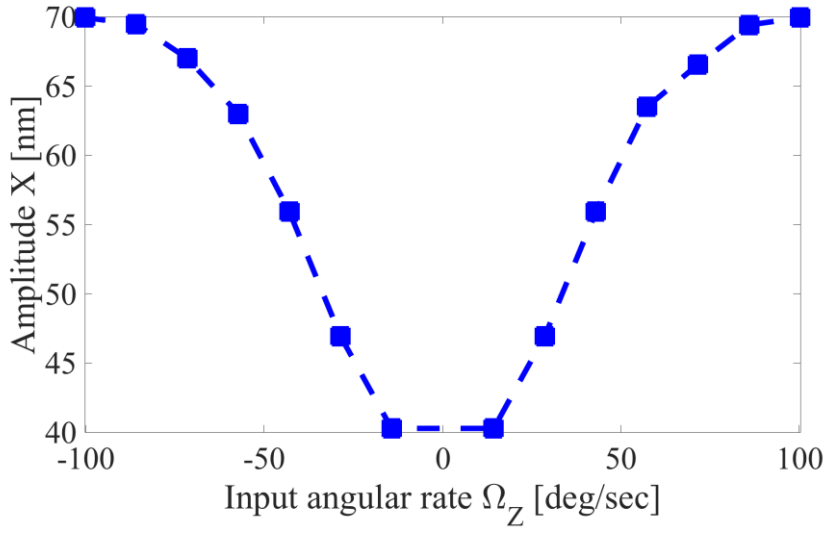

(a)

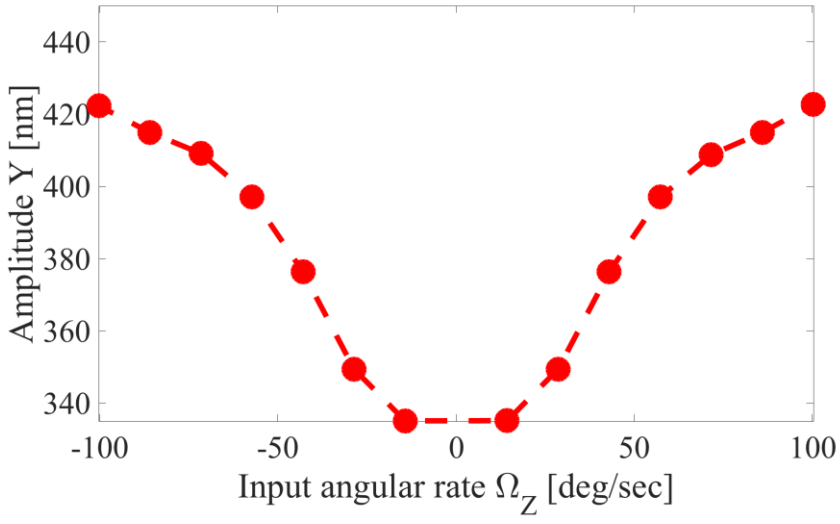

(b)

Figure 3.22. Simulated sensitivity plots acquired using Architect™ for the H-shaped tuning fork microresonator, when exposed to the input rate Ω_Z =[-100.3 100.3] DPS. (a) the spring mode and (b) the pendulum mode.

3.4. MEMS integrated design for inertial sensors fabrication technology

In this section, the MEMS integrated design for inertial sensors (MIDIS) fabrication process offered by Teledyne DALSA Inc. (TDSI) is discussed. The MIDIS platform is a high-aspect-ratio-bulk-micromachining process of a 30-µm thick single-crystal silicon (SCS) device layer that is vacuum encapsulated at 10 mTorr between two silicon wafers [113]. The bottom wafer (handle wafer) has a 380-µm thickness, while the top wafer (interconnect wafer) has a thickness of 108 µm. The top wafer includes through-silicon vias (TSVs) to create electrically isolated connections to the device wafer. The fabrication process flows for the handle, and device wafers can be found in [113].

The MIDIS design guidelines do not provide full characterization information regarding the etching profiles. As such, several device designs of the frame- and H-shaped microresonators with slight variations to the dimensions in Table 3.6 and Table 3.7 are designed to ensure a 2:1 ratio between the modes, respectively. The arrangement of the microresonators in the sketched layout is shown in Figure 3.23. Figure 3.24 exhibits, scanning electron microscope (SEM) image of the fabricated devices before encapsulation.

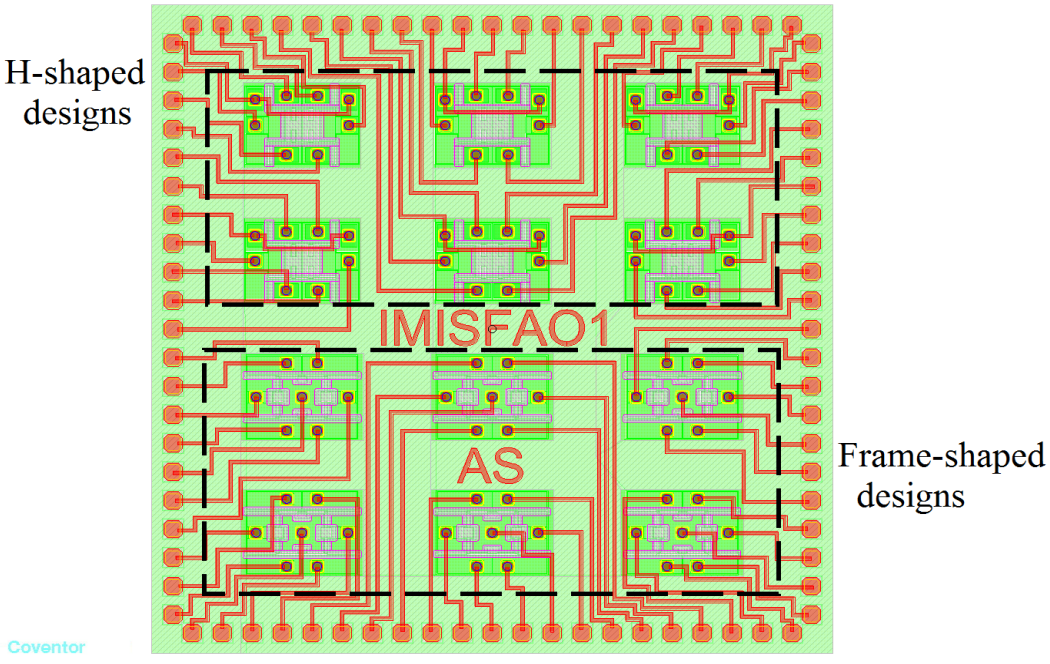

Figure 3.23. Schematic drawing of the layout, sketched using the Coventorware© Designer module, submitted to TDSI.

(a)

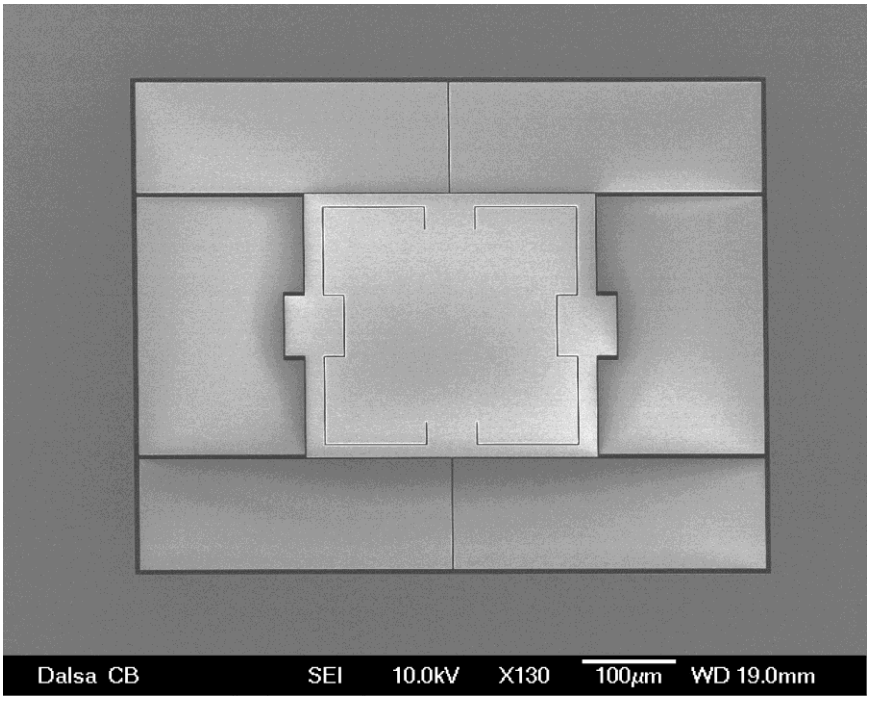

(b)

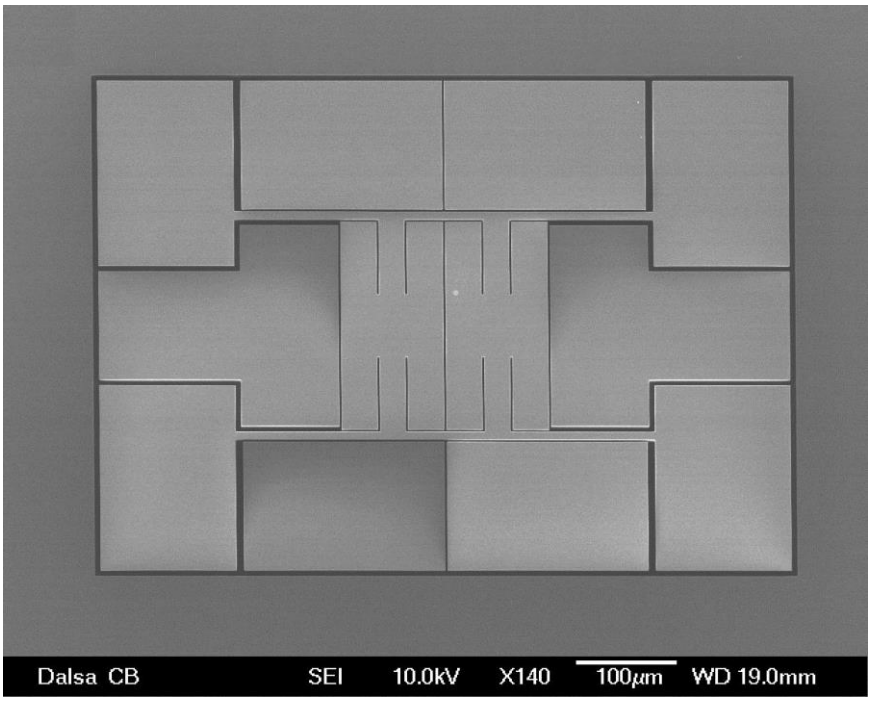

Figure 3.24. Top-view SEM image of (a) the frame-shaped and (b) H-shaped tuning fork microresonators before vacuum encapsulation.

Table 3.6. Design parameters of the frame-shaped microresonator in the presented layout to the external foundry.

Symbol	Value (μm)
L_a	25
w_a	50
L_b	150
w_b	12
L_{tf}	94
w_{tf}	18
w	60
h	62
g	2

Table 3.7. Design parameters of the H-shaped microresonator in the presented layout to the external foundry.

Symbol	Value (μm)	Symbol	Value (μm)
L_a	165	h_1	60
w_a	8	w_2	35
L_c	76	h_2	201
L_{tf}	72	l_1	194
w_{tf}	25	l_2	197
w_1	29	g	1.75

3.5. Summary

In this chapter, nonlinear microresonator designs were introduced which resemble the nonlinear dynamics of the spring-pendulum mechanism with the primary and 2:1 internal resonances. Nonlinear dynamic analysis of reduced-order model simulation software, Architect™ CoventorWare© was utilized to design and examine the 2:1 internal resonance based microresonators. These microresonators use 2:1 internal resonance in their functioning. Through extensive and timely simulations, it was proved that these designs were cable of exhibiting the nonlinear properties and sensitivity to the angular input rate. In the end, the MIDIS fabrication technology was introduced, and the SEM image of the microresonators studied in this dissertation was revealed.

Chapter 4.

Analytical modeling and experimental verification of nonlinear mode coupling in a frame-shaped tuning fork microresonator

This chapter provides the analytical and experimental studies into the nonlinear mode coupling in a frame-shaped tuning fork microresonator, with electrostatic actuation at forced and internal resonance frequencies. The systematic investigation leads to 4-DOF modal equations that take into account kinematic and electrostatic nonlinearities. The equations of motion are derived using Lagrange's energy method. The theoretical resonance curves are determined by using the two-variable expansion perturbation technique near internal resonance. The two desired mode shapes of the device are tailored to establish an approximate two-to-one frequency ratio between their natural frequencies. The influence of AC driving levels and a detuning frequency parameter, due to inevitable fabrication imperfections, on the system dynamics are investigated theoretically and experimentally. It is shown that the deviation from the ideal internal resonance condition separates the region of the nonlinear vibration into two distinct excitation frequencies. The model and simulated results obtained by the perturbation analysis are validated by comparing them with the experimental results.

4.1. Mathematical modeling and perturbation analysis

4.1.1. Description of the mathematical model

Symmetric with respect to a vertical central line, each half of the tuning fork microdevice, as shown in Figure 3.9, can be considered as a 2-DOF MSD mechanical system. Therefore, the microresonator forms a 4-DOF mechanical structure constructed by two decoupled 2-DOF spring-pendulum mechanisms. The lumped modeling has to be started with the consideration of a few assumptions as listed

1) According to the FEM modal analysis in CoventorWare©, rotation with respect to the anchor is allowed at either of the tuning fork beams ends. Thus, it seems reasonable to consider the tuning fork beams on each

side of the device as a simply supported beam with an attached proof mass in the middle.

2) Each half of the base beam can be considered as a cantilever beam in the analysis.

3) The left and right resonators are decoupled. Moreover, They can rotate with respect to the anchor, induced by substantial deformation of the suspension beams.

4) The tuning fork beams displace translationally with respect to the base beams attached to them. The base beams are pinned to the anchor to allow the rotation at the junction point.

5) The silicon anchor in the middle is assumed to be fixed and rigid during entire nonlinear operation of the microresonator.

Because of these assumptions, the tuning fork microresonator can be modeled as a 4-DOF mechanism, demonstrated in Figure 4.1. The (X, Y, Z) reference frame is stationary and centered at the point O. The constant input angular rate applied to the structure is denoted by Ω_Z. Mass M_i (i=1 and 2) represents the mass of the beam of length L_{tf} with the proof mass. The mass M_b represents the effective mass of two cantilever beams of length L_e where L_e=L_b-0.5(w_a+w_{tf}). The stiffness of the linear springs is represented by the spring constant K_i. The flexibility of each resonator is taken into account by a torsional spring with the spring constant of K_{ti}. The translational and torsional dampers of the system are denoted as C_i and C_{ti}, respectively. The electrostatic forces F_1 and F_3 are generated by the drive electrodes DE 1 and DE 2, respectively. The capacitive forces F_2 and F_4 represent, respectively, the difference between the forces exerted to the device by the sense electrodes SE 1 and SE 3, and SE 2 and SE 4. The differential sensing approach has been selected; therefore, the total captured capacitance can be doubled, resulting in boosting the output signal on each side of the device.

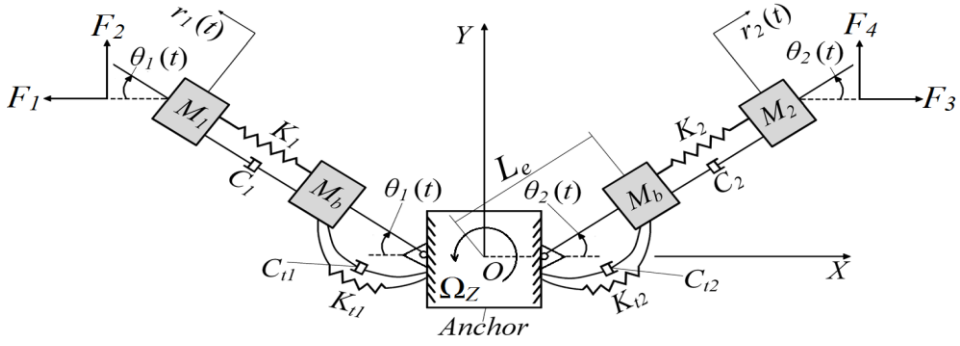

Figure 4.1. Lumped parameter model for the frame-shaped tuning fork dynamics.

4.1.2. Derivation of equations of motion

The equations of motion of the microresonator are achieved using Lagrangian dynamics. The equations are derived by applying symbolic manipulation software *MAPLE*. For the developed 4-DOF model, the kinematics are easily obtained using vector algebra. It is evident from the schematic of the system in Figure 4.1; the motion can be described by using four generalized coordinates (q). Namely, r_1 and r_2, the extension of the masses M_1 and M_2 along the radial direction, respectively, and θ_1 and θ_2, the angle that the masses M_1 and M_2 along with the mass M_b make with a horizontal line passing through the point O about which springs K_{t1} and K_{t2} rotate, respectively. Considering Figure 4.1, we define

$$\mathbf{r}_{M_1} = -\Big(\big(L_e + r_1(t)\big)\cos\big(\theta_1(t)\big)\Big)\hat{i} + \Big(\big(L_e + r_1(t)\big)\sin\big(\theta_1(t)\big)\Big)\hat{j} \tag{4.1}$$

$$\mathbf{r}_{(M_b)_L} = -L_e\cos\big(\theta_1(t)\big)\hat{i} + L_e\sin\big(\theta_1(t)\big)\hat{j} \tag{4.2}$$

$$\mathbf{r}_{M_2} = \Big(\big(L_e + r_2(t)\big)\cos\big(\theta_2(t)\big)\Big)\hat{i} + \Big(\big(L_e + r_2(t)\big)\sin\big(\theta_2(t)\big)\Big)\hat{j} \tag{4.3}$$

$$\mathbf{r}_{(M_b)_R} = L_e\cos\big(\theta_2(t)\big)\hat{i} + L_e\sin\big(\theta_2(t)\big)\hat{j} \tag{4.4}$$

as the vectors describing the positions of the masses M_1, M_b on the left side, M_2, and M_b on the right side, respectively. In the above equations, $\hat{i}$ and $\hat{j}$ are the unit vectors of the (X, Y, Z)-coordinate reference frame. Thus, the velocities of the masses can be calculated as

$$\begin{aligned}\dot{\mathbf{r}}_{M_1} = &\big(-\dot{r}_1(t)\cos\big(\theta_1(t)\big) + \big(L_e + r_1(t)\big)\big(\dot{\theta}_1(t) - \Omega_Z\big)\sin\big(\theta_1(t)\big)\big)\hat{i} \\ &+\big(\dot{r}_1(t)\sin\big(\theta_1(t)\big) + \big(L_e + r_1(t)\big)\big(\dot{\theta}_1(t) - \Omega_Z\big)\cos\big(\theta_1(t)\big)\big)\hat{j}\end{aligned} \tag{4.5}$$

$$\dot{\mathbf{r}}_{(M_b)_L} = \big(L_e\big(\dot{\theta}_1(t) - \Omega_Z\big)\sin\big(\theta_1(t)\big)\big)\hat{i} + \big(L_e\big(\dot{\theta}_1(t) - \Omega_Z\big)\cos\big(\theta_1(t)\big)\big)\hat{j} \tag{4.6}$$

$$\begin{aligned}\dot{\mathbf{r}}_{M_2} = &\big(\dot{r}_2(t)\cos\big(\theta_2(t)\big) - \big(L_e + r_2(t)\big)\big(\dot{\theta}_2(t) + \Omega_Z\big)\sin\big(\theta_2(t)\big)\big)\hat{i} \\ &+\big(\dot{r}_2(t)\sin\big(\theta_2(t)\big) + \big(L_e + r_2(t)\big)\big(\dot{\theta}_2(t) + \Omega_Z\big)\cos\big(\theta_2(t)\big)\big)\hat{j}\end{aligned} \tag{4.7}$$

$$\dot{\mathbf{r}}_{(M_b)_R} = -\left(L_e\left(\dot{\theta}_2(t)+\Omega_Z\right)\sin\left(\theta_2(t)\right)\right)\hat{i}+\left(L_e\left(\dot{\theta}_2(t)+\Omega_Z\right)\cos\left(\theta_2(t)\right)\right)\hat{j} \tag{4.8}$$

The dot represents differentiation with respect to the time *t*. Hence, the kinetic energy (*KE*) of the system can be expressed as

$$\begin{aligned} KE = \frac{1}{2}M_1\dot{\mathbf{r}}_{M_1}\cdot\dot{\mathbf{r}}_{M_1}+\frac{1}{2}M_b\,\dot{\mathbf{r}}_{(M_b)_L}\cdot\dot{\mathbf{r}}_{(M_b)_L}+\frac{1}{2}M_2\dot{\mathbf{r}}_{M_2}\cdot\dot{\mathbf{r}}_{M_2}+\frac{1}{2}M_b\,\dot{\mathbf{r}}_{(M_b)_R}\cdot\dot{\mathbf{r}}_{(M_b)_R} = \\ \frac{1}{2}\left(M_1r_1^2(t)+2L_eM_1r_1(t)+L_e^2(M_1+M_b)\right)\dot{\theta}_1^2(t) \\ +\frac{1}{2}\left(M_2r_2^2(t)+2L_eM_2r_2(t)+L_e^2(M_2+M_b)\right)\dot{\theta}_2^2(t) \\ +\frac{1}{2}M_1\dot{r}_1^2(t)+\frac{1}{2}M_2\dot{r}_2^2(t) \\ +\frac{1}{2}\left(M_1r_1^2(t)+M_2r_2^2(t)+2L_eM_2r_2(t)+2L_eM_1r_1(t)+L_e^2(M_2+M_2+2M_b)\right)\Omega_Z^2 \\ +\frac{1}{2}\begin{pmatrix}-\left(2M_1r_1^2(t)+4L_eM_1r_1(t)+2L_e^2(M_1+M_b)\right)\dot{\theta}_1(t) \\ +\left(2M_2r_2^2(t)+4L_eM_2r_2(t)+2L_e^2(M_2+M_b)\right)\dot{\theta}_2(t)\end{pmatrix}\Omega_Z \end{aligned} \tag{4.9}$$

The potential energy (*PE*) of the system involves that of the translational and torsional springs K_1, K_{t1}, K_2 and K_{t2}, and can be written as

$$PE = \frac{1}{2}\left(K_1\left(r_1(t)\right)^2+K_{t1}\left(\theta_1(t)\right)^2+K_2\left(r_2(t)\right)^2+K_{t2}\left(\theta_2(t)\right)^2\right) \tag{4.10}$$

Rayleigh's dissipation force (F_d) can also be defined as

$$F_d = \frac{1}{2}\left(C_1\left(\dot{r}_1(t)\right)^2+C_{t1}\left(\dot{\theta}_1(t)\right)^2+C_2\left(\dot{r}_2(t)\right)^2+C_{t2}\left(\dot{\theta}_2(t)\right)^2\right) \tag{4.11}$$

Lagrange's equations of motion of the microdevice are

$$\begin{cases} L=KE-PE \\ \left(\dfrac{\partial L}{\partial \dot{q}_i}\right)-\dfrac{\partial L}{\partial q_i}+\dfrac{\partial F_d}{\partial \dot{q}_i}=G_i,\ i=1\text{-}4 \end{cases} \tag{4.12}$$

where *L* is the Lagrangian of the system; the q_i is the generalized coordinate; and the G_i is defined as the nonconservative force or moment applied to the system. Hence,

$$\left.\begin{array}{c} q_1=\theta_1,\ q_2=r_1,\ q_3=\theta_2,\ q_4=r_2 \\ G_1=-\dfrac{F_2}{\cos(\theta_1(t))}(L_e+r_1(t)),\ G_2=-\dfrac{F_1}{\cos(\theta_1(t))} \\ G_3=\dfrac{F_4}{\cos(\theta_2(t))}(L_e+r_2(t)),\ G_4=\dfrac{F_3}{\cos(\theta_2(t))} \end{array}\right\} \tag{4.13}$$

Substituting Equations (4.9)-(4.11) and Equation (4.13) into Equation (4.12), the equations of motion can be derived as follow

$$\begin{gathered} L_e^2(M_b+M_1)\ddot{\theta}_1(t)+C_{t1}\dot{\theta}_1(t)+K_{t1}\theta_1(t)=-F_2\frac{(L_e+r_1(t))}{\cos(\theta_1(t))} \\ \left(M_1\left(r_1^2(t)+2L_e r_1(t)\right)+L_e^2(M_b+M_1)\right)\dot{\Omega}_Z-M_1\left(r_1^2(t)+2L_e r_1(t)\right)\ddot{\theta}_1(t) \\ -2M_1(L_e+r_1(t))\dot{r}_1(t)\dot{\theta}_1(t)+2M_1(L_e+r_1(t))\dot{r}_1(t)\Omega_Z \end{gathered} \tag{4.14}$$

$$\begin{gathered} M_1\ddot{r}_1(t)+C_1\dot{r}_1(t)+K_1r_1(t)=M_1(L_e+r_1(t))\dot{\theta}_1^2(t)-\frac{F_1}{\cos(\theta_1(t))} \\ -2M_1(L_e+r_1(t))\dot{\theta}_1(t)\Omega_Z+M_1(L_e+r_1(t))\Omega_Z^2 \end{gathered} \tag{4.15}$$

$$\begin{gathered} L_e^2(M_b+M_2)\ddot{\theta}_2(t)+C_{t2}\dot{\theta}_2(t)+K_{t2}\theta_2(t)=F_4\frac{(L_e+r_2(t))}{\cos(\theta_2(t))} \\ -\left(M_2\left(r_2^2(t)+2L_e r_2(t)\right)+L_e^2(M_b+M_2)\right)\dot{\Omega}_Z-M_2\left(r_2^2(t)+2L_e r_2(t)\right)\ddot{\theta}_2(t) \\ -2M_2(L_e+r_2(t))\dot{r}_2(t)\dot{\theta}_2(t)-2M_2(L_e+r_2(t))\dot{r}_2(t)\Omega_Z \end{gathered} \tag{4.16}$$

$$\begin{gathered} M_2\ddot{r}_2(t)+C_2\dot{r}_2(t)+K_2r_2(t)=M_2(L_e+r_2(t))\dot{\theta}_2^2(t)+\frac{F_3}{\cos(\theta_2(t))} \\ +2M_2(L_e+r_2(t))\dot{\theta}_2(t)\Omega_Z+M_2(L_e+r_2(t))\Omega_Z^2 \end{gathered} \tag{4.17}$$

where

$$M_1=M_2=M_{Proof\,mass}+M_{tf\,beam}=t_{si}\rho_{si}(wh+L_{tf}w_{tf}),\ M_b=0.4714t_{si}\rho_{si}L_e w_b$$

$$\omega_{n_1}=2\pi\left(K_{t1}/L_e^2(M_1+M_b)\right)^{1/2},\ \omega_{n_2}=2\pi(K_1/M_1)^{1/2}$$
$$\omega_{n_3}=2\pi\left(K_{t2}/L_e^2(M_2+M_b)\right)^{1/2},\ \omega_{n_4}=2\pi(K_2/M_2)^{1/2}$$

$$c_1=\omega_{n_1}\omega_{n_2}\frac{\left(\frac{\omega_{n_2}}{Q_1}\right)-\left(\frac{\omega_{n_1}}{Q_2}\right)}{\left(\omega_{n_2}\right)^2-\left(\omega_{n_1}\right)^2},\ d_1=\frac{\left(\frac{\omega_{n_2}}{Q_2}\right)-\left(\frac{\omega_{n_1}}{Q_1}\right)}{\left(\omega_{n_2}\right)^2-\left(\omega_{n_1}\right)^2}$$

$$c_2=\omega_{n_3}\omega_{n_4}\frac{\left(\frac{\omega_{n_4}}{Q_3}\right)-\left(\frac{\omega_{n_3}}{Q_4}\right)}{\left(\omega_{n_4}\right)^2-\left(\omega_{n_3}\right)^2},\ d_2=\frac{\left(\frac{\omega_{n_4}}{Q_4}\right)-\left(\frac{\omega_{n_3}}{Q_3}\right)}{\left(\omega_{n_4}\right)^2-\left(\omega_{n_3}\right)^2}$$

$$\begin{bmatrix}C_j\\C_{tj}\end{bmatrix}=c_j\begin{bmatrix}M_j & 0\\0 & \left(M_j+M_b\right)L_e^2\end{bmatrix}+d_j\begin{bmatrix}K_j & 0\\0 & K_{tj}\end{bmatrix},\ j=1 \text{ and } 2$$

$$F_1=\frac{1}{2}\left(V_{DC}+V_{ac}\cos(\Omega_r t)\right)^2 p_0 t_{si}\left(2\left(L_{tf}+w_b-4g\right)+h\right)\left(\frac{d}{d\left(r_1(t)\right)}\left(\frac{1}{g-r_1(t)}\right)\right)=$$

$$\frac{1}{2}\left(V_{DC}+V_{ac}\cos(\Omega_r t)\right)^2\left(2\left(L_{tf}+w_b-4g\right)+h\right)\frac{p_0 t_{si}}{\left(g-r_1(t)\right)^2}$$

$$F_2=\frac{1}{2}V_{DC}^2 p_0 t_{si}\left(L_b-\frac{g}{2}\right)\left(\frac{d}{d\left(\theta_1(t)\right)}\left(\frac{1}{g-L_e\tan\left(\theta_1(t)\right)}-\frac{1}{g+L_e\tan\left(\theta_1(t)\right)}\right)\right)=$$

$$\frac{1}{2}V_{DC}^2 p_0 t_{si}L_e\left(L_b-\frac{g}{2}\right)\left(1+\left(\tan\left(\theta_1(t)\right)\right)^2\right)\left(\frac{1}{\left(g-L_e\tan\left(\theta_1(t)\right)\right)^2}+\frac{1}{\left(g+L_e\tan\left(\theta_1(t)\right)\right)^2}\right)$$

$$F_3=\frac{1}{2}\left(V_{DC}+V_{ac}\cos(\Omega_r t)\right)^2 p_0 t_{si}\left(2\left(L_{tf}+w_b-4g\right)+h\right)\left(\frac{d}{d\left(r_2(t)\right)}\left(\frac{1}{g-r_2(t)}\right)\right)=$$

$$\frac{1}{2}\left(V_{DC}+V_{ac}\cos(\Omega_r t)\right)^2\left(2\left(L_{tf}+w_b-4g\right)+h\right)\frac{p_0 t_{si}}{\left(g-r_2(t)\right)^2}$$

$$F_4=\frac{1}{2}V_{DC}^2 p_0 t_{si}\left(L_b-\frac{g}{2}\right)\left(\frac{d}{d\left(\theta_2(t)\right)}\left(\frac{1}{g-L_e\tan\left(\theta_2(t)\right)}-\frac{1}{g+L_e\tan\left(\theta_2(t)\right)}\right)\right)=$$

$$\frac{1}{2}V_{DC}^2 p_0 t_{si}L_e\left(L_b-\frac{g}{2}\right)\left(1+\left(\tan\left(\theta_2(t)\right)\right)^2\right)\left(\frac{1}{\left(g-L_e\tan\left(\theta_2(t)\right)\right)^2}+\frac{1}{\left(g+L_e\tan\left(\theta_2(t)\right)\right)^2}\right)$$

where p_0 is the permittivity of the space (8.85×10^{-12} (F/m)); t_{si} is the thickness of silicon device layer; ρ_{si} is the mass density of silicon (2330 Kg/m^3); d/dx is defined as the differentiation with respect to the variable x; V_{DC} is the DC bias voltage applied to the

sense and drive electrodes; V_{ac} is the amplitude of the AC driving voltage applied to the drive electrodes; and Ω_r is the excitation frequency. The quality factor Q_i and the natural frequency ω_{n_i} (i=1-4) are substituted into Rayleigh's damping equation, stated above, to estimate the translational (C_1 and C_2) and rotational (C_{t1} and C_{t2}) damping coefficients. The description of device design parameters can be found in Table 3.2. It is worth mentioning that in Equations (4.14)-(4.17), the nonlinearities are kinematic and electrostatic. The nonlinear kinematic terms include $\dot{r}_1$ and $\dot{\theta}_1$ (e.g., $\dot{r}_1\dot{\theta}_1$), whereas the electrostatic nonlinearities stem from the electrostatic forces produced by the drive and sense electrodes. The effect of Coriolis coupling between the vibrational modes r_i and θ_i can be spotted in the equations of motion (e.g., $2M_1(L_e+r_1)\dot{r}_1\Omega_Z$ and $2M_1(L_e+r_1)\dot{\theta}_1\Omega_Z$).

The linearized resonance frequencies can be expressed as $\omega_{n_1}=\omega_{n_3}$ and $\omega_{n_2}=\omega_{n_4}$ if the two systems are completely symmetric. That is $M_1= M_2$, $K_1= K_2$, $K_{t1}= K_{t2}$, $C_1= C_2$, $C_{t1}= C_{t2}$, $|r_1|=|r_2|$ and $|\theta_1|=|\theta_2|$. Nevertheless, this does not hold in real life due to unavoidable fabrication defects (such as over-etching). For simplicity of presentation, it is assumed that these values are equal, and due to the symmetric and uncoupled design of the microresonator, the perturbation analysis is carried out for the left resonator, shown in Figure 3.9.

4.1.3. Nondimensional and scaled equations of motion

To generalize the problem, the equations of motion, Equations (4.14)-(4.17), are nondimensionalized by introducing the following length and time scales.

$$P_1=\frac{r_1}{L_e},\ \Theta_1=\theta_1,\ t=\frac{\tau}{\Omega},\ \frac{d}{dt}=\Omega\frac{d}{d\tau},\ \frac{d^2}{dt^2}=\Omega^2\frac{d^2}{d\tau^2} \tag{4.18}$$

In the above equation, Ω is the nondimensionalizing frequency. Thus, the nondimensional equations take the form

$$\left.\begin{aligned}
&\ddot{\Theta}_1(\tau)+\gamma_{t1}\dot{\Theta}_1(\tau)+\omega_1^2\Theta_1(\tau)= \\
&-m_1\left(\left(P_1^2(\tau)+2P_1(\tau)\right)\ddot{\Theta}_1(\tau)+2\left(1+P_1(\tau)\right)\dot{P}_1(\tau)\dot{\Theta}_1(\tau)\right) \\
&+\left(m_1\left(P_1^2(\tau)+2P_1(t)\right)+1\right)\dot{\Omega}_Z+2m_1(P_1(t)+1)\dot{P}_1(\tau)\Omega_Z \\
&-\frac{1}{2}V_{DC}^2 p_0 t_{Si}\left(L_b-\frac{g}{2}\right)\left(1+\left(\tan\left(\Theta_1(\tau)\right)\right)^2\right). \\
&\left(\frac{1}{\left(g-L_e\tan\left(\Theta_1(\tau)\right)\right)^2}+\frac{1}{\left(g+L_e\tan\left(\Theta_1(\tau)\right)\right)^2}\right)\frac{\left(1+P_1(\tau)\right)}{(M_1+M_b)\Omega^2\cos\left(\Theta_1(\tau)\right)} \\
&\ddot{P}_1(\tau)+\gamma_1\dot{P}_1(\tau)+\omega_2^2P_1(\tau)=\left(1+P_1(\tau)\right)\dot{\Theta}_1^2(\tau) \\
&-2(P_1(t)+1)\dot{\Theta}_1(\tau)\Omega_Z+(P_1(t)+1)\Omega_Z^2 \\
&-\frac{1}{2}(V_{DC}+V_{ac}\cos(\Omega_1\tau))^2(2(L_{tf}+w_b-4g)+h)\frac{p_0 t_{Si}}{M_1L_e\Omega^2\left(g-L_eP_1(\tau)\right)^2\cos\left(\Theta_1(\tau)\right)}
\end{aligned}\right\} \quad (4.19)$$

where the dots represent the differentiation with respect to the nondimensional time τ. The natural frequencies of the uncoupled unforced linear system are

$$\omega_1=\frac{\sqrt{\frac{K_{t1}}{(M_1+M_b)L_e^2}}}{\Omega},\ \omega_2=\frac{\sqrt{\frac{K_1}{M_1}}}{\Omega} \quad (4.20)$$

The nondimensional mass and the nondimensional excitation frequency are defined as

$$m_1=\frac{M_1}{M_1+M_b},\ \Omega_1=\frac{\Omega_r}{\Omega} \quad (4.21)$$

The non-dimensional damping parameters are defined as

$$\gamma_{t1}=\frac{C_{t1}}{(M_1+M_b)L_e^2\Omega},\ \gamma_1=\frac{C_1}{M_1\Omega} \quad (4.22)$$

The unforced equations of motion have a stable equilibrium state at $\left(P_1=0,\ \dot{P}_1=0,\ \Theta_1=0,\ \dot{\Theta}_1=0\right)$. In the approximate solutions, we will replace the nonlinear trigonometric terms in Equation (4.19) by truncated Taylor expansions about this equilibrium point. Then, we proceed to scale them to see how large the effect of nonlinear terms is compared to the linear terms. The scaling process produces a small dimensionless parameter ε in the equations, $0<\varepsilon\ll 1$, which shows the order of nonlinearities and coupling. The

parameter ε is chosen so that we perturb off the linear equations for small ε. In other words, the motions are investigated in the vicinity of the static equilibrium position.

We introduce a change of variables as follow

$$\left.\begin{array}{c}\Theta_1(\tau)=\varepsilon^m\psi_1(\tau),\ P_1(\tau)=\varepsilon^n\rho_1(\tau),\ \Omega_Z=\varepsilon^p\dot{\varphi}(\tau)\\ V_{ac}=\varepsilon^r V_{AC},\ V_{DC}=\varepsilon^s V_{dc}\end{array}\right\} \tag{4.23}$$

In the above equation, m, n, p, r, and s are integers greater than or equal to one. These integers are to be specified such that the power of ε in the linear terms are of one order lower than the nonlinear terms. That is to say that we require the order of ε in the linear terms be zero, and at least one lower than the nonlinear terms.

The changed variables in Equation (4.23) are the substituted in Equation (4.19). The power values are to be specified as $m=n=p=r=s=1$ to meet the requirement above. To perturb off from the undamped linear equations, the damping coefficients γ_{t1}, and γ_1 are scaled. Therefore, the damping and nonlinear terms can appear in the same perturbation equations.

$$\gamma_{t1}=\varepsilon\mu_{t1},\ \gamma_1=\varepsilon\mu_1 \tag{4.24}$$

With these assumptions, the scaled equations of motion take the form of the following equations

$$\left.\begin{array}{c}\ddot{\psi}_1+\omega_1^2\psi_1+\varepsilon\left(2m_1\dot{\rho}_1\dot{\psi}_1+2m_1\rho_1\ddot{\psi}_1+\mu_{t1}\dot{\psi}_1\right)+\\ +\varepsilon^2 m_1\rho_1\left(\rho_1\ddot{\psi}_1+2\dot{\rho}_1\dot{\psi}_1\right)-\left(m_1\left(\varepsilon^2\rho_1^2+2\varepsilon\rho_1\right)+1\right)\ddot{\varphi}-2m_1\left(\varepsilon^2\rho_1+\varepsilon\right)\dot{\rho}_1\dot{\varphi}\\ =-\frac{1}{2}p_0 t_{Si}\frac{(2L_b-g)}{(M_1+M_b)\Omega^2 g^2}V_{dc}^2\left(\rho_1\varepsilon^2+\varepsilon\right)\\ \\ \ddot{\rho}_1+\omega_2^2\rho_1+\varepsilon\left(\mu_1\dot{\rho}_1-\dot{\psi}_1^2\right)-\varepsilon^2\rho_1\dot{\psi}_1^2=\\ -2\left(\varepsilon^2\rho_1+\varepsilon\right)\dot{\psi}_1\dot{\varphi}+\left(\varepsilon^2\rho_1+\varepsilon\right)\dot{\varphi}^2\\ -\left(\begin{array}{c}p_0 t_{Si}\left(2\left(L_{tf}+w_b-4g\right)+h\right)\left(\frac{2\rho_1\cos(\Omega_1\tau)\,\varepsilon^2}{M_1 g^3\Omega^2}+\frac{\cos(\Omega_1\tau)\,\varepsilon}{M_1 L_e g^2\Omega^2}\right)V_{dc}V_{AC}\\ +\left(\frac{\rho_1\varepsilon^2}{M_1 g^3\Omega^2}+\frac{\varepsilon}{2M_1 L_e g^2\Omega^2}\right)V_{dc}^2\\ +\left(\frac{\rho_1(\cos(\Omega_1\tau))^2\varepsilon^2}{M_1 g^3\Omega^2}+\frac{(\cos(\Omega_1\tau))^2\varepsilon}{2M_1 L_e g^2\Omega^2}\right)V_{AC}^2\end{array}\right)\end{array}\right\} \tag{4.25}$$

4.1.4. The two-variable expansion-perturbation method

The two-variable expansion-perturbation approach is utilized to understand the dynamics of the microresonator near internal and forced resonances [104]. In this approach, the independent variable τ would be replaced by two new variables ξ, and η, such that

$$\xi = \tau, \quad \eta = \varepsilon\tau \tag{4.26}$$

where ξ is an actual stretched time variable, and η is a slow time variable. The idea behind this perturbation technique is to express dependent variable ψ_1 and ρ_1 to depend explicitly on two-time scales ξ and η. For example, the periodic steady-state behavior will occur in ξ, while the approach to the steady state will occur in η [104].

Using the chain rule, we rewrite the time derivative of $\psi_1(\xi, \eta)$ and $\rho_1(\xi, \eta)$ such that

$$\frac{d}{d\tau} = \frac{\partial}{\partial\xi} + \varepsilon\frac{\partial}{\partial\eta} + O(\varepsilon^2), \quad \frac{d^2}{d\tau^2} = \frac{\partial^2}{\partial\xi^2} + 2\varepsilon\frac{\partial^2}{\partial\xi\partial\eta} + O(\varepsilon^2) \tag{4.27}$$

We also expand ψ_1 and ρ_1 as

$$\psi_1 = \psi_{10} + \varepsilon\psi_{11} + O(\varepsilon^2), \quad \rho_1 = \rho_{10} + \varepsilon\rho_{11} + O(\varepsilon^2) \tag{4.28}$$

At this point, the equations of motion are ready to be analyzed at the primary and 2:1 internal resonance cases. For the primary resonance case, we detune the resonance with the parameter σ_1 such that

$$\Omega_1 = \omega_2 + \varepsilon\sigma_1 \tag{4.29}$$

where σ_1 denotes the external forcing parameter. Substituting Equations (4.26)-(4.29) into Equation (4.25) and equating coefficients of equal powers of ε, neglecting terms of $O(\varepsilon^2)$, we find the zeroth and first-order equations of ε to be as follows.

For order ε^0

$$\psi_{1_{0\xi\xi}}+\omega_1^2\psi_{1_0}=\varphi_{\zeta\zeta},\ \rho_{1_{0\xi\xi}}+\omega_2^2\rho_{1_0}=0 \tag{4.30}$$

For order ε

$$\left.\begin{array}{c}\psi_{1_{1\xi\xi}}+\omega_1^2\psi_{1_1}=-2\psi_{1_{0\xi\eta}}-\mu_{t1}\psi_{1_{0\xi}}-2m_1\left(\rho_{1_0}\psi_{1_{0\xi\xi}}+\rho_{1_{0\xi}}\psi_{1_{0\xi}}\right)\\ -p_0t_{Si}\dfrac{(2L_b-g)}{2(M_1+M_b)(g\Omega)^2}V_{dc}^2+2m_1\left(\rho_{1_{0\xi}}\varphi_\zeta+\rho_{1_0}\varphi_{\zeta\zeta}\right)\\ \rho_{1_{1\xi\xi}}+\omega_2^2\rho_{1_1}=\left(\psi_{1_{0\xi}}\right)^2-\mu_1\rho_{1_{0\xi}}-2\rho_{1_{0\xi\eta}}+\left(\varphi_\zeta\right)^2-2\varphi_\zeta\psi_{1_{0\xi}}\\ -\dfrac{p_0t_{Si}(2(L_{tf}+w_b-4g)+h)}{2M_1L_e(g\Omega)^2}\left(\begin{array}{c}2V_{dc}V_{AC}\cos(\Omega_1\tau)+\\ V_{dc}^2+V_{AC}^2(\cos(\Omega_1\tau))^2\end{array}\right)\end{array}\right\} \tag{4.31}$$

where the sub-subscripts represent partial derivatives. The solution of Equations $(4.30)_{1,2}$ can be written in the form

$$\left.\begin{array}{l}\psi_{1_0}=k_1(\eta)\sin(\omega_1\xi)+k_2(\eta)\cos(\omega_1\xi)\\ \rho_{1_0}=k_3(\eta)\sin(\omega_2\xi)+k_4(\eta)\cos(\omega_2\xi)\end{array}\right\} \tag{4.32}$$

We now substitute Equation (4.32) into Equation (4.31), suppressing the secular terms $\sin(\omega_i\xi)$ and $\cos(\omega_i\xi)$ in Equation (4.31), where i=1 and 2. Secular terms cause unbounded growth in the signal amplitudes. They are needed to be eliminated. Note that we need to write

$$\cos(\Omega_1\xi)=\cos(\omega_2\xi+\sigma_1\eta)=\cos(\omega_2\xi)\cos(\sigma_1\eta)-\sin(\omega_2\xi)\sin(\sigma_1\eta) \tag{4.33}$$

Due to the length of the expressions, some of the intermediate steps are eliminated. The case of internal resonance, $\omega_2\approx2\omega_1$, is examined through the significance of the secular terms in the resonance. The case of $\omega_2\approx2\omega_1$ is the case when ω_2 is very close to $2\omega_1$. The detuning parameter σ_2 is introduced to show the closeness of the frequencies. Thus,

$$\omega_2=2\omega_1+\varepsilon\sigma_2 \tag{4.34}$$

In addition to Equation (4.33), we can write

$$\cos(\omega_2\xi)=\cos(2\omega_1\xi+\sigma_2\eta)=\cos(2\omega_1\xi)\cos(\sigma_2\eta)-\sin(2\omega_1\xi)\sin(\sigma_2\eta) \tag{4.35}$$

Before writing the solvability conditions, a polar transformation is introduced such that

$$\left.\begin{aligned} k_1(\eta)=a_1(\eta)\sin(\alpha_1(\eta)),\ k_2(\eta)=a_1(\eta)\cos(\alpha_1(\eta)) \\ k_3(\eta)=a_2(\eta)\sin(\alpha_2(\eta)),\ k_4(\eta)=a_2(\eta)\cos(\alpha_2(\eta)) \end{aligned}\right\} \tag{4.36}$$

where a_n and α_n are real functions of η. This transformation makes it possible to achieve the secular-term equations more conveniently. Therefore, the non-autonomous solvability equations, in polar form,

$$\left.\begin{aligned} \alpha_{1\eta}&=\frac{1}{2}m_1a_2(\omega_1-\omega_2)\cos(\beta_1) \\ a_{1\eta}&=-\frac{\mu_{t1}}{2}a_1+\frac{1}{2}m_1(\omega_1-\omega_2)a_1a_2\sin(\beta_1) \\ \alpha_{2\eta}&=-\frac{\omega_1^2}{4a_2\omega_2}a_1^2\cos(\beta_1)-\frac{p_0t_{Si}(2(L_{tf}+w_b-4g)+h)}{2M_1L_e(g\Omega)^2\omega_2a_2}V_{dc}V_{AC}\cos(\beta_2) \\ a_{2\eta}&=-\frac{\mu_1}{2}a_2+\frac{\omega_1^2}{4\omega_2}a_1^2\sin(\beta_1)-\frac{p_0t_{Si}(2(L_{tf}+w_b-4g)+h)}{2M_1L_e(g\Omega)^2\omega_2}V_{dc}V_{AC}\sin(\beta_2) \end{aligned}\right\} \tag{4.37}$$

where

$$\beta_1=2\alpha_1-\alpha_2+\sigma_2\eta,\quad \beta_2=\alpha_2+\sigma_1\eta \tag{4.38}$$

Eliminating α_1 and α_2 from Equation (4.37), we obtain the following set of equations

$$\left.\begin{aligned} \beta_{1\eta}&=m_1a_2(\omega_1-\omega_2)\cos(\beta_1)+\frac{\omega_1^2}{4a_2\omega_2}a_1^2\cos(\beta_1)+ \\ &\frac{p_0t_{Si}(2(L_{tf}+w_b-4g)+h)}{2M_1L_e(g\Omega)^2\omega_2a_2}V_{dc}V_{AC}\cos(\beta_2)+\sigma_2 \\ a_{1\eta}&=-\frac{\mu_{t1}}{2}a_1+\frac{1}{2}m_1(\omega_1-\omega_2)a_1a_2\sin(\beta_1) \\ \beta_{2\eta}&=-\frac{\omega_1^2}{4a_2\omega_2}a_1^2\cos(\beta_1)-\frac{p_0t_{Si}(2(L_{tf}+w_b-4g)+h)}{2M_1L_e(g\Omega)^2\omega_2a_2}V_{dc}V_{AC}\cos(\beta_2)+\sigma_1 \\ a_{2\eta}&=-\frac{\mu_1}{2}a_2+\frac{\omega_1^2}{4\omega_2}a_1^2\sin(\beta_1)-\frac{p_0t_{Si}(2(L_{tf}+w_b-4g)+h)}{2M_1L_e(g\Omega)^2\omega_2}V_{dc}V_{AC}\sin(\beta_2) \end{aligned}\right\} \tag{4.39}$$

When the condition for the steady-state solutions, i.e., the equilibrium solutions, is satisfied, that is $a_{1\eta}=a_{2\eta}=\beta_{1\eta}=\beta_{2\eta}=0$, there are two possible steady-state solutions for Equation (4.39). Where a_i and β_i (i=1 and 2) denote the steady-state nondimensionalized amplitudes and phase variables of modes. Two cases for Equation (4.39) can be recognized as follow. The first case is

$$\left.\begin{aligned} a_1&=0,\ a_2=-\frac{p_0 t_{Si}(2(L_{tf}+w_b-4g)+h)V_{dc}V_{AC}}{M_1\omega_2 L_e(g\Omega)^2\sqrt{4\sigma_1^2+\mu_1^2}} \\ \beta_1&=\cos^{-1}\left(\frac{(\sigma_1+\sigma_2)M_1\omega_2 L_e(g\Omega)^2\sqrt{4\sigma_1^2+\mu_1^2}}{p_0 t_{Si}(2(L_{tf}+w_b-4g)+h)V_{dc}V_{AC}m_1(\omega_1-\omega_2)}\right) \\ \beta_2&=\tan^{-1}\left(\frac{\mu_1}{\sqrt{4\sigma_1^2+\mu_1^2}},-\frac{2\sigma_1}{\sqrt{4\sigma_1^2+\mu_1^2}}\right) \end{aligned}\right\} \tag{4.40}$$

The first case implies the solutions to that of the linear systems, as follows

$$\left.\begin{aligned} \psi_1&=O(\varepsilon) \\ \rho_1&=-\frac{p_0 t_{Si}(2(L_{tf}+w_b-4g)+h)V_{dc}V_{AC}}{M_1\omega_2 L_e(g\Omega)^2\sqrt{4\sigma_1^2+\mu_1^2}}\cos(\Omega_1\tau-\beta_2)+O(\varepsilon) \end{aligned}\right\} \tag{4.41}$$

The second case is

$$\left.\begin{aligned} a_1&=-\frac{1}{\omega_1 g\Omega}\left[\frac{2\left(\Gamma_1\pm\sqrt{(\Gamma_2+\Gamma_3)(\Gamma_2-\Gamma_3)}\right)}{M_1 m_1 L_e(\omega_1-\omega_2)}\right]^{\frac{1}{2}} \\ a_2&=-\frac{\sqrt{(\mu_{t1})^2+(\sigma_1+\sigma_2)^2}}{m_1(\omega_2-\omega_1)} \\ \beta_1&=\tan^{-1}\left(\frac{\mu_{t1}}{\sqrt{(\mu_{t1})^2+(\sigma_1+\sigma_2)^2}},-\frac{\sigma_1+\sigma_2}{\sqrt{(\mu_{t1})^2+(\sigma_1+\sigma_2)^2}}\right) \\ \beta_2&=-\tan^{-1}\left(\frac{(\sigma_1+\sigma_2)\Gamma_3-\mu_{t1}\sqrt{(\Gamma_2+\Gamma_3)(\Gamma_2-\Gamma_3)}}{\mu_{t1}\Gamma_3+(\sigma_1+\sigma_2)\sqrt{(\Gamma_2+\Gamma_3)(\Gamma_2-\Gamma_3)}}\right) \end{aligned}\right\} \tag{4.42}$$

where

$$\begin{aligned}\Gamma_1&=M_1\omega_2 L_e(g\Omega)^2\left(\mu_1\mu_{t1}-2\sigma_1(\sigma_1+\sigma_2)\right)\\ \Gamma_2&=p_0 t_{Si}V_{dc}V_{AC}(\omega_1-\omega_2)m_1(2(L_{tf}+w_b-4g)+h)\\ \Gamma_3&=M_1\omega_2 L_e(g\Omega)^2\left((\mu_1+2\mu_{t1})\sigma_1+\mu_1\sigma_2\right)\end{aligned} \tag{4.43}$$

Hence, the steady-state response for this case is

$$\left.\begin{aligned}\psi_1&=-\frac{1}{\omega_1 g\Omega}\left[\frac{2\left(\Gamma_1\pm\sqrt{(\Gamma_2+\Gamma_3)(\Gamma_2-\Gamma_3)}\right)}{M_1 m_1 L_e(\omega_1-\omega_2)}\right]^{\frac{1}{2}}\cos\left(\frac{1}{2}(\Omega_1\tau-\beta_1-\beta_2)\right)+O(\varepsilon)\\ \rho_1&=-\frac{\sqrt{(\mu_{t1})^2+(\sigma_1+\sigma_2)^2}}{m_1(\omega_2-\omega_1)}\cos(\Omega_1\tau-\beta_2)+O(\varepsilon)\end{aligned}\right\} \tag{4.44}$$

By comparing the two feasible solutions, Equations (4.41) and (4.44), we can understand that ψ_1 responds at half of the excitation frequency due to the existence of the intended phenomena. Moreover, the phase of motion will be varying by $(\beta_1+\beta_2)$. The other observation from Equation (4.41) is that the amplitude of ρ_1 is the independent of the electrostatic actuation ($V_{dc}V_{AC}$) due to saturation phenomenon. Moreover, ρ_1 responds at the excitation frequency Ω_1. The system parameters utilized for simulations, which will be presented in this chapter, can be found in Table 4.1. It is noteworthy that the system parameters are estimated to agree with the experimental measurements.

Table 4.1. System parameter values for the frame-shaped microresonator.

Symbol	Value	Symbol	Value
ω_1	1	M_1	4.06×10^{-10} Kg
ω_2	1.9932	C_1	6.17×10^{-7} N/m.sec
Ω	ω_{n_1}	C_{t1}	5.97×10^{-15} N.m/sec
m_1	0.9	K_1	1.99×10^{4} N/m
μ_1	0.43	K_{t1}	7.54×10^{-5} N.m
μ_{t1}	0.28	M_b	4.92×10^{-11} Kg
ε	0.001	L_e	116 μm
σ_2	-6.8	g	2.25 μm

4.2. Experimental setup and resonance characterization

Two experimental test-beds are employed to explore the nonlinear mode coupling arising from the 2:1 internal resonance. The natural frequencies and the quality factors of the structure are estimated using the setup shown in Figure 4.2.

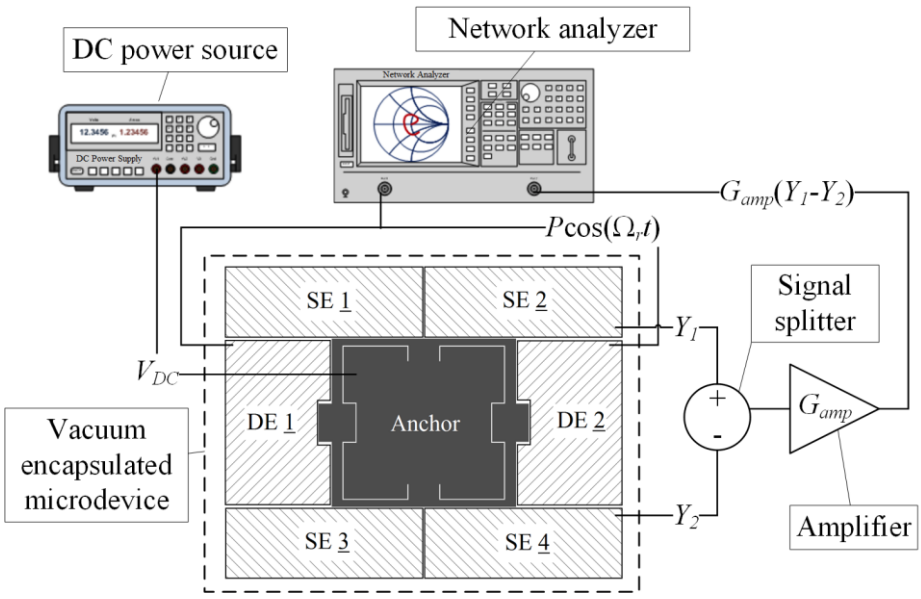

Figure 4.2. The experimental configuration to achieve the natural frequencies and the quality factors of the frame-shaped microresonator.

The setup includes (1) a vacuum encapsulated microresonator; (2) a DC power source (*Keysight, Model: B2901A*) with the output DC voltage of V_{DC}; (3) a vector network analyzer (*Rohde & Schwarz, Model: ZVB 4*); (4) a signal splitter (*Mini-Circuits SPLITTER, Model: ZFSCJ-2-2-S*) and (5) a lock-in amplifier (LIA) (*Zurich Instruments, Model: HF2LI*) with a pre-amp gain of G_{amp}. In the figure, P is the power of the output signal which has to be specified in the vector network analyzer in dBm, and Y_1 and Y_2 are the capacitance change captured via SE 2 and 4, respectively. The required setting to determine the natural frequencies is: V_{DC}=80 V, P =10 dBm and G_{amp}=10 kΩ. Figure 4.3 demonstrates two resonant modes of the device and the mode shapes simulated via CoventorWare© FEM analysis. The microresonator has its first desired natural frequency at f_1 =558.4 kHz (pendulum mode), and the corresponding quality factor is Q_1=3.6k. The second desired resonance frequency is at f_2=1.113 MHz (spring mode) with the quality factor of Q_2=4.6k. The frequency ratio is f_2/f_1 =1.9932≈2.

As it can be inferred from the figure, the state of 2:1 internal resonance is established between the anti-phase movements along the X-axis and the in-phase motions along the Y-axis. The observation is astonishing because the intended pendulum-mode shape in the design process was tailored to be the anti-phase movements of the masses along the Y-axis. The in-phase and out-of-phase modal displacement along the Y-axis were both detected using the network analyzer. However, the frequency ratio

between the resonant modes shown in Figure 4.3 was closer to 2:1. Therefore, the nonlinear mode coupling occurred between these two modes instead.

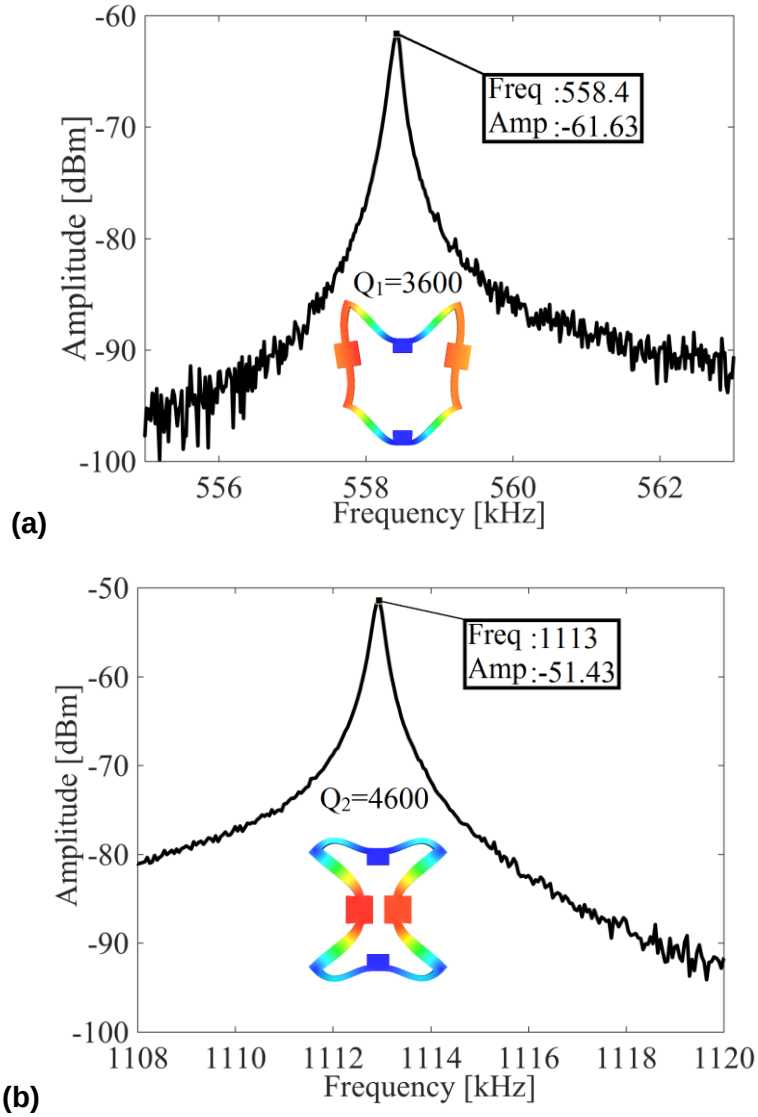

Figure 4.3. The experimentally measured frequency spectrum for the frame-shaped microresonator. The natural frequency and the quality factor of (a) the pendulum mode and (b) the spring mode.

The nonlinear mode interaction is evaluated through the saturation figure and the nonlinear frequency transmission plots. To achieve the plots, a series of experiments have to be accomplished through the experimental configuration demonstrated in Figure 4.4. The setup involves (1) a vacuum encapsulated microresonator; (2) a DC power source (*Keysight, Model: B2901A*) to bias the microresonator with the voltage V_{DC}; (3) a pulse function arbitrary generator (*Agilent Technologies, Model: 81150A*) to provide the

harmonic and sweep AC signals, i.e., $V_{ac}\cos(\Omega_r t)$, through the drive electrodes DE 1 and DE 2; (4) a signal splitter (*Mini-Circuits SPLITTER, Model: ZFSCJ-2-2-S*) to measure the output signals differentially and to remove interferences (improving the signal processing); (5) a lock-in amplifier of pre-amp gain G_{amp} (*Zurich Instruments, Model: HF2LI*) to boost the output current captured by the sense electrodes SE 2 and SE 4; (6) a signal analyzer (*Agilent Technologies, Model: N9000A*) to monitor the sensed signals in the frequency domain. The output signals Y_1 and Y_2 are proportional to the capacitance changes captured via SE 2 and SE 4, respectively.

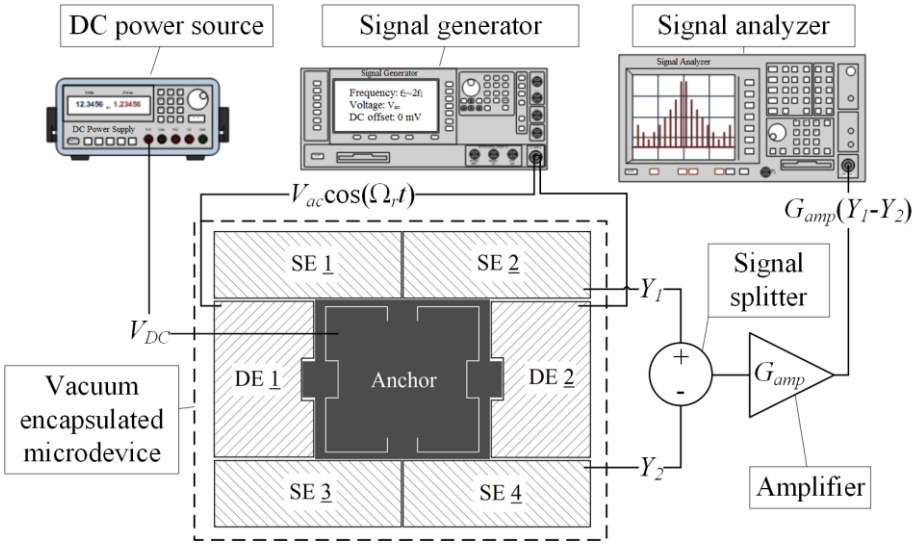

Figure 4.4. Experimental setup to obtain saturation figure and perform frequency sweeps for the frame-shaped microresonator.

4.3. Results and discussion

This section presents the simulation and experimental findings. When the system incorporating the 2:1 internal resonance is excited at a frequency near the higher natural frequency, the structure responds at the frequency of excitation, and the amplitude of the response increases linearly with the amplitude of excitation. However, when the amplitude of the mode with higher resonant frequency reaches a critical value, the response saturates and the additional energy spills over to the lower natural frequency mode. This phenomenon is known as saturation due to 2:1 internal resonance. The following loading setting is required to investigate saturation phenomenon: V_{DC} = 80 V, V_{ac} = 0–8.5, and G_{amp}=10 kΩ. Figure 4.5 shows the experimental observations confirming the saturation.

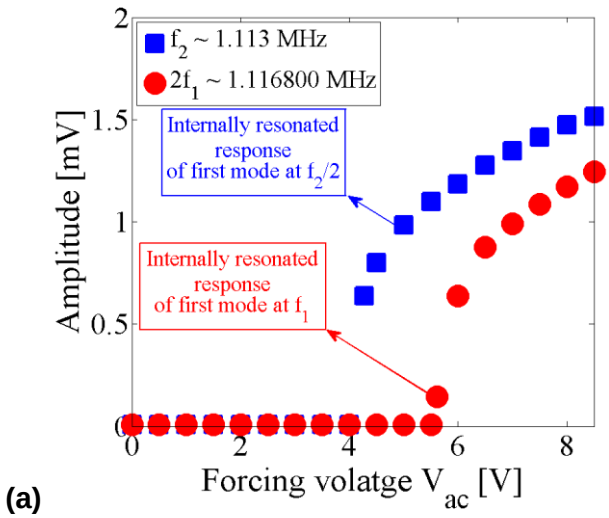

(a)

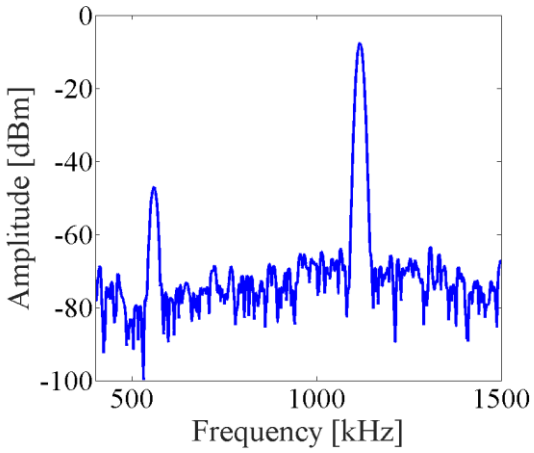

(b)

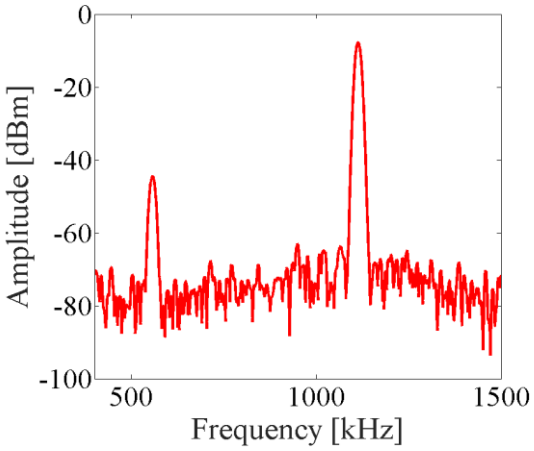

(c)

Figure 4.5. **(a) The measured response of the pendulum mode versus the voltage V_{ac} in the frame-shaped microresonator. Frequency spectrum on the signal analyzer when V_{ac}=7 V and the excitation frequency is set at (b) $2f_1$ and (c) f_2.**

Figure 4.5(a) illustrates the experimentally measured oscillation amplitude of the microresonator at the frequencies f_1 and $f_2/2$ while the drive amplitude V_{ac} is changed and the excitation frequency Ω_r is fixed at the frequencies $2f_1$ and f_2. We observe the signatures of nonlinear mode coupling at frequencies f_1 and $f_2/2$ for the AC drive voltages $V_{ac}\geq$ 5.6 V and $V_{ac}\geq$ 4.2 V, respectively. Beyond these thresholds, the microresonator starts to experience the internal resonance, and the jump occurs. This effect leads to the energy spillover from the saturated mode with a natural frequency f_2 to the mode of natural frequency f_1. To better understand this effect, Figure 4.5(b) and Figure 4.5(c) present the signals saved via the signal analyzer when V_{ac}=7 V and Ω_r is set at $2f_1$ and f_2. As it can be seen in both figures, there are two spikes. The one at the lower frequency belongs to the pendulum mode, and the other one is associated with the spring mode and electrical interferences. This observation also confirms the transfer of energy from the mode with the higher resonant frequency to lower-natural-frequency mode.

The perturbation solutions in Equation (4.42) are simulated, shown in Figure 4.6. The loading setting same as the experiments stated above is chosen. Hence, the nondimensionalized excitation frequency is fixed at $\Omega_1=\omega_2$ (σ_1=0) and $\Omega_1=2\omega_1$ ($\sigma_1=-\sigma_2$) and the nondimensionalized AC load V_{AC} is swept from 0 to $V_{AC}=V_{ac}/\varepsilon$. Upon using the real values for the system parameters, obtained from the experimental measurements, we will observe a jump phenomenon when σ_1=0 for $V_{ac_{critical}}=\varepsilon V_{AC_{critical}}$>3.8 V and $\sigma_1+\sigma_2$=0, for $V_{ac_{critical}}=\varepsilon V_{AC_{critical}}$>4.7 V. We also numerically integrate Equation (4.39) for a_i and β_i (i=1 and 2), and compare the results with the solution of Equations (4.40) and (4.42) which are the steady-state behavior of the response amplitudes. Figure 4.7 illustrates the response amplitudes a_1 (pendulum mode) and a_2 (spring mode) as functions of nondimensionalized forcing voltage V_{AC} for two different cases when $\Omega_1=\omega_2$ (σ_1=0) and $\Omega_1=2\omega_1$ ($\sigma_1=-\sigma_2$), respectively. In both figures, for specific values below an AC voltage threshold, while the amplitude of a_2 of the directly excited mode (spring mode) is proportional to V_{AC}, the amplitude a_1 of the pendulum mode is zero. It implies that the internal resonance is not activated and the nonlinear mode coupling is not triggered. For the excitation voltages higher than the threshold, the amplitude a_2 of the resonantly excited mode is independent of V_{AC}, while the amplitude a_1 of the pendulum mode, which is not directly resonated, depends on V_{AC}. The result confirms the saturation phenomenon in the nonlinear systems incorporating quadratic nonlinearities. These plots show that the

results of numerical integration match accurately with the perturbation solutions, confirming the validity of perturbation analysis.

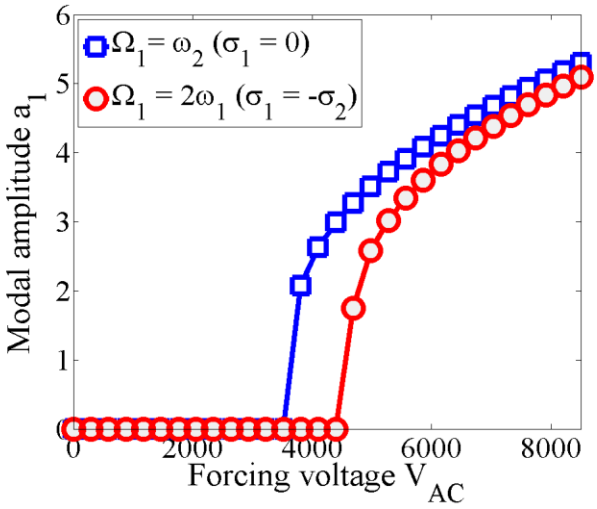

Figure 4.6. The simulation of the amplitudes of response a_1 in the frame-shaped microresonator versus the forcing voltage V_{AC} showing perturbation solutions when σ_1=0 or $\Omega_1=\omega_2$ and $\sigma_1=-\sigma_2$ or $\Omega_1=2\omega_1$.

The experimental and simulated nonlinear frequency response curves are illustrated in Figure 4.8. We sweep the frequency of the AC driving voltage V_{ac} forward and backward around the resonance frequency of the second mode natural frequency f_2 when V_{DC}=80 V, V_{ac}=7.5, 8 and 8.5, and G_{amp}=10 kΩ. We actuate the second mode of vibration at a constant drive voltage V_{ac}. The drive frequency is then varied forward and backward around the frequency f_2 while monitoring and capturing the half subharmonic response of the device in the vicinity of the frequency f_1. It should be mentioned that max-hold function on the signal analyzer was activated to achieve the nonlinear frequency response plots in Figure 4.8(a). The sweep frequency range was set between the frequencies 1.1 MHz-1.13 MHz.

This nonlinear mode coupling corresponds to the characteristics of the systems with 2:1 internal resonance. The behavior is predicted to occur in the presence of quadratic nonlinearities and with the structural modes such that one mode has a natural frequency which is twice the natural frequency of the other mode, i.e., $f_2 \approx 2f_1$. Therefore, the first mode goes into internal resonance. When the frequency ratio is perfectly achieved as exact 2:1, the frequency response curves for a specific range of driving voltages form flat-top curves. However, due to the presence of fabrication nonidealities, it is predictable to

come up with the case where the frequency ratio has some difference, though limited, from 2:1. In this case, nonlinear vibrations can separately occur in two intervals of the excitation frequencies. Splitting the curve is the representation of this non-ideal case where there is detuning between f_2 and $2f_1$ and the frequency ratio is not exactly 2:1. As a result, the nonlinearly coupled vibrations occur in two intervals of the excitation frequency due to small detuning between f_2 and $2f_1$. As it can be seen increasing the AC driving voltages leads to more separation between the resonant peaks. Moreover, the signal goes through half-order subharmonic resonance, and the subharmonic frequency locks to approximately one-half of the forcing frequency.

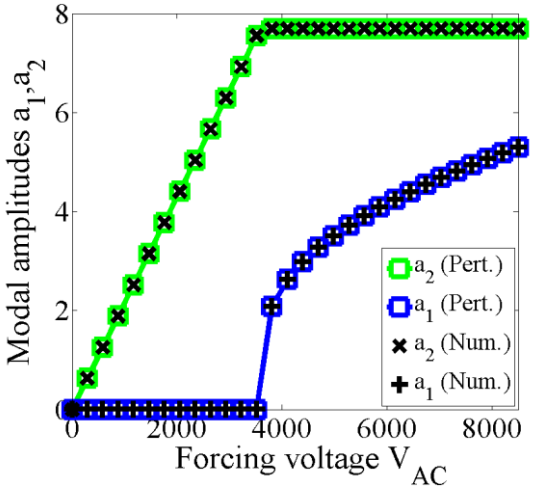

(a)

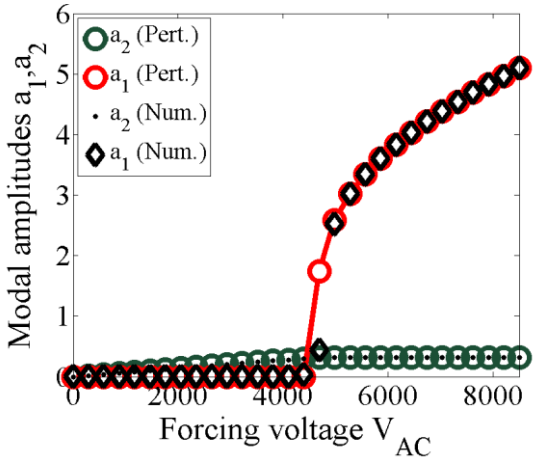

(b)

Figure 4.7. The simulation of the modal amplitudes a_1 and a_2 in the frame-shaped microresonator versus the voltage V_{AC} when (a) $\sigma_1=0$ or $\Omega_1=\omega_2$. (b) $\sigma_1=-\sigma_2$ or $\Omega_1=2\omega_1$. The plots are a typical representation of saturation phenomenon due to 2:1 internal resonance.

It is worth mentioning here that the strong signal that is observed is mainly due to the long capacitive electrodes, the high vacuum within the device package, and the relatively small gap between the device and electrodes. The simulated frequency response curves are demonstrated in Figure 4.8(b). The figure shows the amplitude a_1 versus the detuning forcing parameter σ_1 for the different AC drive levels. The nondimensionalized electrostatic voltages are V_{dc}=80000 and V_{AC}=7500, 8000, and 8500. The values of parameters are chosen to agree with the experiments. The simulation results confirm the existence of the gap between the resonant curves at f_1 and $f_2/2$ in agreement with experimental results, which is because $\sigma_2 \neq 0$.

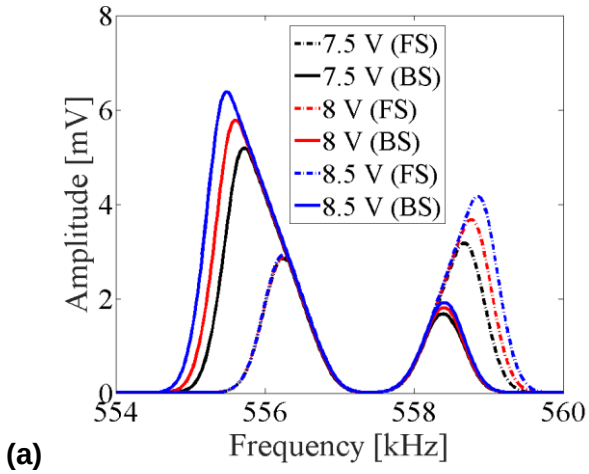

(a)

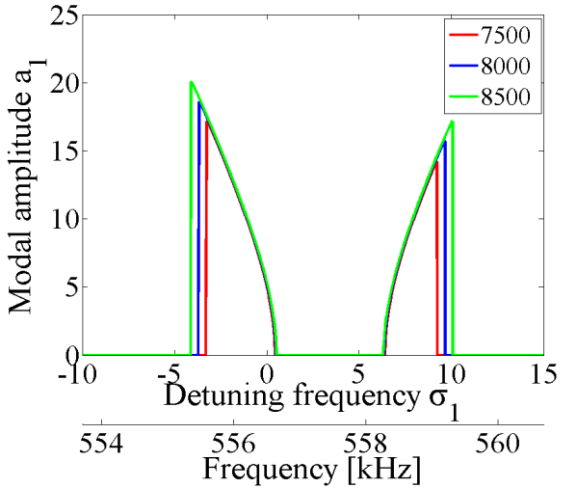

(b)

Figure 4.8. The measured nonlinear frequency transmission responses for the frame-shaped microresonator. (a) Experiment. Due to the frequency ratio of 1.9932, the vibrational amplitudes split. (b) Simulation of the amplitude a_1 versus the detuning forcing parameter σ_1. The separation in the nonlinear modal couplings is due to $\sigma_2 \neq 0$.

4.4. Summary

This chapter reported on the analytical, numerical and experimental investigation on nonlinear mode coupling due to 2:1 internal resonance in a decoupled frame-shaped tuning fork microresonator. We developed a simple 2-DOF dynamical model for each side of the microresonator, by which we can reproduce the nonlinear behavior of our microresonator at resonance by simulation. We studied the possible forced and 2:1 internal resonances to the first order of approximation, that is $\Omega_1 \approx \omega_2$ and $\omega_2 \approx 2\omega_1$, by the method of two-variable expansion perturbation. By this model, we showed that saturation and nonlinear mode coupling of the modes exist in qualitative agreement with the experimental findings. Due to the approximate 2:1 resonance condition, the nonlinear mode coupling occurs in two intervals of the excitation frequency. Finally, the comparison of the perturbation and the numerical solutions with the experimental results confirms that the derived mathematical model qualitatively predicts the dynamical behavior of the microresonator exhibiting 2:1 internal resonance.

Chapter 5.

Dynamics of an H-shaped tuning fork microresonator with nonlinear mode coupling: modeling, simulations, and experiments

In this chapter, the nonlinear dynamics and mode coupling in an H-shaped tuning fork microresonator with internal resonance are examined numerically and experimentally. The device is studied through the lumped mass-spring-damper modeling of two spring-pendulum systems. The equations of motion are derived using Lagrange's energy method. By the method of two-variable expansion perturbation technique, the original 4-DOF system is reduced to an approximate system of amplitude and phase variables. Splitting of the resonance peaks was noticed in the simulated and experimentally obtained nonlinear frequency responses for the sufficiently large drive voltages. The results demonstrated that the perturbation closed-form solutions could qualitatively agree with the experimental findings, confirming the validity of perturbation approach.

5.1. Theory

5.1.1. Governing equations

The schematic drawing of the microresonator was shown in Figure 3.16. The lumped modeling of the device dynamics in nonlinear regime involves some assumptions;

1) According to the FEM modal analysis in CoventorWare©, rotation with respect to the anchor is allowed at either of the tuning fork beams ends. Thus, it makes sense to consider the tuning fork beams on each side of the device as a simply supported beam with an attached H-shaped proof mass in the middle.

2) Each anchor beam can be considered as a cantilever beam.

3) The left and right resonators are assumed to be decoupled.

4) The resonators can rotate with respect to the anchor, caused by large deformation of the suspension beams.

5) The tuning fork beams displace translationally with respect to the anchor beams attached to them.

6) The anchor beams are pinned to the fixed support to allow the rotation at the junction point.

7) The silicon anchors are assumed to be fixed and rigid during entire nonlinear operation of the microresonator. Accordingly, the planar motion of the microdevice can be modeled as a 4-DOF mechanism (see Figure 5.1).

It is perceptible from the schematic that the motion of the microdevice with the masses M_1 and M_2 can be described by using four generalized coordinates $q_1=\theta_1$, $q_2=r_1$, $q_3=\theta_2$ and $q_4=r_2$. The variables r_1 and r_2 describe the extensional motions of the masses M_1 and M_2, respectively. The generalized coordinates θ_1 and θ_2 represent the angular motions of masses M_1 and M_2 along with M_b, respectively. The (X, Y, Z) reference frame is stationary and centered at the point O. The mass M_i represents the mass of the beam of length L_{tf} with the central H-like proof mass. The mass M_b represents the effective mass of two cantilever beams of length L_e where $L_e=L_a-0.5w_{tf}$. The linear and rotational springs and dampers are considered to be present in both spring and pendulum motions. The electrostatic forces F_1 and F_3 are applied to the masses M_1 and M_2, respectively. The capacitive forces F_2 and F_4 stand for the difference between the electrostatic forces imposed on the device by the sense electrodes SE 1 and SE 3, and SE 2 and SE 4, respectively. The constant input angular rate is indicated by Ω_Z.

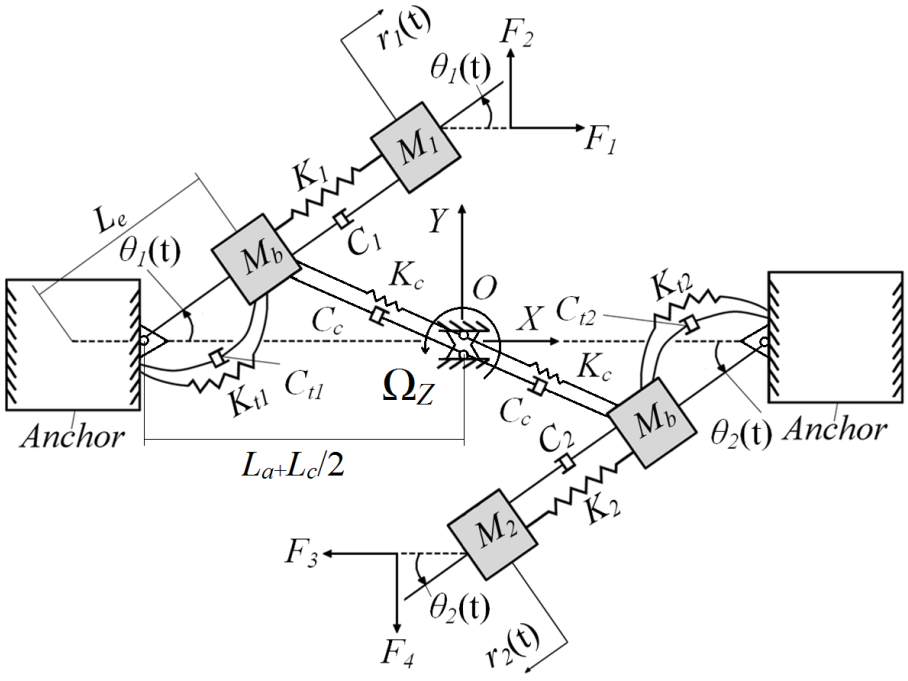

Figure 5.1. Lumped parameter model for the H-shaped tuning fork dynamics.

The positions of the masses M_1, M_b on the left side, M_2, and M_b on the right side, respectively, can be expressed as

$$r_{M_1} = \left(-(L_a + \frac{L_c}{2}) + \left(L_e + r_1(t)\right) cos\left(\theta_1(t)\right)\right)\hat{i} + \left(\left(L_e + r_1(t)\right) sin\left(\theta_1(t)\right)\right)\hat{j} \tag{5.1}$$

$$r_{(M_b)_L} = \left(-(L_a + \frac{L_c}{2}) + L_e\, cos\left(\theta_1(t)\right)\right)\hat{i} + \left(L_e\, sin\left(\theta_1(t)\right)\right)\hat{j} \tag{5.2}$$

$$r_{M_2} = \left((L_a + \frac{L_c}{2}) - \left(L_e + r_2(t)\right) cos\left(\theta_2(t)\right)\right)\hat{i} - \left(\left(L_e + r_2(t)\right) sin\left(\theta_2(t)\right)\right)\hat{j} \tag{5.3}$$

$$r_{(M_b)_R} = \left((L_a + \frac{L_c}{2}) - L_e\, cos\left(\theta_2(t)\right)\right)\hat{i} - \left(L_e\, sin\left(\theta_2(t)\right)\right)\hat{j} \tag{5.4}$$

where $\hat{i}$ and $\hat{j}$ are the unit vectors of the (X, Y, Z)-coordinate reference frame. The velocity vectors can be sorted as

$$\dot{r}_{M_1} = \left(\dot{r}_1(t)\, cos\left(\theta_1(t)\right) - \left(L_e + r_1(t)\right)\left(\dot{\theta}_1(t) + \Omega_Z\right) sin\left(\theta_1(t)\right)\right)\hat{i} + \left(\dot{r}_1(t)\, sin\left(\theta_1(t)\right) + \left(L_e + r_1(t)\right)\left(\dot{\theta}_1(t) + \Omega_Z\right) cos\left(\theta_1(t)\right) - (L_a + \frac{L_c}{2})\Omega_Z\right)\hat{j} \tag{5.5}$$

$$\dot{r}_{(M_b)_L} = \left(-L_e\left(\dot{\theta}_1(t) + \Omega_Z\right) sin\left(\theta_1(t)\right)\right)\hat{i} + \left(L_e\dot{\theta}_1(t)\, cos\left(\theta_1(t)\right) + \Omega_Z\left(L_e\, cos\left(\theta_1(t)\right) - \left(L_a + \frac{L_c}{2}\right)\right)\right)\hat{j} \tag{5.6}$$

$$\dot{r}_{M_2} = \left(\left(L_e + r_2(t)\right)\left(\dot{\theta}_2(t) + \Omega_Z\right) sin\left(\theta_2(t)\right) - \dot{r}_2(t)\, cos\left(\theta_2(t)\right)\right)\hat{i} - \left(\left(L_e + r_2(t)\right)\left(\dot{\theta}_2(t) + \Omega_Z\right) cos\left(\theta_2(t)\right) + \dot{r}_2(t)\, sin\left(\theta_2(t)\right) - (L_a + \frac{L_c}{2})\Omega_Z\right)\hat{j} \tag{5.7}$$

$$\dot{r}_{(M_b)_R} = \left(L_e\left(\dot{\theta}_2(t) + \Omega_Z\right) sin\left(\theta_2(t)\right)\right)\hat{i} + \left(-L_e\dot{\theta}_2(t)\, cos\left(\theta_2(t)\right) + \Omega_Z\left(-L_e\, cos\left(\theta_1(t)\right) + \left(L_a + \frac{L_c}{2}\right)\right)\right)\hat{j} \tag{5.8}$$

The dot represents differentiation with respect to the time *t*. The kinetic and potential energy of the system (KE) and (PE), respectively, are

$$KE = \frac{1}{2}M_1\dot{\mathbf{r}}_{M_1}.\dot{\mathbf{r}}_{M_1} + \frac{1}{2}M_b\,\dot{\mathbf{r}}_{(M_b)_L}.\dot{\mathbf{r}}_{(M_b)_L} + \frac{1}{2}M_2\dot{\mathbf{r}}_{M_2}.\dot{\mathbf{r}}_{M_2} + \frac{1}{2}M_b\,\dot{\mathbf{r}}_{(M_b)_R}.\dot{\mathbf{r}}_{(M_b)_R} \tag{5.9}$$

$$PE = \frac{1}{2}\begin{pmatrix} K_1(r_1(t))^2 + K_{t1}(\theta_1(t))^2 + K_2(r_2(t))^2 + K_{t2}(\theta_2(t))^2 \\ +K_cL_e^2\left((\tan(\theta_1(t)))^2 + (\tan(\theta_2(t)))^2\right) \end{pmatrix} \tag{5.10}$$

Rayleigh's dissipation force (F_d) can also be defined as

$$F_d = \frac{1}{2}\begin{pmatrix} C_1(\dot{r}_1(t))^2 + C_{t1}\left(\dot{\theta}_1(t)\right)^2 + C_2(\dot{r}_2(t))^2 + C_{t2}\left(\dot{\theta}_2(t)\right)^2 + \\ C_cL_e^2\left(\left(\dot{\theta}_1(t)\left(1+\tan^2(\theta_1(t))\right)\right)^2 + \left(\dot{\theta}_2(t)\left(1+\tan^2(\theta_2(t))\right)\right)^2\right) \end{pmatrix} \tag{5.11}$$

The above expressions for the kinetic, potential energy and dissipation forces can be then substituted into Lagrange equations:

$$\left(\frac{\partial L}{\partial \dot{q}_i}\right) - \frac{\partial L}{\partial q_i} + \frac{\partial F_d}{\partial \dot{q}_i} = G_i,\ i=1\text{-}4 \tag{5.12}$$

where *L* is the Lagrangian defined through

$$L = KE\text{-}PE \tag{5.13}$$

and the G_i are the generalized nonconservative forces or moments. Therefore, we get the equations of motion as

$$\begin{aligned} &L_e^2(M_b+M_1)\ddot{\theta}_1(t) + C_{t1}\dot{\theta}_1(t) + K_{t1}\theta_1(t) = \frac{F_2}{\cos(\theta_1(t))}\left(L_e + r_1(t)\right) \\ &-M_1\left(\left(r_1^2(t) + 2L_er_1(t)\right)\ddot{\theta}_1(t) + 2\left(L_e + r_1(t)\right)\dot{r}_1(t)\dot{\theta}_1(t)\right) \\ &-L_e^2\left(K_c\frac{\sin(\theta_1(t))}{\cos^3(\theta_1(t))} + C_c\frac{\dot{\theta}_1(t)}{\cos^4(\theta_1(t))}\right) - \left(2M_1\dot{r}_1(t)\left(L_e + r_1(t)\right)\right)\Omega_Z \\ &+\left(\left(L_a + \frac{L_c}{2}\right)\sin(\theta_1(t))\left(M_1\left(L_e + r_1(t)\right) + M_bL_e\right)\right)\Omega_Z^2 \\ &-\left(M_1\left(L_e + r_1(t)\right)^2 + M_bL_e^2 - \left(M_1\left(L_e + r_1(t)\right) + M_bL_e\right)\cos(\theta_1(t))\left(L_a + \frac{L_c}{2}\right)\right)\dot{\Omega}_Z \end{aligned} \tag{5.14}$$

$$M_1\ddot{r}_1(t)+C_1\dot{r}_1(t)+K_1r_1(t)=M_1\left(L_e+r_1(t)\right)\dot{\theta}_1^2(t)+\frac{F_1}{\cos\left(\theta_1(t)\right)}$$
$$+2M_1\left(L_e+r_1(t)\right)\dot{\theta}_1(t)\Omega_Z$$
$$+\left(M_1\left(L_a+\frac{L_c}{2}\right)\sin\left(\theta_1(t)\right)\right)\dot{\Omega}_Z+M_1\left(L_e+r_1(t)-\cos\left(\theta_1(t)\right)\left(L_a+\frac{L_c}{2}\right)\right)\Omega_Z^2 \quad (5.15)$$

$$L_e^2(M_b+M_2)\ddot{\theta}_2(t)+C_{t2}\dot{\theta}_2(t)+K_{t2}\theta_2(t)=\frac{F_4}{\cos\left(\theta_2(t)\right)}\left(L_e+r_2(t)\right)$$
$$-M_2\left(\left(r_2^2(t)+2L_er_2(t)\right)\ddot{\theta}_2(t)+2\left(L_e+r_2(t)\right)\dot{r}_2(t)\dot{\theta}_2(t)\right)$$
$$-L_e^2\left(K_c\frac{\sin\left(\theta_2(t)\right)}{\cos^3\left(\theta_2(t)\right)}+C_c\frac{\dot{\theta}_2(t)}{\cos^4\left(\theta_2(t)\right)}\right)-\left(2M_2\dot{r}_2(t)\left(L_e+r_2(t)\right)\right)\Omega_Z$$
$$+\left(\left(L_a+\frac{L_c}{2}\right)\sin\left(\theta_2(t)\right)\left(M_2\left(L_e+r_2(t)\right)+M_bL_e\right)\right)\Omega_Z^2$$
$$-\left(M_2\left(L_e+r_2(t)\right)^2+M_bL_e^2-\left(M_2\left(L_e+r_2(t)\right)+M_bL_e\right)\cos\left(\theta_2(t)\right)\left(L_a+\frac{L_c}{2}\right)\right)\dot{\Omega}_Z \quad (5.16)$$

$$M_2\ddot{r}_2(t)+C_2\dot{r}_2(t)+K_2r_2(t)=M_2\left(L_e+r_2(t)\right)\dot{\theta}_2^2(t)-\frac{F_3}{\cos\left(\theta_2(t)\right)}$$
$$+2M_2\left(L_e+r_2(t)\right)\dot{\theta}_2(t)\Omega_Z$$
$$+\left(M_2\left(L_a+\frac{L_c}{2}\right)\sin\left(\theta_2(t)\right)\right)\dot{\Omega}_Z+M_2\left(L_e+r_2(t)-\cos\left(\theta_2(t)\right)\left(L_a+\frac{L_c}{2}\right)\right)\Omega_Z^2 \quad (5.17)$$

Where

$$F_1=\frac{1}{2}\left(V_{DC}+V_{ac}\cos(\Omega_rt)\right)^2l_1\frac{p_0t_{Si}}{\left(g-r_1(t)\right)^2},\ F_3=\frac{1}{2}\left(V_{DC}+V_{ac}\cos(\Omega_rt)\right)^2l_1\frac{p_0t_{Si}}{\left(g-r_2(t)\right)^2}$$

$$F_2=\frac{1}{2}V_{DC}^2p_0t_{Si}L_el_2\left(1+\left(\tan\left(\theta_1(t)\right)\right)^2\right)\left(\frac{1}{\left(g-L_e\tan\left(\theta_1(t)\right)\right)^2}+\frac{1}{\left(g+L_e\tan\left(\theta_1(t)\right)\right)^2}\right)$$

$$F_4=\frac{1}{2}V_{DC}^2p_0t_{Si}L_el_2\left(1+\left(\tan\left(\theta_2(t)\right)\right)^2\right)\left(\frac{1}{\left(g-L_e\tan\left(\theta_2(t)\right)\right)^2}+\frac{1}{\left(g+L_e\tan\left(\theta_2(t)\right)\right)^2}\right)$$

$$M_1=M_2=M_{Proof\,mass}+M_{tf\,beam}=t_{Si}\rho_{Si}(2h_2w_2+h_1w_1+L_{tf}w_{tf}),\ M_b=0.4714t_{Si}\rho_{Si}L_ew_a$$

$$\omega_{n_1}=2\pi\left(\left(K_{t1}+K_cL_e^2\right)/L_e^2(M_1+M_b)\right)^{1/2}=\left(K_{t1eff}/L_e^2(M_1+M_b)\right)^{1/2},\ \omega_{n_2}=2\pi(K_1/M_1)^{1/2}$$

$$\omega_{n_3}=2\pi\left(\left(K_{t2}+K_cL_e^2\right)/L_e^2(M_2+M_b)\right)^{1/2}=\left(K_{t2eff}/L_e^2(M_2+M_b)\right)^{1/2},\ \omega_{n_4}=2\pi(K_2/M_2)^{1/2}$$

$$c_1=\omega_{n_1}\omega_{n_2}\frac{\left(\frac{\omega_{n_2}}{Q_1}\right)-\left(\frac{\omega_{n_1}}{Q_2}\right)}{\left(\omega_{n_2}\right)^2-\left(\omega_{n_1}\right)^2},\ d_1=\frac{\left(\frac{\omega_{n_2}}{Q_2}\right)-\left(\frac{\omega_{n_1}}{Q_1}\right)}{\left(\omega_{n_2}\right)^2-\left(\omega_{n_1}\right)^2}$$

$$c_2=\omega_{n_3}\omega_{n_4}\frac{\left(\frac{\omega_{n_4}}{Q_3}\right)-\left(\frac{\omega_{n_3}}{Q_4}\right)}{\left(\omega_{n_4}\right)^2-\left(\omega_{n_3}\right)^2},\ d_2=\frac{\left(\frac{\omega_{n_4}}{Q_4}\right)-\left(\frac{\omega_{n_3}}{Q_3}\right)}{\left(\omega_{n_4}\right)^2-\left(\omega_{n_3}\right)^2}$$

$$\begin{bmatrix} C_j \\ C_{tj} \end{bmatrix} = c_j \begin{bmatrix} M_j & 0 \\ 0 & (M_j+M_b)L_e^2 \end{bmatrix} + d_j \begin{bmatrix} K_j & 0 \\ 0 & K_{tj}+K_c L_e^2 \end{bmatrix}, \; j=1 \text{ and } 2$$

where p_0 is the permittivity of the space (8.85×10^{-12} (F/m)); t_{Si} is the thickness of silicon device layer; ρ_{Si} is the mass density of silicon layer (2330 Kg/m^3); V_{DC} is the DC bias voltage applied to the sense and drive electrodes; V_{ac} is the amplitude of the AC driving voltage applied to the drive electrodes, and Ω_r is the frequency of the AC voltage signal. The Q_i stands for the quality factor corresponding to the i^{th}-mode, i=1-4. The translational (C_1 and C_2) and rotational (C_{t1} and C_{t2}) damping coefficients are estimated using Rayleigh's damping equation, stated above. The linearized natural frequencies of pendulum-mode are specified as ω_{n_1}, and ω_{n_3} and the corresponding spring-mode resonant frequencies of the system are defined by ω_{n_2} and ω_{n_4}, respectively. The device design parameters, e.g., w_1 and h_1, were described in Table 3.4. Based on the symmetry and the assumed uncoupled nature of the microresonator, the perturbation closed-form solutions are extracted for the left resonator.

5.1.2. The two-variable expansion perturbation analysis

The following equations represent the scaled and nondimensionalized equations of motion

$$\left.\begin{aligned}
&\ddot{\psi}_1+\omega_1^2\psi_1+\varepsilon\begin{pmatrix} 2m_1\dot{\rho}_1\dot{\psi}_1+2m_1\rho_1\ddot{\psi}_1+\mu_{t1}\dot{\psi}_1 \\ +2\ddot{\varphi}m_1\rho_1-\ddot{\varphi}m_1\rho_1\dfrac{\left(L_a+\frac{L_c}{2}\right)}{L_e}+2m_1\dot{\rho}_1\dot{\varphi} \end{pmatrix} \\
&+\left(1-\frac{\left(L_a+\frac{L_c}{2}\right)}{L_e}\right)\ddot{\varphi}+\varepsilon^2 m_1\begin{pmatrix} \rho_1^2\ddot{\varphi}+\rho_1\left(\rho_1\ddot{\psi}_1+2\dot{\rho}_1\dot{\psi}_1\right) \\ +2\dot{\rho}_1\rho_1\dot{\varphi}-\dfrac{\left(L_a+\frac{L_c}{2}\right)}{L_e}\psi_1\dot{\varphi}^2 \end{pmatrix} \\
&=p_0t_{Si}\frac{l_2}{(M_1+M_b)\Omega^2g^2}V_{dc}^2\left(\rho_1\varepsilon^2+\varepsilon\right) \\
&\ddot{\rho}_1+\omega_2^2\rho_1+\varepsilon\left(\mu_1\dot{\rho}_1-\dot{\psi}_1^2-\frac{\left(L_a+\frac{L_c}{2}\right)}{L_e}\psi_1\ddot{\varphi}+\left(\frac{\left(L_a+\frac{L_c}{2}\right)}{L_e}-1\right)\dot{\varphi}^2-2\dot{\psi}_1\dot{\varphi}\right) \\
&-\varepsilon^2\left(2\rho_1\dot{\varphi}\dot{\psi}_1+\rho_1\dot{\psi}_1^2+\rho_1\dot{\varphi}^2\right) \\
&=p_0t_{Si}l_1\left(V_{dc}+V_{AC}\cos(\Omega_1\tau)\right)^2\left(\frac{\varepsilon^2\rho_1}{M_1g^3\Omega^2}+\frac{\varepsilon}{2M_1L_eg^2\Omega^2}\right)
\end{aligned}\right\} \quad (5.18)$$

where

$$r_1(t)=P_1(\tau)L_e,\ \theta_1(t)=\Theta_1(\tau)$$

$$t=\frac{\tau}{\Omega},\ \frac{d}{dt}=\Omega\frac{d}{d\tau},\ \frac{d^2}{dt^2}=\Omega^2\frac{d^2}{d\tau^2}$$

$$\Theta_1(\tau)=\varepsilon\psi_1(\tau),\ P_1(\tau)=\varepsilon\rho_1(\tau),\ \Omega_Z=\varepsilon\dot{\varphi}(\tau),\ V_{ac}=\varepsilon V_{AC},\ V_{DC}=\varepsilon V_{dc},\ \gamma_{t1}=\varepsilon\mu_{t1},\ \gamma_1=\varepsilon\mu_1$$

$$\omega_1=\frac{\sqrt{\frac{K_{t1}+K_cL_e^2}{(M_1+M_b)L_e^2}}}{\Omega},\ \omega_2=\frac{\sqrt{\frac{K_1}{M_1}}}{\Omega},\ m_1=\frac{M_1}{M_1+M_b},\ \Omega_1=\frac{\Omega_r}{\Omega}$$

$$\gamma_{t1}=\frac{C_{t1}+C_cL_e^2}{(M_1+M_b)L_e^2\Omega}=\frac{C_{t1eff}}{(M_1+M_b)L_e^2\Omega},\gamma_1=\frac{C_1}{M_1\Omega}$$

In the above equation, Ω is the nondimensionalizing frequency, and ε is a small dimensionless parameter, $0<\varepsilon\ll 1$, expressing the order of nonlinearity and coupling. The method of two-variable expansion is used to obtain an approximate solution for Equations $(5.18)_{1,2}$ in case of the external resonance ($\Omega_1\approx\omega_2$) and the 2:1 internal resonance ($\omega_2\approx 2\omega_1$). To describe how close the frequencies are to the resonance conditions we introduce detuning parameters σ_1 and σ_2:

$$\Omega_1=\omega_2+\varepsilon\sigma_1,\ \omega_2=2\omega_1+\varepsilon\sigma_2 \tag{5.19}$$

where σ_1 is called the external detuning parameter; σ_2 denotes the internal detuning parameter. In the two-variable expansion perturbation method, the independent variable τ is replaced by two new variables ξ, and η, such that

$$\xi=\tau,\ \eta=\varepsilon\tau \tag{5.20}$$

where ξ is a stretched time variable τ, and η is a slow time variable. The fast scale ξ is associated with the relatively rapid changes in response, and the slow scale η corresponds to the relatively low changes in amplitudes and phases. We seek a set of solutions for Equation (5.18) for small but finite ψ_1 and ρ_1 in the form of

$$\psi_1=\psi_{1_0}+\varepsilon\psi_{1_1}+O(\varepsilon^2),\ \rho_1=\rho_{1_0}+\varepsilon\rho_{1_1}+O(\varepsilon^2) \tag{5.21}$$

Derivatives with respect to τ are then transformed into

$$\frac{d}{d\tau}=\frac{\partial}{\partial\xi}+\varepsilon\frac{\partial}{\partial\eta}+O(\varepsilon^2),\ \frac{d^2}{d\tau^2}=\frac{\partial^2}{\partial\xi^2}+2\varepsilon\frac{\partial^2}{\partial\xi\partial\eta}+O(\varepsilon^2) \tag{5.22}$$

where $O(\varepsilon^2)$ represents the higher order of ε terms. Substituting these expressions into Equation (5.18) and equating coefficients of equal powers of ε lead to

For order ε^0

$$\psi_{1_{0\xi\xi}}+\omega_1^2\psi_{1_0}=\frac{\left(1-\left(L_a+\frac{L_c}{2}\right)\right)}{L_e}\varphi_{\zeta\zeta}=0,\ \rho_{1_{0\xi\xi}}+\omega_2^2\rho_{1_0}=0 \tag{5.23}$$

For order ε

$$\left.\begin{aligned}
&\psi_{1_{1\xi\xi}}+\omega_1^2\psi_{1_1}=-2\psi_{1_{0\xi\eta}}-\mu_{t1}\psi_{1_{0\xi}}-2m_1\left(\rho_{1_0}\psi_{1_{0\xi\xi}}+\rho_{1_{0\xi}}\psi_{1_{0\xi}}\right)\\
&\frac{p_0t_{Si}l_2}{(M_1+M_b)\Omega^2g^2}V_{dc}^2-2m_1\left(\rho_{1_{0\xi}}\varphi_\zeta+\left(\frac{L_a+\frac{L_c}{2}}{L_e}\right)\rho_{1_0}\varphi_{\zeta\zeta}\right)^2\\
\rho_{1_{1\xi\xi}}+\omega_2^2\rho_{1_1}=&\left(\psi_{1_{0\xi}}\right)^2-\mu_1\rho_{1_{0\xi}}-2\rho_{1_{0\xi\eta}}+\left(1-\left(\frac{L_a+\frac{L_c}{2}}{L_e}\right)\right)(\varphi_\zeta)^2+2\varphi_\zeta\psi_{1_{0\xi}}\\
&+\left(\frac{L_a+\frac{L_c}{2}}{L_e}\right)\psi_{1_0}\varphi_{\zeta\zeta}+\frac{p_0t_{Si}l_1}{2M_1L_e(g\Omega)^2}\left(\begin{matrix}2V_{dc}V_{AC}\cos(\Omega_1\tau)+\\V_{dc}^2+V_{AC}^2(\cos(\Omega_1\tau))^2\end{matrix}\right)
\end{aligned}\right\} \tag{5.24}$$

where the sub-subscripts represent partial derivatives. The solutions of Equations $(5.23)_{1,2}$ can be written in the form:

$$\left.\begin{aligned}\psi_{1_0}&=k_1(\eta)\sin(\omega_1\xi)+k_2(\eta)\cos(\omega_1\xi)\\ \rho_{1_0}&=k_3(\eta)\sin(\omega_2\xi)+k_4(\eta)\cos(\omega_2\xi)\end{aligned}\right\} \tag{5.25}$$

where

$$\left.\begin{aligned}k_1(\eta)&=a_1(\eta)\sin(\alpha_1(\eta)),\ k_2(\eta)=a_1(\eta)\cos(\alpha_1(\eta))\\ k_3(\eta)&=a_2(\eta)\sin(\alpha_2(\eta)),\ k_4(\eta)=a_2(\eta)\cos(\alpha_2(\eta))\end{aligned}\right\} \tag{5.26}$$

In these equations a_n and α_n are real functions of η. This transformation makes it possible to achieve the secular-term equations more conveniently. Equation (5.25) can be then rewritten as:

$$\left.\begin{aligned}\psi_{1_0}&=a_1(\eta)\cos(\omega_1\xi-\alpha_1(\eta))\\ \rho_{1_0}&=a_2(\eta)\cos(\omega_2\xi-\alpha_2(\eta))\end{aligned}\right\} \tag{5.27}$$

We now substitute Equations $(5.27)_{1,2}$ into Equations $(5.24)_{1,2}$, suppressing the secular terms $\sin(\omega_i\xi)$ and $\cos(\omega_i\xi)$ in Equations $(5.24)_{1,2}$, where i=1 and 2. Note that we need to write

$$\left.\begin{aligned} \cos(\Omega_1\xi) &= \cos(\omega_2\xi + \sigma_1\eta) = \cos(\omega_2\xi)\cos(\sigma_1\eta) - \sin(\omega_2\xi)\sin(\sigma_1\eta) \\ \cos(\omega_2\xi) &= \cos(2\omega_1\xi + \sigma_2\eta) = \cos(2\omega_1\xi)\cos(\sigma_2\eta) - \sin(2\omega_1\xi)\sin(\sigma_2\eta) \end{aligned}\right\} \tag{5.28}$$

The functions a_n and α_n are to be determined by satisfying the solvability conditions. The form of solvability conditions depends on the resonance conditions, i.e., an internal resonance if $\omega_2 \approx 2\omega_1$ and an external resonance if $\Omega_1 \approx \omega_2$. The solvability conditions (the conditions for the elimination of secular terms) can be written as

$$\left.\begin{aligned} \alpha_{1\eta} &= \frac{1}{2} m_1 a_2 (\omega_1 - \omega_2)\cos(\beta_1) \\ a_{1\eta} &= -\frac{\mu_{t1}}{2} a_1 + \frac{1}{2} m_1 (\omega_1 - \omega_2) a_1 a_2 \sin(\beta_1) \\ \alpha_{2\eta} &= -\frac{\omega_1^2}{4a_2\omega_2} a_1^2 \cos(\beta_1) + \frac{p_0 t_{Si} l_1}{2M_1 L_e (g\Omega)^2 \omega_2 a_2} V_{dc} V_{AC} \cos(\beta_2) \\ a_{2\eta} &= -\frac{\mu_1}{2} a_2 + \frac{\omega_1^2}{4\omega_2} a_1^2 \sin(\beta_1) + \frac{p_0 t_{Si} l_1}{2M_1 L_e (g\Omega)^2 \omega_2} V_{dc} V_{AC} \sin(\beta_2) \end{aligned}\right\} \tag{5.29}$$

where

$$\beta_1 = 2\alpha_1 - \alpha_2 + \sigma_2\eta,\ \beta_2 = \alpha_2 + \sigma_1\eta \tag{5.30}$$

Differentiating Equation (5.30) with respect to η, and substituting Equation (5.29) and Equation (41) into Equation (5.30), we have a system of ordinary differential equations of amplitude a_n and phase β_n for n= 1 and 2.

$$\left.\begin{aligned} \beta_{1\eta} &= m_1 a_2 (\omega_1 - \omega_2)\cos(\beta_1) + \frac{\omega_1^2}{4a_2\omega_2} a_1^2 \cos(\beta_1) - \frac{p_0 t_{Si} l_1}{2M_1 L_e (g\Omega)^2 \omega_2 a_2} V_{dc} V_{AC} \cos(\beta_2) + \sigma_2 \\ a_{1\eta} &= -\frac{\mu_{t1}}{2} a_1 + \frac{1}{2} m_1 (\omega_1 - \omega_2) a_1 a_2 \sin(\beta_1) \\ \beta_{2\eta} &= -\frac{\omega_1^2}{4a_2\omega_2} a_1^2 \cos(\beta_1) + \frac{p_0 t_{Si} l_1}{2M_1 L_e (g\Omega)^2 \omega_2 a_2} V_{dc} V_{AC} \cos(\beta_2) + \sigma_1 \\ a_{2\eta} &= -\frac{\mu_1}{2} a_2 + \frac{\omega_1^2}{4\omega_2} a_1^2 \sin(\beta_1) + \frac{p_0 t_{Si} l_1}{2M_1 L_e (g\Omega)^2 \omega_2} V_{dc} V_{AC} \sin(\beta_2) \end{aligned}\right\} \tag{5.31}$$

To obtain the steady-state solutions, solving $a_{1\eta}=a_{2\eta}=\beta_{1\eta}=\beta_{2\eta}=0$, we have two possible cases. The first case is

$$\left.\begin{aligned} a_1 = 0, \qquad a_2 &= \frac{p_0 t_{Si} l_1 V_{dc} V_{AC}}{M_1 \omega_2 L_e (g\Omega)^2 \sqrt{4\sigma_1^2 + \mu_1^2}} \\ \beta_1 &= \pi - cos^{-1}\left(\frac{(\sigma_1 + \sigma_2) M_1 \omega_2 L_e (g\Omega)^2 \sqrt{4\sigma_1^2 + \mu_1^2}}{p_0 t_{Si} l_1 V_{dc} V_{AC} m_1 (\omega_1 - \omega_2)}\right) \\ \beta_2 &= tan^{-1}\left(\frac{\mu_1}{\sqrt{4\sigma_1^2 + \mu_1^2}}, -\frac{2\sigma_1}{\sqrt{4\sigma_1^2 + \mu_1^2}}\right) \end{aligned}\right\} \tag{5.32}$$

The first case implies the solutions to that of the linear systems, as follows

$$\left.\begin{aligned} \psi_1 &= O(\varepsilon) \\ \rho_1 &= \frac{p_0 t_{Si} l_1 V_{dc} V_{AC}}{M_1 \omega_2 L_e (g\Omega)^2 \sqrt{4\sigma_1^2 + \mu_1^2}} cos(\Omega_1 \tau - \beta_2) + O(\varepsilon) \end{aligned}\right\} \tag{5.33}$$

The second case is

$$\left.\begin{aligned} a_1 &= -\frac{1}{\omega_1 g\Omega}\left[\frac{2\left(\Gamma_1 \pm \sqrt{(\Gamma_2 + \Gamma_3)(\Gamma_2 - \Gamma_3)}\right)}{M_1 m_1 L_e (\omega_1 - \omega_2)}\right]^{\frac{1}{2}} \\ a_2 &= \frac{\sqrt{(\mu_{t1})^2 + (\sigma_1 + \sigma_2)^2}}{m_1 (\omega_2 - \omega_1)} \\ \beta_1 &= tan^{-1}\left(-\frac{\mu_{t1}}{\sqrt{(\mu_{t1})^2 + (\sigma_1 + \sigma_2)^2}}, \frac{\sigma_1 + \sigma_2}{\sqrt{(\mu_{t1})^2 + (\sigma_1 + \sigma_2)^2}}\right) \\ \beta_2 &= -tan^{-1}\left(\frac{(\sigma_1 + \sigma_2)\Gamma_3 - \mu_{t1}\sqrt{(\Gamma_2 + \Gamma_3)(\Gamma_2 - \Gamma_3)}}{\mu_{t1}\Gamma_3 + (\sigma_1 + \sigma_2)\sqrt{(\Gamma_2 + \Gamma_3)(\Gamma_2 - \Gamma_3)}}\right) \end{aligned}\right\} \tag{5.34}$$

where

$$\Gamma_1 = M_1 \omega_2 L_e (g\Omega)^2 \left(\mu_1 \mu_{t1} - 2\sigma_1 (\sigma_1 + \sigma_2)\right), \; \Gamma_2 = p_0 t_{Si} V_{dc} V_{AC} (\omega_1 - \omega_2) m_1 l_1$$
$$\Gamma_3 = M_1 \omega_2 L_e (g\Omega)^2 \left((\mu_1 + 2\mu_{t1})\sigma_1 + \mu_1 \sigma_2\right) \tag{5.35}$$

Hence, the steady-state responses for this case, with the use of Equations (5.34) and (5.35), are

$$\left.\begin{aligned} \psi_1 &= -\frac{1}{\omega_1 g\Omega}\left[\frac{2\left(\Gamma_1 \pm \sqrt{(\Gamma_2 + \Gamma_3)(\Gamma_2 - \Gamma_3)}\right)}{M_1 m_1 L_e (\omega_1 - \omega_2)}\right]^{\frac{1}{2}} cos\left(\frac{1}{2}(\Omega_1 \tau - \beta_1 - \beta_2)\right) + O(\varepsilon) \\ \rho_1 &= \frac{\sqrt{(\mu_{t1})^2 + (\sigma_1 + \sigma_2)^2}}{m_1 (\omega_2 - \omega_1)} cos(\Omega_1 \tau - \beta_2) + O(\varepsilon) \end{aligned}\right\} \tag{5.36}$$

The solutions for the second case correspond to the nonlinear behavior of the system when the nonlinear internal resonance occurs. The system parameters utilized for simulations can be found in Table 5.1. It should be mentioned that these values are estimated according to the experimental measurements.

Table 5.1. System parameter values for the H-shaped microresonator.

Symbol	Value	Symbol	Value
ω_1	1	M_1	1.32×10^{-9} Kg
ω_2	2.001	C_1	1.63×10^{-6} N/m.sec
Ω	ω_{n_1}	C_{t1eff}	1.62×10^{-14} N.m/sec
m_1	0.97	K_1	6.55×10^{4} N/m
μ_1	0.35	K_{t1eff}	3.93×10^{-4} N.m
μ_{t1}	0.14	M_b	4.31×10^{-11} Kg
ε	0.001	L_e	152 μm
σ_2	1	g	1.75 μm

5.2. Experimental setups and resonance characterization

The natural frequencies of the microresonator (f_1 and f_2) and the quality factors (Q_1 and Q_2) for the pendulum- and spring modes are estimated using the test-bed shown in Figure 5.2.

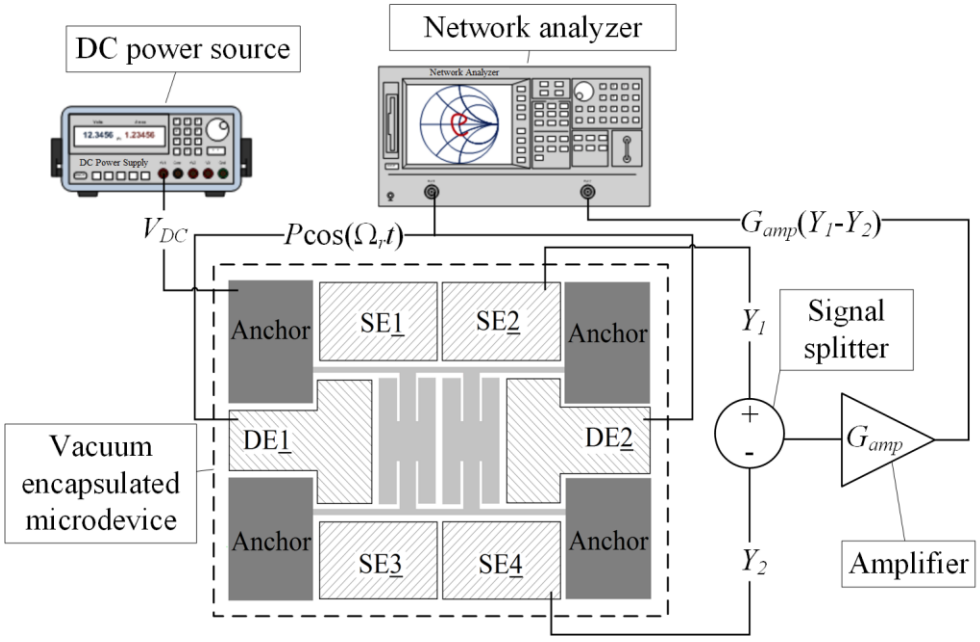

Figure 5.2. The experimental configuration to achieve the natural frequencies and the quality factors of the H-shaped microresonator.

The setup comprises of (1) a vacuum encapsulated microresonator, (2) a DC power source (*Keysight, Model: B2901A*) with the output DC voltage of V_{DC}, (3) a vector network analyzer (*Rohde & Schwarz, Model: ZVB 4*) with the output signal of power P in dBm, (4) a signal splitter (*Mini-Circuits SPLITTER, Model: ZFSCJ-2-2-S*) and (5) a lock-in

amplifier (*Zurich Instruments, Model: HF2LI*) with a preamp gain of G_{amp}. In this figure, the signals Y_1 and Y_2 are the capacitance change captured via SE 2 and SE 4, respectively. The required setting to determine the natural frequencies and the Q-factors is: V_{DC}=100 V, P =5 dBm and G_{amp}=10 kΩ. Figure 5.3 shows the resonant modes of the device are located at f_1= 560.28 kHz with Q_1=6.9k (pendulum mode) and f_2=1.12235 MHz with Q_2=5.7k (spring mode). According to these frequencies, the frequency ratio between f_2 and f_1 can be calculated as f_2/f_1 =2.003≈2.

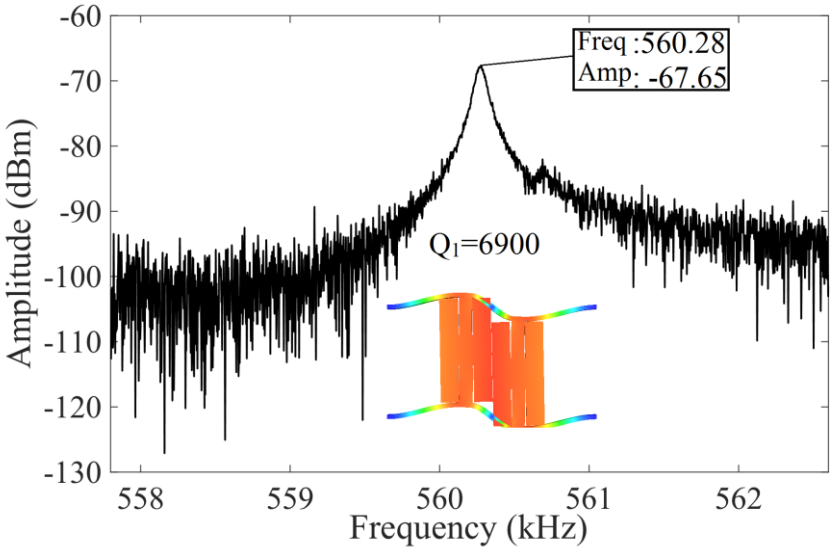

(a)

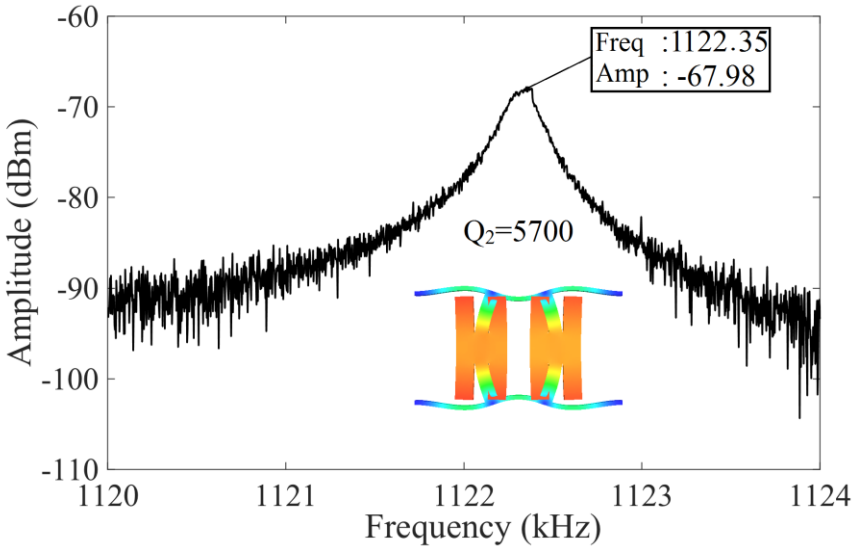

(b)

Figure 5.3. The experimentally measured frequency spectrum for the H-shaped microresonator. The natural frequency and the quality factor of (a) the pendulum mode and (b) the spring mode.

The nonlinear mode coupling caused by the 2:1 internal resonance is evaluated through the saturation figure and the nonlinear frequency response curves. A series of experiments have to be accomplished through the experimental configuration demonstrated in Figure 5.4. The setup consists of (1) a vacuum encapsulated microresonator; (2) a DC power source (*Keysight, Model: B2901A*) to bias the microresonator; (3) a pulse function arbitrary generator (*Agilent Technologies, Model: 81150A*) to provide harmonic and sweep AC signals, i.e., $V_{ac}\cos(\Omega_r t)$, through the drive electrodes DE 1 and DE 2; (4) a signal splitter (*Mini-Circuits SPLITTER, Model: ZFSCJ-2-2-S*) to measure the output signal differentially and double the total capacitance change (improving the signal processing); (5) a lock-in amplifier (*Zurich Instruments, Model: HF2LI*) to boost the output current captured by the sense electrodes SE 2 and SE 4; (6) a signal analyzer (*Agilent Technologies, Model: N9000A*) to monitor the sensed signals in frequency domain.

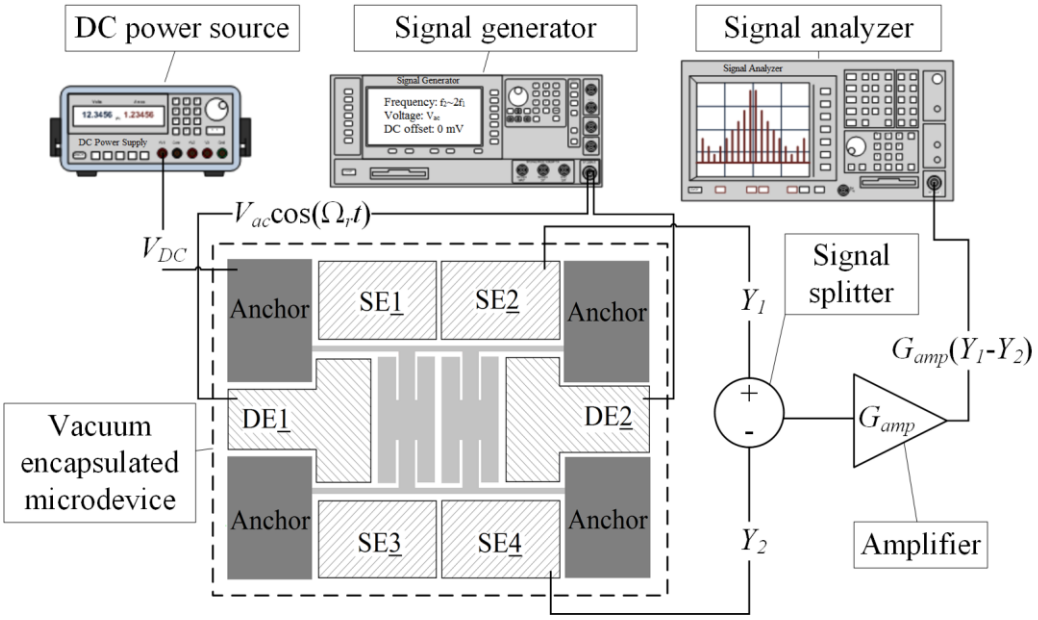

Figure 5.4. The experimental setup to obtain saturation figure and perform frequency sweeps for the H-shaped microresonator.

5.3. Results and discussion

Multiple experiments were performed to reveal the intended 2:1 internal resonance and nonlinear mode coupling in the microresonator. Figure 5.5 exhibits the experimental and simulated half-order subharmonic response of the pendulum mode of the device as

the drive voltage amplitude is increased and the frequency of excitation is fixed at $f_2 \approx 2f_1$ (experiment) or $\omega_2 \approx 2\omega_1$ (simulation). For tests, we set V_{DC}=100 V, V_{ac} =0-4.5 V and G_{amp}=10 kΩ. Figure 5.5(a) shows the amplitude of the spike generated at half the excitation frequency (i.e., $f_2/2 \approx f_1$) versus the AC forcing voltage. As it can be seen the device is quickly driven to the nonlinear regime where the 2:1 internal resonance is triggered by the amplitude of $V_{ac} \geq 1$ V and Ω_r =1.120448 MHz$\approx 2f_1$. Therefore, we spot signatures of nonlinear mode coupling due to the saturation phenomenon. This phenomenon leads to spill over of energy from the higher- frequency mode to the mode with the lower natural frequency. To obtain the numerical results, we have used the values of the system parameters in Table 5.1. The steady-state solution amplitude a_1 in Equation (5.34) is used to achieve the simulation results illustrated in Figure 5.5(b). The figure demonstrates the modal amplitude a_1 versus the nondimensionalized AC drive voltage V_{AC} when V_{dc}=100000 and σ_2=-σ_1 (Ω_1=2ω_1). Upon using the real values for the system parameters, obtained from experimental measurements stated in Table 5.1, we can notice the activation of the nonlinear mode coupling by a response jump at $V_{AC} \geq 923$.

We also numerically integrate Equations $(5.31)_{1\text{-}4}$ for a_i and β_i (i=1 and 2), and compare the results with the steady-states solutions from the perturbation analysis Equations (5.32) and (5.34). Using these equations, we have plotted the response curves shown in, Figure 5.6, where a_1 (pendulum mode) and a_2 (spring mode) are the modal amplitudes, and V_{AC} is the amplitude of the nondimensionalized AC harmonic voltage. For specific values of the excitation below a threshold, while the amplitude of a_2 of the directly excited mode (spring mode) is proportional to V_{AC}, the amplitude a_1 of the pendulum mode is zero. The finding implies that the internal resonance is not activated and the nonlinear mode coupling is not triggered. For the excitation voltages higher than the threshold, the amplitude a_2 of the resonantly excited mode is independent of V_{AC}, while the amplitude a_1 of the pendulum mode, which is not directly resonated, depends on V_{AC}. The dynamical behavior implies the saturation phenomenon in the 2:1 internally resonant systems. The similar behavior between the experimental and simulation results tell us that the approximate perturbation solutions reflect the response of the microresonator very well. Moreover, the results of numerical integration match accurately with the perturbation solutions, confirming the validity of perturbation solutions.

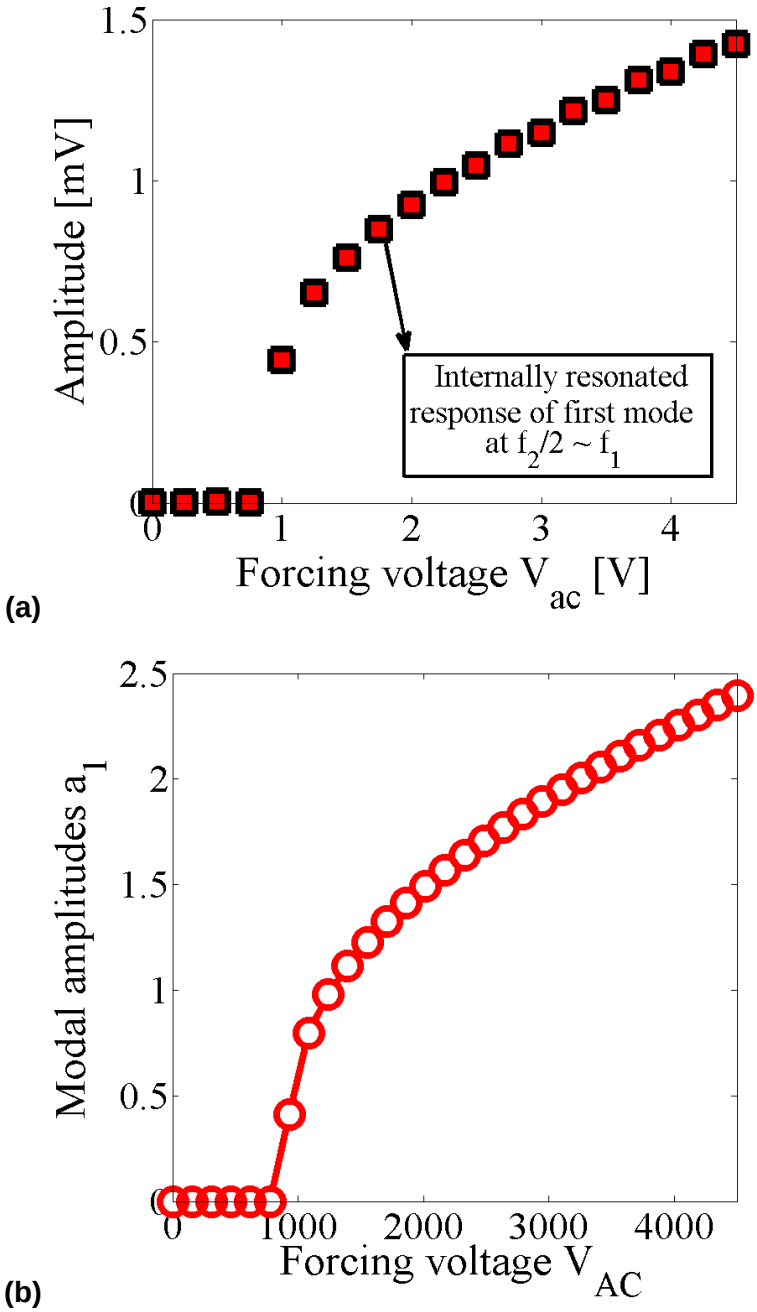

Figure 5.5. The pendulum-mode response in the H-shaped microresonator versus the AC voltage amplitudes.(a) experimentally measured when $\Omega_r=2f_1\approx1.120448$ MHz and (b) simulated when $\sigma_1=-\sigma_2$ or $\Omega_1=2\omega_1$.

To demonstrate the 2:1 Internal resonance in the system, we also actuate the second mode of interest (spring mode) at a constant drive voltage when V_{DC}=100 V and G_{amp}=10 kΩ. The drive frequency of the electrostatic voltage is then varied forward and backward around the spring mode frequency in steps while monitoring the frequency

response of the first desired mode (pendulum mode). Figure 5.7 shows the experimental and simulated frequency response of the first mode for three different drive voltages. The simulated amplitudes a_1 are achieved using Equation (5.34).The observed coupling and associated nonlinear frequency response curves are the characteristics of the nonlinear systems with 2:1 internal resonance. Despite the actuation of the system at the excitation frequency in the vicinity of the spring-mode resonant frequency, the pendulum mode responds at half the excitation frequency. As the electrostatic voltage is increased, the microresonator starts to experience more nonlinear mode coupling, where the vibrational amplitude splits and two peaks of the vibrational deflection emerge in the vicinity of the pendulum-mode resonant frequency. The splitting of the resonance curve is a consequence of the nonlinear mode coupling due to the 2:1 internal resonance. Increasing more the electrostatic voltage V_{ac} will result in more separation between the peaks. A remark worth mentioning is the broadening of the resonance band due to the presence of two peaks in the frequency response curve.

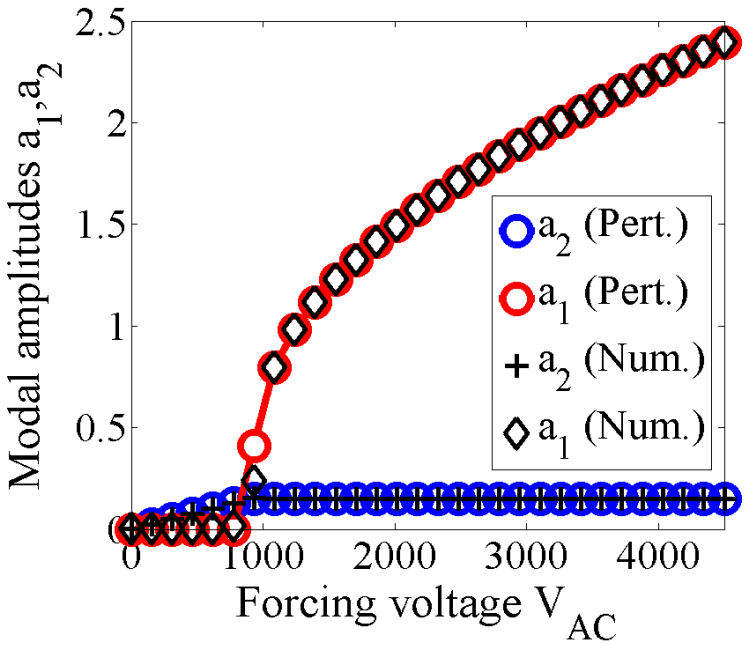

Figure 5.6. **The simulation of the modal amplitudes a_1 and a_2 in the H-shaped microresonator versus the voltage V_{AC} when $\sigma_1=-\sigma_2$ or $\Omega_1=2\omega_1$. The plots are a typical representation of saturation phenomenon due to 2:1 internal resonance.**

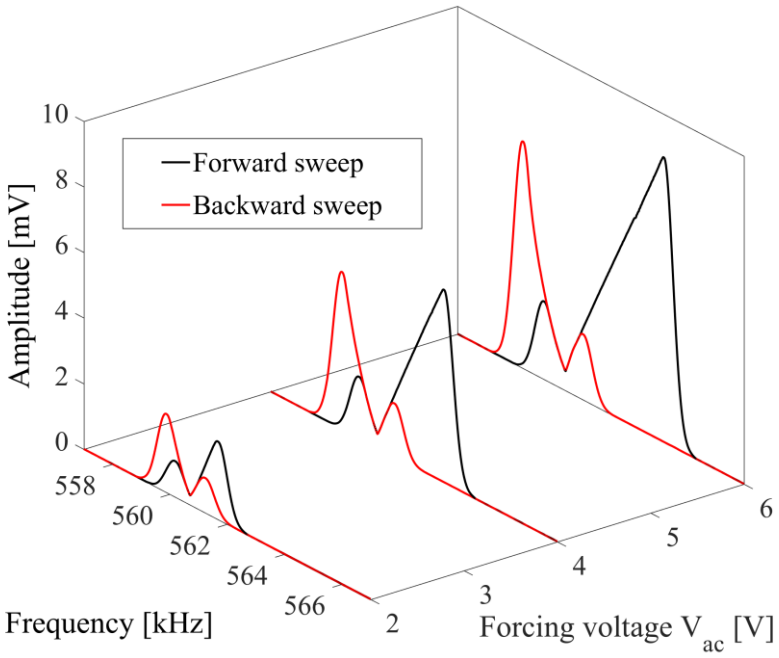

(a)

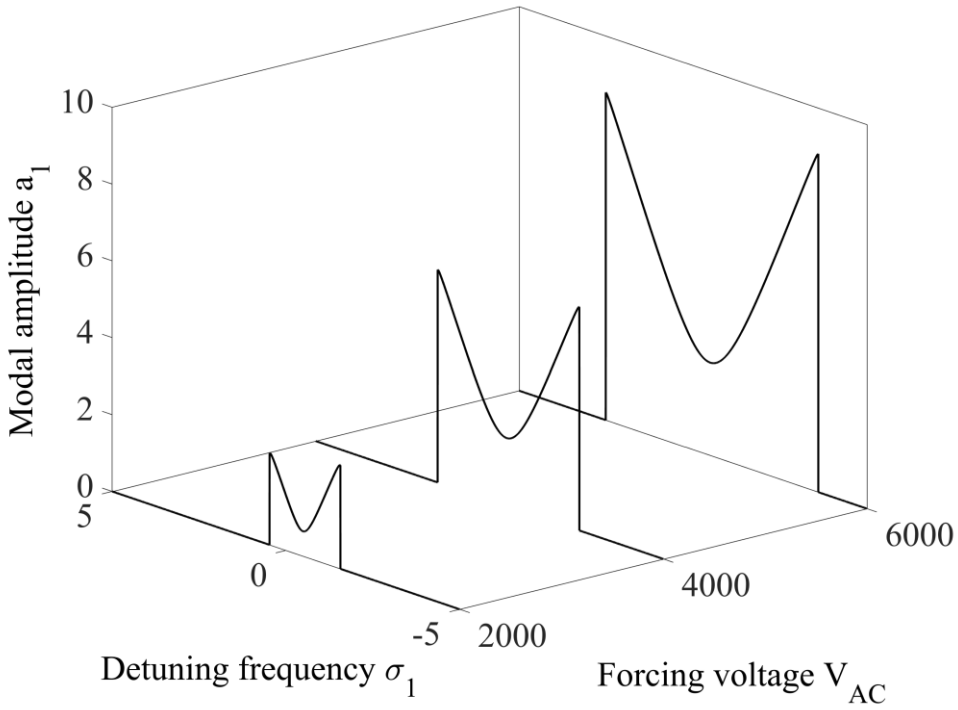

(b)

Figure 5.7. The measured nonlinear frequency transmission responses for the H-shaped microresonator. (a) experiment and (b) simulation of the amplitude a_1 versus the detuning forcing parameter σ_1.

5.4. Summary

In this chapter, we derived a 4-DOF system of two spring-pendulum mechanisms for an H-shaped tuning fork microresonator near the external and internal resonance conditions. The approximate solutions achieved from two-variable expansion perturbation technique were shown to have the saturation phenomenon and the half-order subharmonic resonance for sufficiently large forcing voltages. By examining the experimental and numerical simulation results, we found that the approximate system qualitatively reflects the nonlinear characteristics of the microresonator in case of the 2:1 internal resonance.

Chapter 6.

Rate table characterization of the microresonator

This chapter presents the experimental setup and results on testing the sensitivity of the H-shaped microresonator to rate. The description of the setup and testing approach is provided in detail. Measuring the sensitivity of the device to the input rate required specific adjustments and apparatus. The experimental findings revealed a linear correlation between the magnitude of the input angular rate and the device output over a particular range of the input rates.

6.1. Tuning fork microresonator for angular rate sensing

In the previous two chapters, MEMS tuning fork designs capable of exhibiting the nonlinear mode coupling were introduced and developed. The state of 2:1 internal resonance could be established in both microresonators, i.e., the frame- and H-shaped designs, experimentally and analytically. However, the frequency ratios were different, although close to 2:1. The results indicated that the internal resonance occurs in both devices, in which frequency ratios have some difference, though limited, from 2:1. Moreover, as shown in the frame-shaped tuning fork microresonator, the nonlinear vibrations could occur separately in two intervals of the excitation frequency where the frequency ratio is more detuned from 2:1 compared to the H-shaped microdevice. It happened even though this microdevice was designed to have the ideal-2:1 frequency ratio between the two modes of interest. In contrast to the frame-shaped design, the H-shaped microresonator with the closer frequency ratio to 2:1 demonstrated the famous *M*-shaped frequency response curves in the internally resonant systems. The H-shaped microresonator is selected for characterization on the rate table, since it can provide continuous and broader region of operation for angular rate sensing, without distance between the nonlinear resonance peaks.

The experimentally-measured resonance peaks of the H-shaped microresonator is illustrated in Figure 6.1. As mentioned earlier in Chapter 5, this plot was captured by forward- and backward frequency sweeps around the linear natural frequency of the spring mode with f_2=1.12235 MHz. For performance evaluation as a rate sensor, the operational

region of the microresonator is specified as the overlap between the forward- and backward sweeps. This common area is where the microresonator can be directly driven and the energy will be exchanged between the modes. It is noteworthy that the microresonator cannot be resonated by applying the excitation frequencies twice the frequency values outside this range.

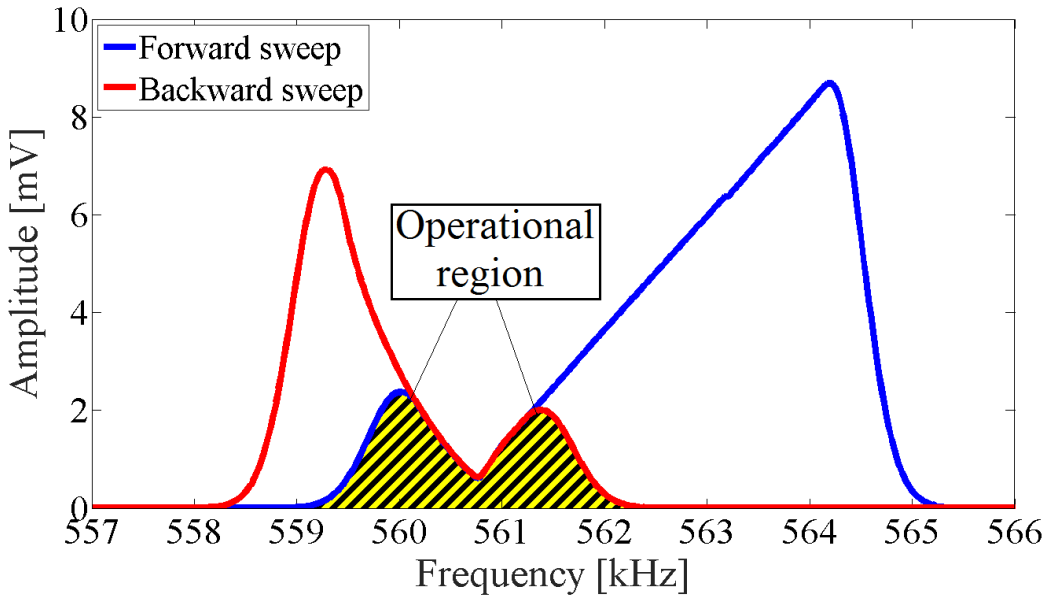

Figure 6.1. Operational frequency region for the H-shaped microresonator when V_{ac}=6V and V_{DC}=100V.

6.2. Required test arrangements

This section highlights description of the test-bed for the rate-table characterization of the microresonator. System level tests are carried out to get information about the performance of the device when undergoes the input rotation rates. The system level test is considered as scale factor (SF) test. Scale factor or sensitivity is the relationship between the output signal of the microresonator and the angular rate being measured. It is specified as the amount of change in the output voltage per unit change of rotation rate and is expressed in V deg^{-1} sec^{-1}. The vacuum-encapsulated device is affixed to a printed circuit board (PCB) to perform the SF test. Then, the PCB is mounted in a test setup, illustrated in Figure 6.2 and Figure 6.3. The block diagram in Figure 6.2 shows the practical implementation of the microresonator and the designed electronics for signal processing and measurement. Figure 6.3 shows a photograph of the actual setup. The rate

performance of the H-shaped microresonator is experimentally evaluated using a computer controlled rate table (*Ideal Aerosmith, Model: 1621-200A-TL*) with a rate controller (*AERO 812 Table Controller*). The rate table generates an angular rotation rate at various amplitudes up to approximately 2000 deg sec^{-1}. The microresonator on the PCB is placed inside the chamber of the rate table. Signal from a lock-in amplifier (*Model: HF2LI-Zurich Instruments*) is used to actuate the microresonator and demodulate the detected rate table signal. The simultaneous actuation and measurement scheme is performed through Zi-Control software installed on the computer.

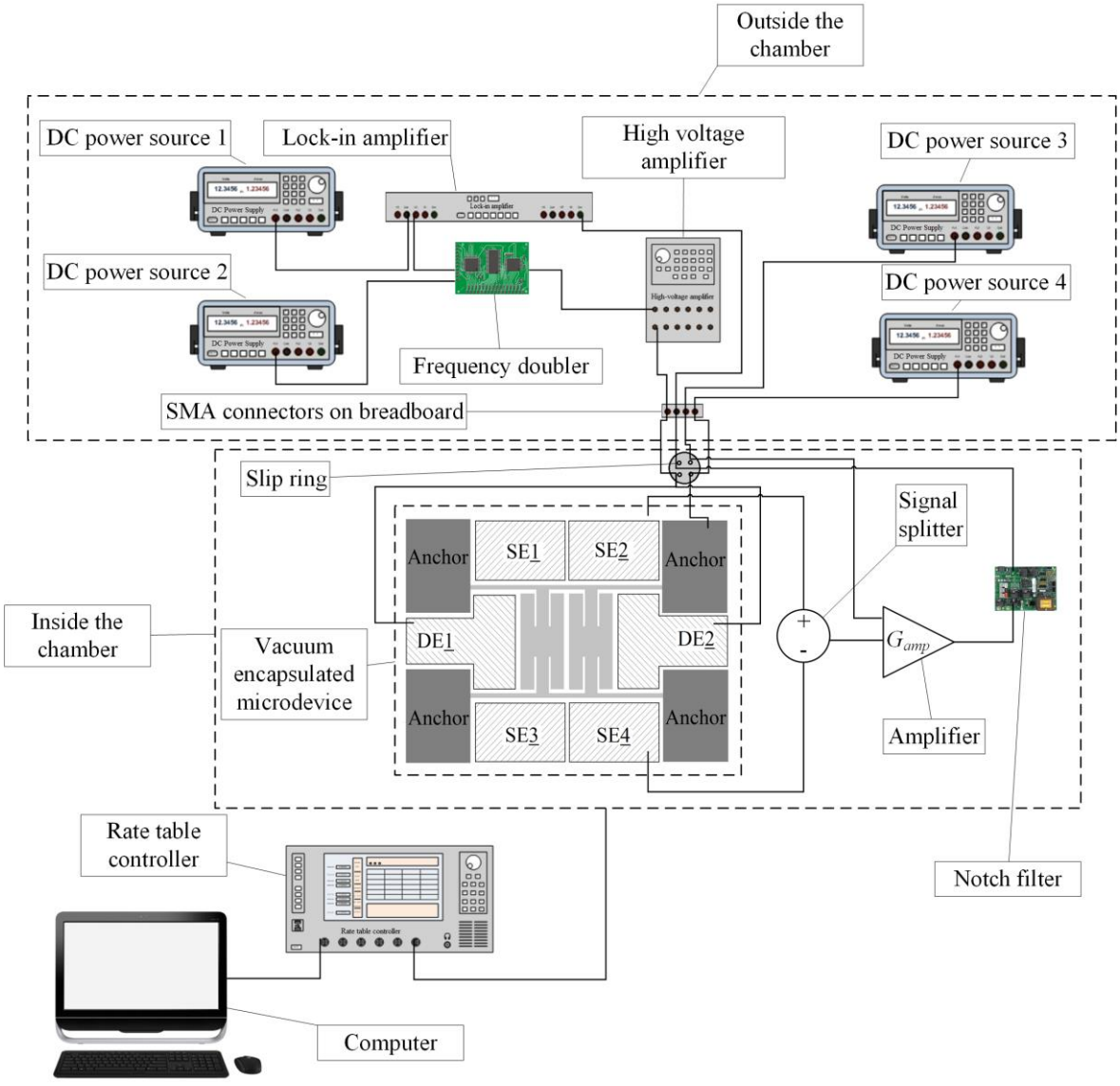

Figure 6.2. Block diagram of actuation and detection scheme used for the rate performance characterization.

Before the sensitivity test, it is crucial to confirm the nonlinear modal interaction between the anti-phase modes of the structure. To meet this requirement, we need to perform the following procedures. The microresonator is driven into the anti-phase resonant oscillations using a combination of an 80V DC bias voltage applied to the anchor through the DC power source 4 (*KEYSIGHT, Model: B2901A*) and an 800 mVpp (peak-to-peak voltage) AC driving voltage applied to DE 1 and DE 2 through the output port of the LIA. A reference signal at 561.236 kHz is provided to the LIA though the ZI-Control software. The LIA tracks the signal variation at this frequency during the testing. The frequency doubler, powered by the DC source 2 (*TENMA, Model: 72-6905*) of 5V, multiplies the frequency of the AC voltage by two and generates an actuation signal with a frequency in the neighborhood of the spring mode≈1.122468 MHz. It also produces an unwanted frequency component at 561.236 after frequency doubling. The DC source 1 (*KEYSIGHT, Model: B2901A*) with 3mV bias voltage is employed to eliminate this unwelcome frequency component. After this stage, the AC voltage has to be amplified to reach to the intended threshold to trigger the nonlinear mode coupling. The high-voltage amplifier (*TEGAM, Model: 2350*) with the gain of 20 facilitates this voltage increase. The connection between the parts inside and outside of the chamber is made possible through the slip ring on the rate table and the standard male (SMA) connectors on the breadboard.

Up to this point, the microresonator is excited to reach the necessary drive oscillations. The motions of the structure and the induced capacitance changes detected by SE 2 and SE 4 are subtracted from each other by a signal splitter (*Mini-Circuits SPLITTER, Model: ZFSCJ-2-2-S*). This differential sensing scheme is utilized to detect the resulting motion in the pendulum mode. To reduce the influence of the electrical interference on the signal, a notch filter with the attenuated frequency at 1.124 MHz is constructed. This removal of the interfering signal can result in an adjustment of the higher gain of the amplifier since the high-gain interference signal can overload the amplifier output signal. The output current of the microresonator is converted into a voltage by a transimpedance amplifier (*FEMTO, Model: DHPCA-100*), with the adjusted gain of 10^8 and powered with 15V by the DC power source 3 (*Agilent, Model: E3631A).* The boosted signal is then fed back to the LIA through the slip ring and the SMA connectors on the breadboard. The frequency response of the microdevice shown on the oscilloscope module in Zi-Control software is exhibited in Figure 6.4. As it can be noticed, the structure responds at half the excitation frequency or the reference frequency adjusted earlier on

the LIA. This observation confirms the activation of the nonlinear mode coupling due to the 2:1 internal resonance.

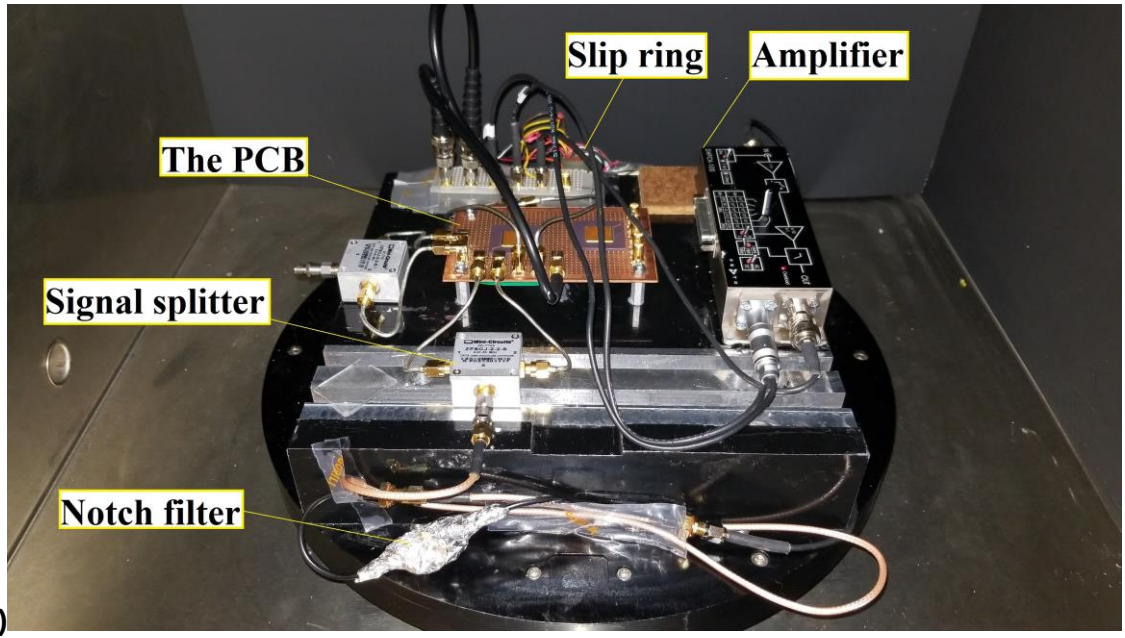

(a)

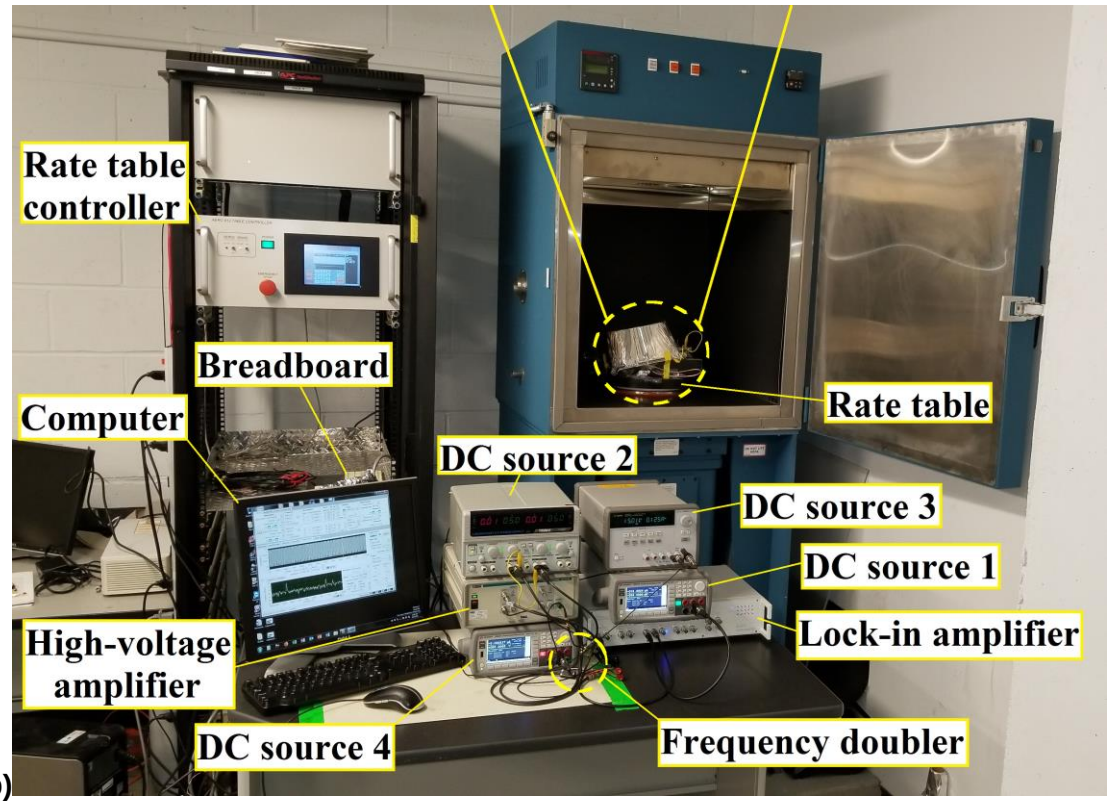

(b)

Figure 6.3. The photographs of (a) the PCB mounted inside the chamber of the rate table, and (b) the complete setup showing the actuation and measurement equipment used during the tests.

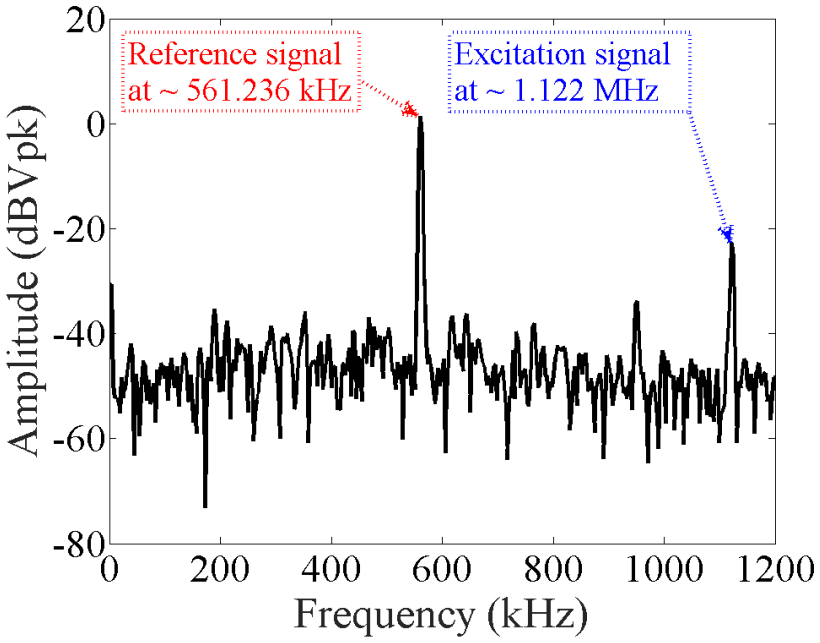

Figure 6.4. The Experimental frequency transmission plot of the H-shaped microdevice before the rotation rate application.

6.3. Test results

In the scale factor test, the rate signal in the range of ±360 deg sec^{-1} with 10 deg sec^{-1} steps is applied to the device. During the scale factor tests, the applied rate first increases from 0 deg sec^{-1} to the desired rate with the constant angular acceleration of 40 deg sec^{-2}, stays at the intended amplitude rate for roughly 30 secs, and then decreases from the desired speed to 0 with the same angular acceleration of negative sign. At the same time, the output response of the microresonator is monitored and recorded via the spectroscope module in Zi-Control software. The applied trapezoidal rate profile provides the opportunity to observe the correlation between the input rate and the output response of the microresonator. The linearity, full-scale range, and response of the microresonator to the input rotation rate are extracted from the data obtained through the scale factor test. To calculate the full-scale range and scale factor value, we perform a dynamic rate experiment using a high precision rate table. Figure 6.5 shows the calibration curve obtained by controlling the rate table to constant angular rate and observing the corresponding output voltage of the microresonator. The x-axis in the figure represents the reference signal read from the rate table output shown on the rate table controller, and the y-axis represents the difference between the output voltage in response to the rotation

rate and the bias-voltage offset before the application of the rate for the microresonator system. The asterisk mark is the measured data, and the red line is the basic fit model generated by MATLAB. By observing the data in Figure 6.5, the microresonator demonstrates that the collected data-points are fitted to a line to reveal a sensitivity of 0.011 mV deg^{-1} sec^{-1} in a measurement range (full-scale range) of approximately |220| deg s^{-1}. For higher rates, the microresonator output seems to be less sensitive to the further input rates. The remark verifies that the simulated and measured data are qualitatively consistent with each other.

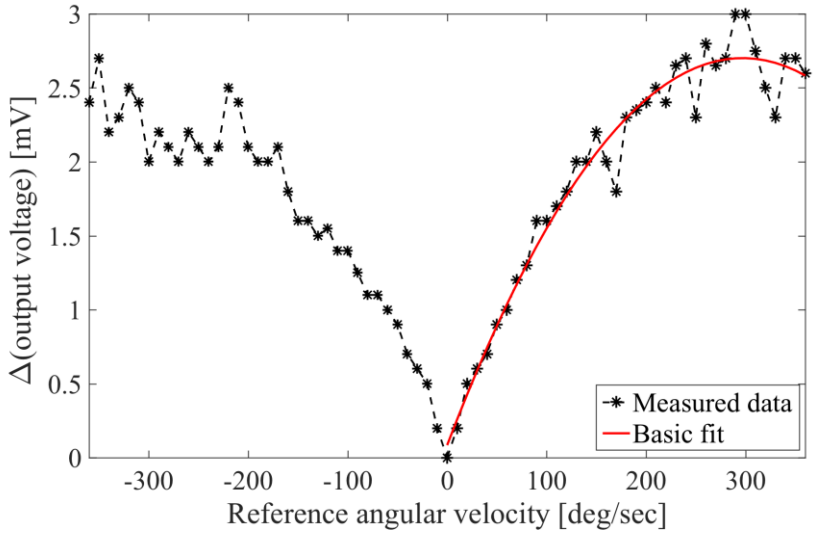

Figure 6.5. Measured full-scale rate range of the microresonator in a measurement range of ±360 deg sec^{-1} with 10 deg sec^{-1} steps.

As seen from the software simulations and experimental results, the microresonator responds to the absolute value of rate and does not recognize changes in the direction of rotation. This issue can be resolved by placing an accelerometer next to the PCB on the rate table. Accordingly, we put Samsung Galaxy S8 next to the PCB on the rate table and utilize the data acquired from the accelerometer embedded inside the phone. Figure 6.6(a) shows the measured DC output of the microresonator in response to constant angular rate inputs from the zero rate up to +200 deg sec^{-1} and then back to the zero rate and Figure 6.6(b) exhibits the accelometer's output signal sitting beside the PCB. In a similar fashion, Figure 6.7(a) illustrates the measured DC output of the microresonator in response to constant angular rate inputs from the zero rate up to -200 deg sec^{-1} and then back to the zero rate and Figure 6.7(b) demonstrates the output of the accompanying accelometer.

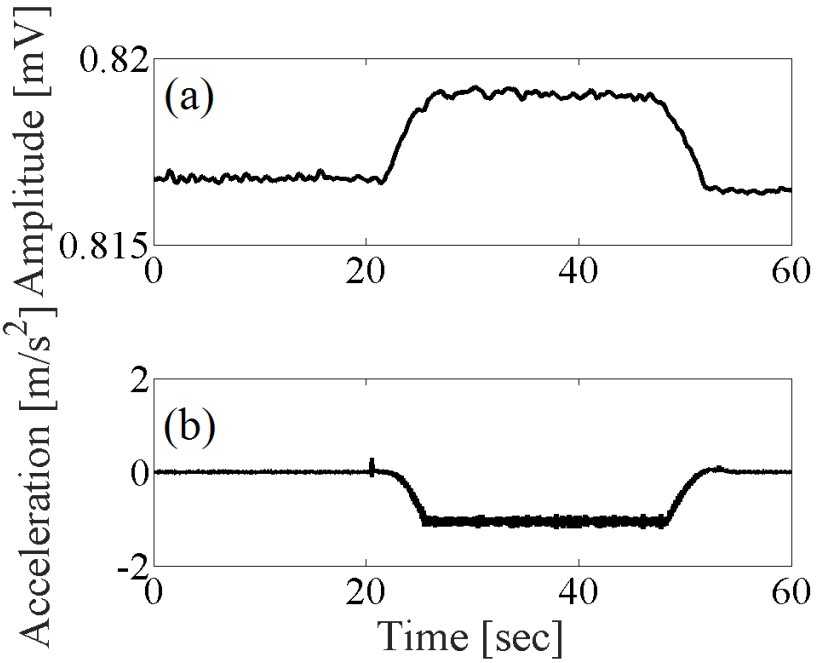

Figure 6.6. **(a) Measured DC output of the microresonator in response to constant angular input from the zero rate up to +200 deg sec^{-1} and then back to the zero rate. (b) The output of the accelerometer while testing (clockwise rotation of the rate table).**

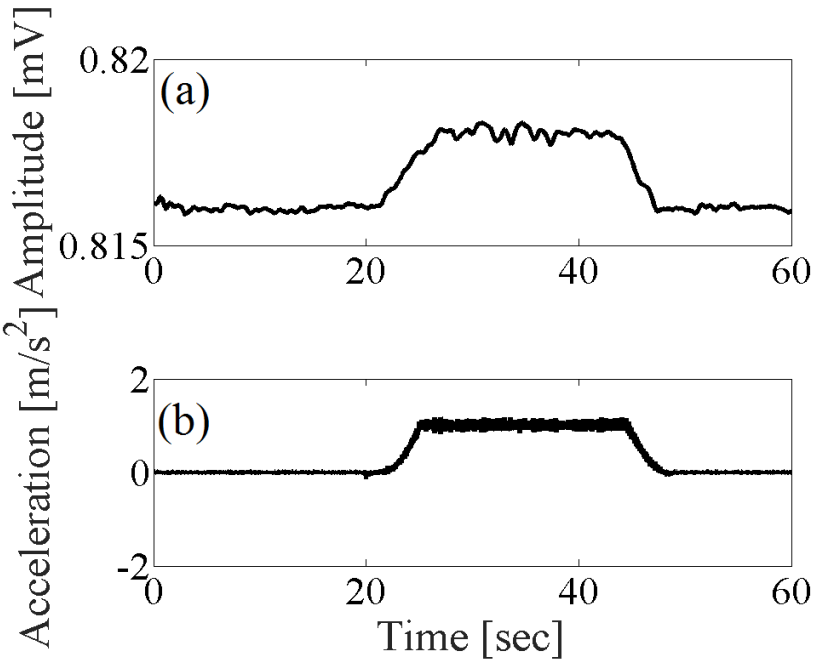

Figure 6.7. **(a) Measured DC output of the microresonator in response to constant angular input from the zero speed up to -200 deg sec^{-1} and then back to the zero rate. (b) The output of the accelerometer while testing (counterclockwise rotation of the rate table).**

According to the rate table datasheet and experimental observations, the positive angular rate values cause the clockwise rotation of the rate table, and the negative values result in the counterclockwise motion of the table. The DC bias voltages before the application of the input rate (approximately up to the first 20 seconds), shown in Figure 6.6(a) and Figure 6.7(a), are associated with the output voltage produced by the microresonator in the absence of the angular rate. As the microresonator experiences the input angular rate applied by the rate table, it responds to the command and follows the rate profile. The results also reveal that the direction of rotation can be realized by the accelometer's output. This can be understood by the sign change in the output signals of the accelerometer shown in Figure 6.6(b) and Figure 6.7(b).

6.4. Summary

The sensitivity of the H-shaped microresonator to the angular input rate was experimentally investigated. The detailed description of the test-bed to capture the microresonator output was explained thoroughly. It was shown that the output response of the microresonator linearly changed with an increase in the angular input rate in the range of 0 to 220 deg sec^{-1}. The test defined the full dynamic range of the microdevice for the angular rate measurement. The accelerometer inside the cell phone was utilized and placed beside the PCB while rotating the microresonator, to recognize the direction of the rate table rotation. This strategy helped us to specify both the direction and quantity of the rotation rate.

Chapter 7.

Conclusions and future work

7.1. Conclusions and contributions

In this dissertation, for the first time, the utilization of nonlinear 2:1 internal resonance in microresonators for angular rate sensing was investigated. I studied nonlinear features of the proposed microresonators incorporating the 2:1 internal resonance through experiments as well as the analytical studies. The nonlinear mode coupling induced by the internal resonance was introduced as an alternative solution to eliminate the mode-matched condition in MEMS Coriolis vibratory gyroscopes. The author believed that the 2:1 internal resonance has a few advantages which are of interest in MEMS Coriolis vibratory gyroscopes applications as follow. The microresonator with the 2:1 internal resonance between the vibrational modes can generate broad operational frequency region with high gain signals. The mode of operation causes less sensitivity of the microdevice to the fluctuations in the driving frequency. Another remarkable benefit is to decrease the effect of the off-axis cross-coupling between modes of operation. For conventional MEMS gyroscopes, the drive and sense modes are required to be in a close match for improving sensor sensitivity. However, a small fabrication defect may cause undesirable cross-coupling arising from damping and stiffness forces, which prevents high precision of the gyroscopes arising from quadrature error. In the proposed principle of operation, the drive (spring) and sense (pendulum) modes are away from each other, and this may reduce the unwanted cross-coupling problem.

I proposed two MEMS tuning fork designs, which resemble nonlinear dynamics of a spring-pendulum system with the forced and 2:1 internal resonances. The tuning fork designs were chosen due to their excellent dynamic characteristics regarding common-mode rejection and differential mode of operation. Electrostatic/capacitive transduction was employed for actuation and detection ends because of easy fabrication and ease of implementation. The frame- and H-shaped tuning fork MEMS structures were designed using Architect™ CoventorWare© software. This analysis tool has proven to be extremely reliable, particularly for the analysis of the nonlinear dynamics of systems operating on the 2:1 internal resonance. The author could successfully predict the qualitative behavior of

the device before the experiments, which was of great significance during the device design and also in testing them. The reduced-order modeling software (Architect™ CoventorWare©) facilitated the modal analysis and transient behavior of the microresonators in two different modes as a resonator and an angular rate sensor. Long hours of simulations on the microdevices demonstrated the effectiveness of the 2:1 internal resonance application in angular rate measurements. The microresonators illustrated sensitivity to the angular rotation velocities while the nonlinear mode coupling was probed.

The simulation software proved to be truly valuable in the nonlinear analysis, although the simulations were incredibly lengthy. Consequently, the nonlinear behavior of the tuning fork resonators was then investigated through the lumped mass-spring-damper modeling and the two-variable expansion perturbation technique. Detailed nonlinear models of the microstructures according to the spring-pendulum assumption were presented and explained in detail. These include the models of electrostatic (actuation and detection) nonlinearities. Later the simulation results achieved by the mathematical models established a qualitative agreement with the experiments, confirming the validity of the closed-form perturbation solutions.

The sketched layout consisting of the designed microresonators (the frame- and H-shaped designs) were sent to the external foundry, Teledyne DALSA Inc., and fabricated via MIDIS fabrication technology. The extensive experiments were accomplished to probe the nonlinear dynamics of the microresonators. The testing on the frame-shaped microresonator showed that there was 1.9932 frequency ratio between the in-phase (pendulum mode) and the anti-phase (spring mode) motions of the masses along the Y- and X-axes, respectively. The test result differed from the expected modes of vibration, which were both out-of-phase oscillations. The non-ideal, although close to 2:1, frequency ratio in the frame-shaped tuning fork led to the occurrence of the nonlinear resonant peaks in the separate region of the excitation frequency. The analytical studies also confirmed the experimental responses. The measured frequency ratio of 2.003 between the anti-phase modes (pendulum and spring modes) in the H-shaped microresonator were more desirable and closer to 2:1. The experimental results confirmed the nonlinear mode coupling between the modes and generation of the *M*-shaped nonlinear frequency response curves. The results proved the initial hypothesis obtained

through the software simulations. The validity of the perturbation solutions was also approved via qualitative comparison with the experimental measurements.

The existence of the preplanned nonlinear characteristics of the microresonators, i.e., saturation phenomenon and nonlinear frequency response curves created by half subharmonic responses, were confirmed analytically and experimentally. Afterward, it was the time to investigate the dynamical behavior of the microresonator when subjected the angular input rate. The H-shaped microstructure was chosen as it offered better nonlinear dynamical behavior due to closer frequency ratio to 2:1 compared to the frame-shaped microresonator. The unique testing apparatus was designed and implemented to carry out the rate table characterization of the microresonator. With careful design and selection of the test-bed components, the experimental results showed the sensitivity of the microresonator to the angular input rates in the range of 0 to 220 deg sec^{-1}. An accelerometer was used to determine the direction of rotation. To sum up, the author believes the utilization of the 2:1 internal resonance as the actuation mechanism can lead to alternative avenues and pave the way for the development of the nonlinear MEMS Coriolis vibratory gyroscopes without the need to mode-tuning condition.

7.2. Future work

This work founded the basis of the application of the 2:1 internal resonance in next generation of nonlinear MEMS Coriolis vibratory gyroscopes. Additional investigations can be conducted to improve further the performance of the microresonators exhibiting the nonlinear modal interaction. Following provides a list of viable future enhancements.

1) The performance figures of merit of the MEMS gyroscopes, i.e., resolution (angle random walk), dynamic drift bias, bandwidth, etc., have to be investigated and enhanced for the future microresonator designs.

2) Two approaches are feasible for improving the sensitivity and enhancing the resolution of the microdevices. The first scheme is to design and fabricate structures with larger inertial proof masses. The second approach is using system-level solutions for increasing the sensitivity, for instance by inducing a significant displacement in the spring mode or/and increasing the structural quality factors. These proposed strategies have to

be accomplished through analytical/software simulations before fabrication and experiments.

3) Non-deterministic noise levels, e.g., drift bias and electronic noise have to be minimized. To this end, electronic actuation and readout circuits are needed to be carefully designed with low noise floors and power consumption. Future experiments are recommended to be accomplished by placement of the PCB inside a small vacuum chamber affixed to the rate table. This arrangement can be significantly beneficial to reduce the effect of electrical interference and noise floors.

4) The improved characteristics associated with typical MEMS gyroscopes tuned to 2:1 internal resonance include wide bandwidth with a flat frequency response curve of the sense vibrational mode. The flat frequency region is defined as the operational frequency region of the gyroscope with a 2:1 frequency ratio. Under these conditions, the coupling terms such as Coriolis (or nonlinear quadratic terms) will be responsible for facilitating the energy-transfer between the drive and sense modes, and because of the wide (and flat top) sense-mode frequency response curve, the gyroscope becomes less sensitive to variation in the drive frequency. Accordingly, investigation on the impact of nonlinear coupling terms to widen the operational frequency region, and enhance the flat-top area of operation is of great importance. The influence of various nonlinear coupling terms to improve the performance of the internally resonant gyroscopes (i.e., bandwidth and smooth operation region) are needed to be well studied. As the proof of concept, this idea has been implemented on a macro-scale T-beam structure actuated by an electromagnetic shaker, shown in Figure 7.1. The effect of the cubic nonlinearity feedbacks on the nonlinear frequency response of the pendulum mode with 1.89 frequency ratio between the vibrational modes (r_1: spring mode and θ_2: pendulum mode) are presented in Figure 7.2. In these figures, term 1 indicates $K_a r_1 \dot{\theta}_2^2$, and term 2 implies $K_b r_1^i \dot{\theta}_2^2$. As it can be observed, the manipulation of the nonlinear feedback can generate flat-top resonant curves. Although this strategy is pretty useful in the macro-scale systems, its implementation in microstructures can be extremely challenging.

5) Other microresonator designs capable of exhibiting 2:1 internal resonance are designed and characterized to study their sensitivity to the angular input rates. As such,

two structural designs simulated in Architect™ are introduced in Figure 7.3 and Figure 7.4.

6) The characterization of bulk acoustic wave (BAW) microresonators operating on the nonlinear 2:1 internal resonance is of great interest. Since they are capable of delivering superior dynamic properties such as high resistance to shock and vibration due to their high natural frequencies, high-quality factor under atmospheric or near atmospheric pressure and without vacuum packaging, high resistance to stiction during both fabrication and operation, etc.

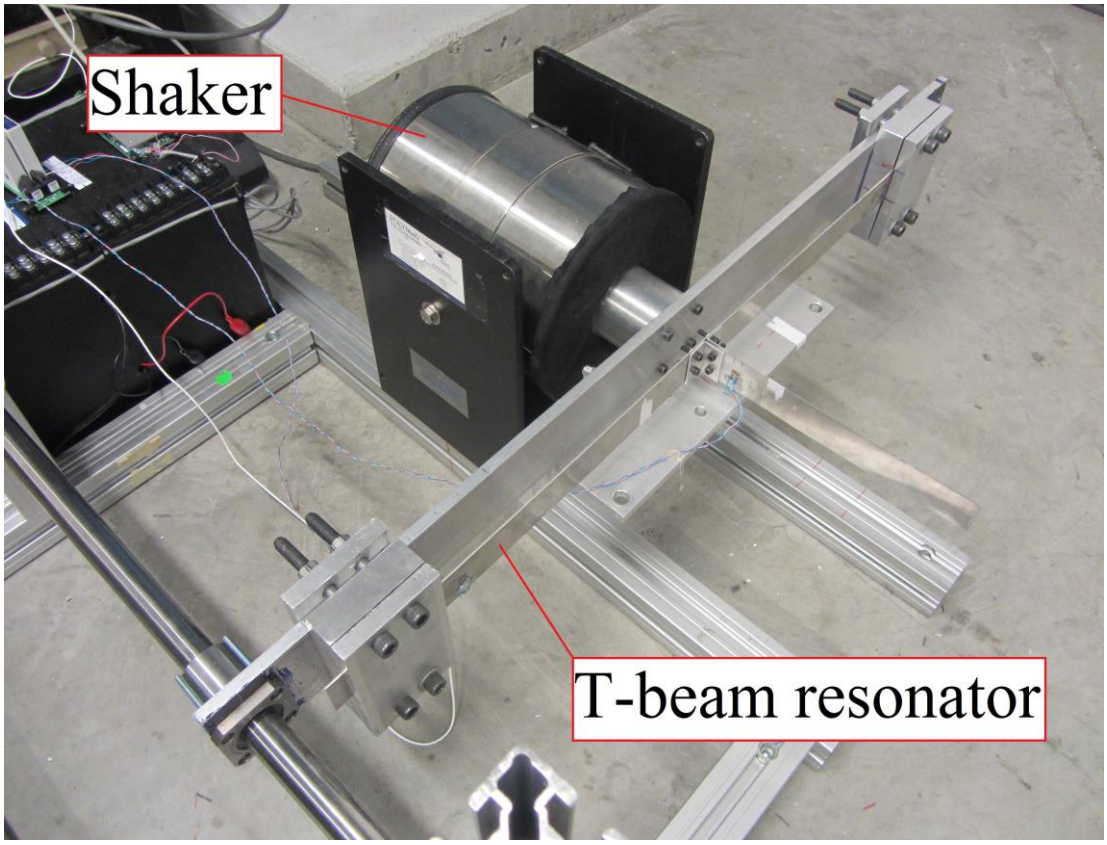

Figure 7.1. Photograph of the macro-scale T-beam as a resonator excited by the electromagnetic shaker.

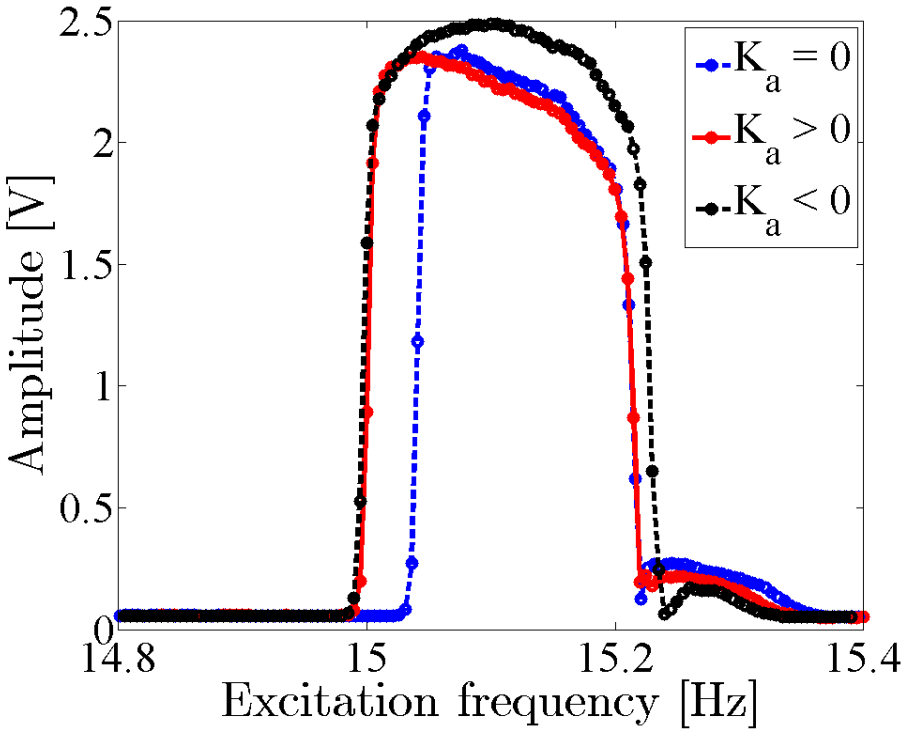

(a)

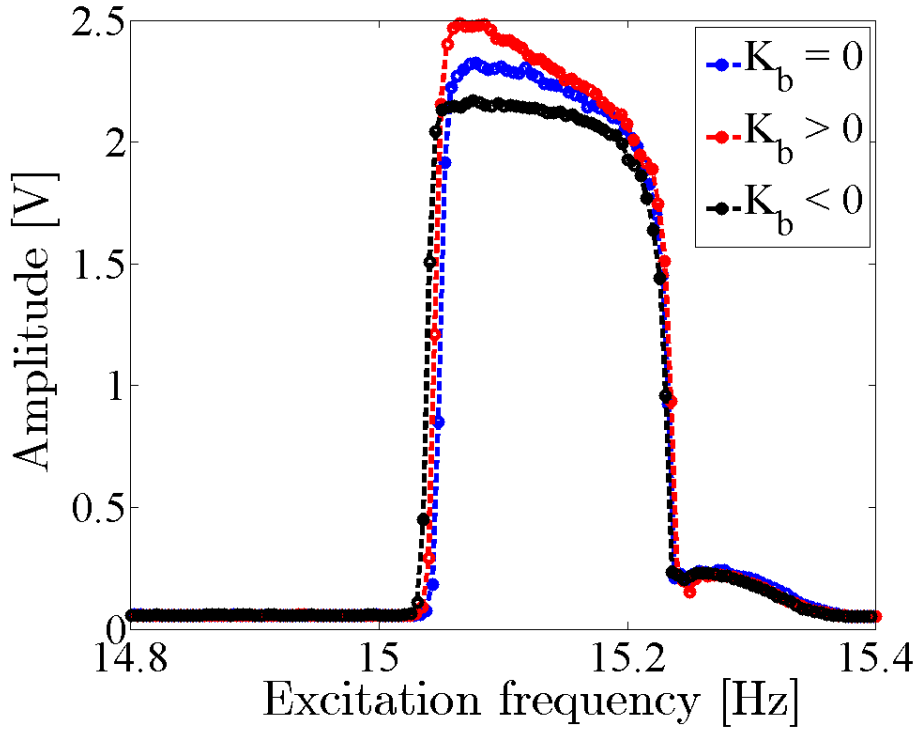

(b)

Figure 7.2. Effect of cubic nonlinear feedback (a) term 1 and (b) term 2 on the nonlinear resonant peaks of the macro-scale T-beam structure.

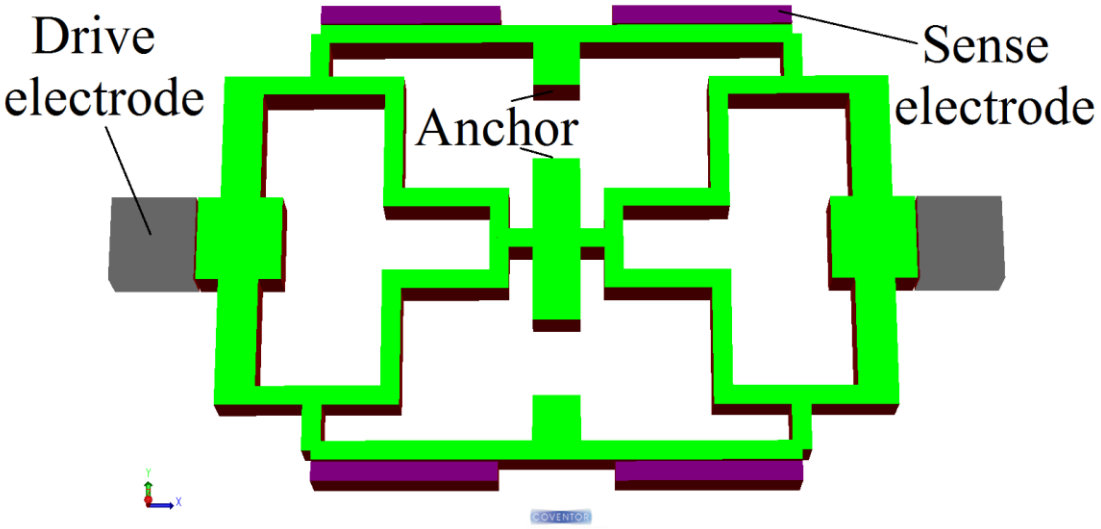

(a)

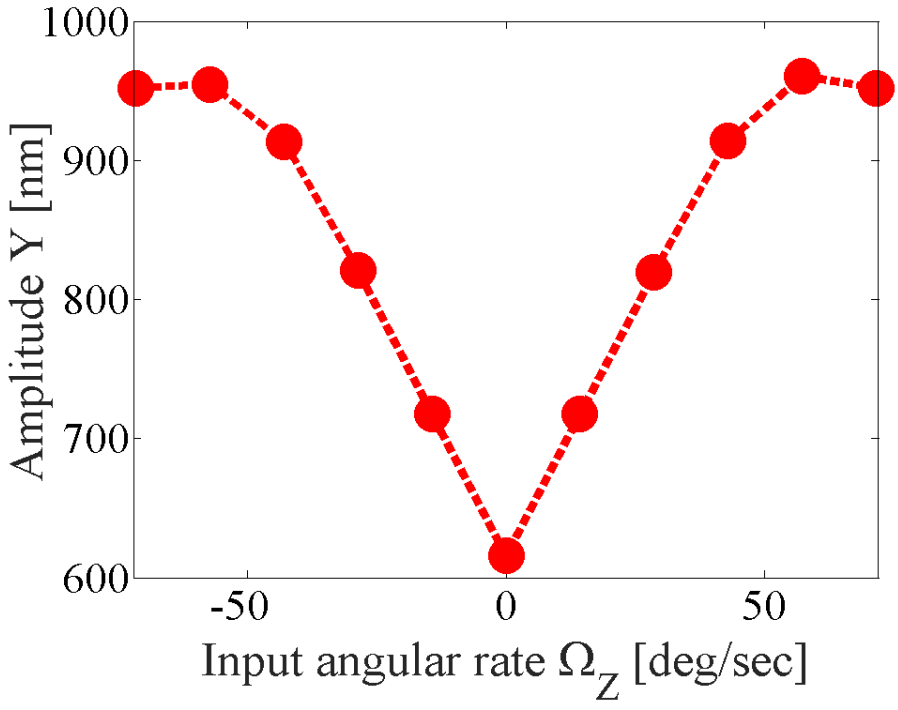

(b)

Figure 7.3. **(a) 3D view of the proposed TF microresonator simulated in Architect™ Scence3D. (b) Full-scale sensitivity range of the microresonator to the input rate.**

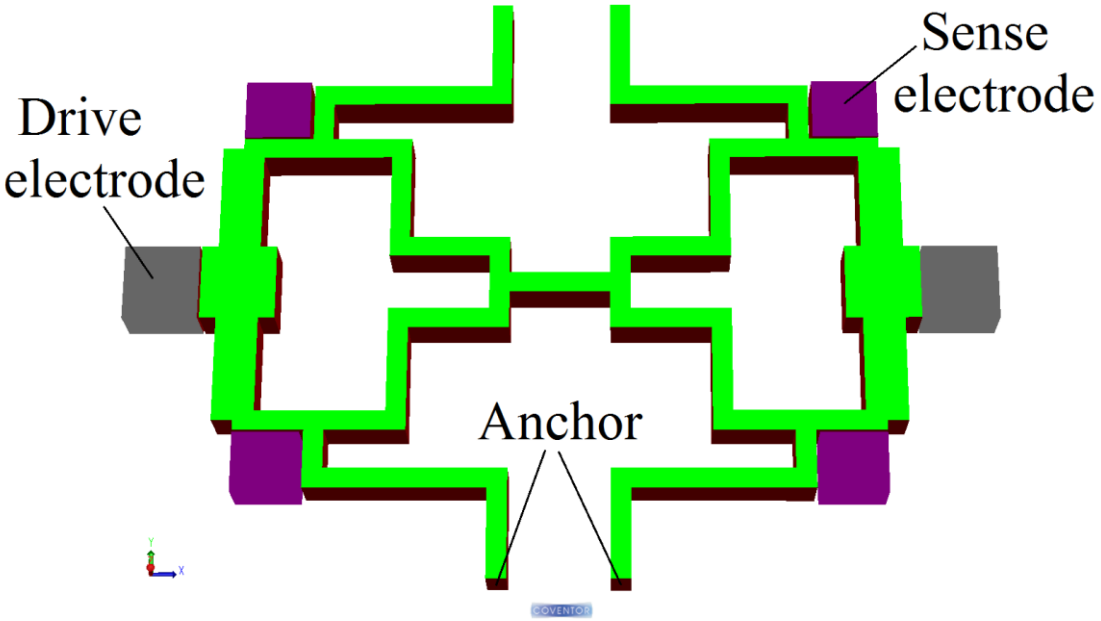

(a)

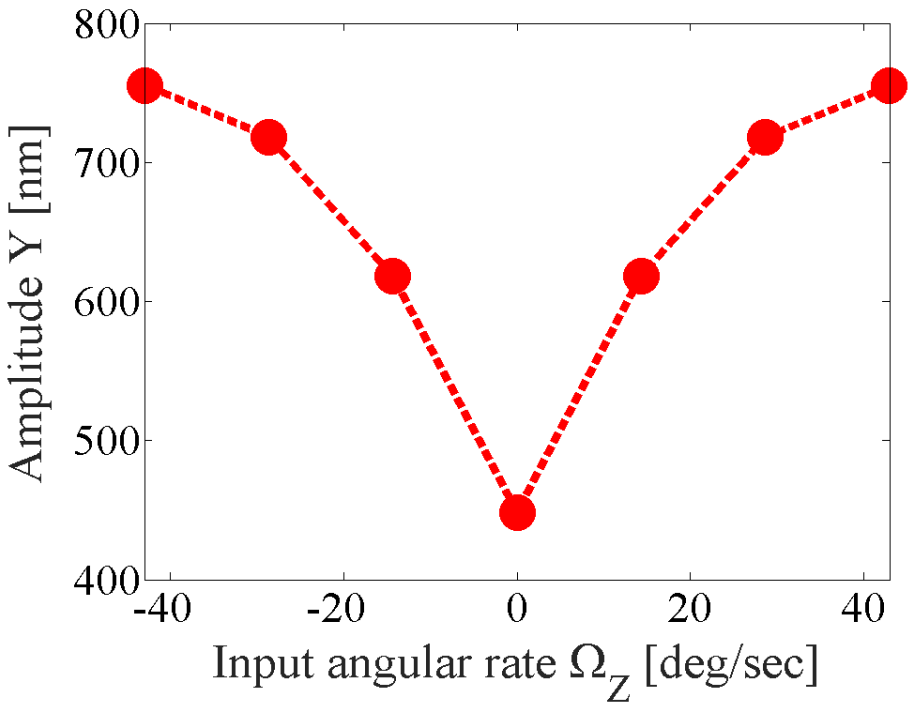

(b)

Figure 7.4. **(a) 3D view of the proposed TF microresonator simulated in Architect™ Scence3D. (b) Full-scale sensitivity range of the microresonator to the input rate.**

References

[1] R. Abdolvand, B. Bahreyni, J. E.-Y. Lee, and F. Nabki, “Micromachined Resonators: A Review,” *Micromachines*, vol. 7, no. 9, p. 160, Sep. 2016.

[2] C. Lan, W. Qin, and W. Deng, “Energy Harvesting by Dynamic Unstability and Internal Resonance for Piezoelectric Beam,” *Appl. Phys. Lett.*, vol. 107, no. 9, p. 093902, Aug. 2015.

[3] D. Antonio, D. H. Zanette, and D. López, “Frequency Stabilization in Nonlinear Micromechanical Oscillators,” *Nat. Commun.*, vol. 3, p. 806, May 2012.

[4] C. Samanta, P. R. Yasasvi Gangavarapu, and A. K. Naik, “Nonlinear Mode Coupling and Internal Resonances in MoS2 Nanoelectromechanical System,” *Appl. Phys. Lett.*, vol. 107, no. 17, p. 173110, Oct. 2015.

[5] A. Castellanos-Gomez, H. B. Meerwaldt, W. J. Venstra, H. S. J. van der Zant, and G. A. Steele, “Strong and Tunable Mode Coupling in Carbon Nanotube Resonators,” *Phys. Rev. B*, vol. 86, no. 4, p. 041402, Jul. 2012.

[6] W. J. Venstra, R. van Leeuwen, and H. S. J. van der Zant, “Strongly Coupled Modes in a Weakly Driven Micromechanical Resonator,” *Appl. Phys. Lett.*, vol. 101, no. 24, p. 243111, Dec. 2012.

[7] A. H. Ramini, A. Z. Hajjaj, and M. I. Younis, “Tunable Resonators for Nonlinear Modal Interactions,” *Sci. Rep.*, vol. 6, p. 34717, Oct. 2016.

[8] C. R. Kirkendall, D. J. Howard, and J. W. Kwon, “Internal Resonance in Quartz Crystal Resonator and Mass Detection in Nonlinear Regime,” *Appl. Phys. Lett.*, vol. 103, no. 22, p. 223502, Nov. 2013.

[9] E. Sage *et al.*, “Neutral Particle Mass Spectrometry with Nanomechanical Systems,” *Nat. Commun.*, vol. 6, p. 6482, Mar. 2015.

[10] Y. T. Yang, C. Callegari, X. L. Feng, K. L. Ekinci, and M. L. Roukes, “Zeptogram-Scale Nanomechanical Mass Sensing,” *Nano Lett.*, vol. 6, no. 4, pp. 583–586, Apr. 2006.

[11] X. L. Feng, C. J. White, A. Hajimiri, and M. L. Roukes, “A Self-Sustaining Ultrahigh-Frequency Nanoelectromechanical Oscillator,” *Nat. Nanotechnol.*, vol. 3, no. 6, p. 342, Jun. 2008.

[12] A. N. Cleland and M. L. Roukes, “Noise Processes in Nanomechanical Resonators,” *J. Appl. Phys.*, vol. 92, no. 5, pp. 2758–2769, Aug. 2002.

[13] X. Wei, L. Ruihong, and L. Shuang, “Resonance and Bifurcation in a Nonlinear Duffing System with Cubic Coupled Terms,” *Nonlinear Dyn.*, vol. 46, no. 1–2, pp. 211–221, Oct. 2006.

[14] K. L. Tuer, M. F. Golnaraghi, and D. Wang, “Development of a Generalised Active Vibration Suppression Strategy for a Cantilever Beam Using Internal Resonance,” *Nonlinear Dyn.*, vol. 5, no. 2, pp. 131–151, Mar. 1994.

[15] S. A. Q. Siddiqui and M. F. Golnaraghi, “Vibration Suppression in a Flexible Gyroscopic System Using Modal Coupling Strategies,” *Mathematical Problems in Engineering*, 1996. [Online]. Available: https://www.hindawi.com/journals/mpe/1996/389684/abs/. [Accessed: 27-Feb-2018].

[16] T. Ikeda and S. Murakami, “Autoparametric Resonances in a Structure/Fluid Interaction System Carrying a Cylindrical Liquid Tank,” *J. Sound Vib.*, vol. 285, no. 3, pp. 517–546, Jul. 2005.

[17] K. L. Tuer, A. P. Duquette, and M. F. Golnaraghi, “Vibration Control of a Flexible Beam Using a Rotational Internal Resonance Controller, Part I: Theoretical Development and Analysis,” *J. Sound Vib.*, vol. 167, no. 1, pp. 41–62, Oct. 1993.

[18]A. P. Duquette, K. L. Tuer, and M. F. Golnaraghi, “Vibration Control of a Flexible Beam Using a Rotational Internal Resonance Controller, Part II: Experiment,” *J. Sound Vib.*, vol. 167, no. 1, pp. 63–75, Oct. 1993.
[19]N. Srinil and G. Rega, “Two-to-One Resonant Multi-Modal Dynamics of Horizontal/Inclined Cables. Part II: Internal Resonance Activation, Reduced-Order Models and Nonlinear Normal Modes,” *Nonlinear Dyn.*, vol. 48, no. 3, pp. 253–274, May 2007.
[20]A. Luongo and G. Piccardo, “Non-linear Galloping of Sagged Cables in 1:2 Internal Resonance,” *J. Sound Vib.*, vol. 214, no. 5, pp. 915–940, Jul. 1998.
[21]A. H. Nayfeh, D. T. Mook, and L. R. Marshall, “Nonlinear Coupling of Pitch and Roll Modes in Ship Motions,” *J. Hydronautics*, vol. 7, no. 4, pp. 145–152, 1973.
[22]Y. Ishida and T. Inoue, “Internal Resonance Phenomena of the Jeffcott Rotor With Nonlinear Spring Characteristics,” *J. Vib. Acoust.*, vol. 126, no. 4, pp. 476–484, Dec. 2004.
[23]Y. Fujino, P. Warnitchai, and B. M. Pacheco, “An Experimental and Analytical Study of Autoparametric Resonance in a 3DOF Model of Cable-Stayed-Beam,” *Nonlinear Dyn.*, vol. 4, no. 2, pp. 111–138, Apr. 1993.
[24]A. Vyas, D. Peroulis, and A. K. Bajaj, “A Microresonator Design Based on Nonlinear 1:2 Internal Resonance in Flexural Structural Modes,” *J. Microelectromechanical Syst.*, vol. 18, no. 3, pp. 744–762, Jun. 2009.
[25]R. Antonello, R. Oboe, L. Prandi, and F. Biganzoli, “Automatic Mode Matching in MEMS Vibrating Gyroscopes Using Extremum-Seeking Control,” *IEEE Trans. Ind. Electron.*, vol. 56, no. 10, pp. 3880–3891, Oct. 2009.
[26]S. Park and R. Horowitz, “Adaptive Control for Z-Axis MEMS Gyroscopes,” in *Proceedings of the 2001 American Control Conference. (Cat. No.01CH37148)*, 2001, vol. 2, pp. 1223–1228 vol.2.
[27]N. Yazdi, F. Ayazi, and K. Najafi, “Micromachined Inertial Sensors,” *Proc. IEEE*, vol. 86, no. 8, pp. 1640–1659, Aug. 1998.
[28]A. Said Emre, “MEMS Gyroscopes for Tactical-Grade Inertial Measurement Applications,” The Graduate School of Natural and Applied Sciences of Middle East Technical University, Middle East Techinical University, 2005.
[29]A. M. Shkel, “Type I and Type II Micromachined Vibratory Gyroscopes,” in *2006 IEEE/ION Position, Location, And Navigation Symposium*, 2006, pp. 586–593.
[30]P. R. Sethna, “Steady-State Undamped Vibrations of a Class of Nonlinear Discrete Systems,” *J. Appl. Mech.*, vol. 27, no. 1, pp. 187–195, Mar. 1960.
[31]S. Sridhar, A. H. Nayfeh, and D. T. Mook, “Nonlinear Resonances in a Class of Multi-Degree-of-Freedom Systems,” *J. Acoust. Soc. Am.*, vol. 58, no. 1, pp. 113–123, Jul. 1975.
[32]A. G. Haddow, A. D. S. Barr, and D. T. Mook, “Theoretical and Experimental Study of Modal Interaction in a Two-Degree-of-Freedom Structure,” *J. Sound Vib.*, vol. 97, no. 3, pp. 451–473, Dec. 1984.
[33]D. T. Mook, R. H. Plaut, and N. HaQuang, “The Influence of an Internal Resonance on Non-Linear Structural Vibrations Under Subharmonic Resonance Conditions,” *J. Sound Vib.*, vol. 102, no. 4, pp. 473–492, Oct. 1985.
[34]R. S. Haxton and A. D. S. Barr, “The Autoparametric Vibration Absorber,” *J. Eng. Ind.*, vol. 94, no. 1, pp. 119–125, Feb. 1972.
[35]A. H. Nayfeh and L. D. Zavodney, “Experimental Observation of Amplitude- and Phase-Modulated Responses of Two Internally Coupled Oscillators to a Harmonic Excitation,” *J. Appl. Mech.*, vol. 55, no. 3, pp. 706–710, Sep. 1988.

[36]A. H. Nayfeh and B. Balachandran, “Experimental Investigation of Resonantly Forced Oscillations of a Two-Degree-of-Freedom Structure,” *Int. J. Non-Linear Mech.*, vol. 25, no. 2, pp. 199–209, Jan. 1990.
[37]M. F. Golnaraghi, “Regulation of Flexible Structures via Nonlinear Coupling,” *Dyn. Control*, vol. 1, no. 4, pp. 405–428, Nov. 1991.
[38]S. S. Oueini, A. H. Nayfeh, and M. F. Golnaraghi, “A Theoretical and Experimental Implementation of a Control Method Based on Saturation,” *Nonlinear Dyn.*, vol. 13, no. 2, pp. 189–202, Jun. 1997.
[39]S. S. Oueini and M. F. Golnaraghi, “Experimental Implementation of the Internal Resonance Control Strategy,” *J. Sound Vib.*, vol. 191, no. 3, pp. 377–396, Apr. 1996.
[40]S. Oueini and A. Nayfeh, “Saturation Control of a DC Motor,” in *37th Structure, Structural Dynamics and Materials Conference*, American Institute of Aeronautics and Astronautics.
[41]M. Sayed and M. Kamel, “1:2 and 1:3 Internal Resonance Active Absorber for Non-Linear Vibrating System,” *Appl. Math. Model.*, vol. 36, no. 1, pp. 310–332, Jan. 2012.
[42]K. L. Tuer, M. F. Golnaraghi, and D. Wang, “Development of a Generalised Active Vibration Suppression Strategy for a Cantilever Beam Using Internal Resonance,” *Nonlinear Dyn.*, vol. 5, no. 2, pp. 131–151, Mar. 1994.
[43]K. L. Tuer, “Vibration Control of Flexible Structures Using Nonlinear and Linear Coupling Effects.,” University of Waterloo, 1993.
[44]A. P. Duquette, “An Experimental Study of Vibration Control of a Flexible Beam via Modal and Coordinate Coupling.,” University of Waterloo, 1991.
[45]M. F. Golnaraghi, K. Tuer, and D. Wang, “Regulation of a Lumped Parameter Cantilever Beam via Internal Resonance Using Nonlinear Coupling Enhancement,” *Dyn. Control*, vol. 4, no. 1, pp. 73–96, Jan. 1994.
[46]A. Sarrafan, B. Bahreyni, and F. Golnaraghi, “Development and Characterization of an H-Shaped Microresonator Exhibiting 2:1 Internal Resonance,” *J. Microelectromechanical Syst.*, vol. 26, no. 5, pp. 993–1001, Oct. 2017.
[47]A. Sarrafan, B. Bahreyni, and F. Golnaraghi, “Design and Characterization of Microresonators Simultaneously Exhibiting 1/2 Subharmonic and 2:1 Internal Resonances,” in *2017 19th International Conference on Solid-State Sensors, Actuators and Microsystems (TRANSDUCERS)*, 2017, pp. 102–105.
[48]A. Vyas, D. Peroulis, and A. K. Bajaj, “Dynamics of a Nonlinear Microresonator Based on Resonantly Interacting Flexural-Torsional Modes,” *Nonlinear Dyn.*, vol. 54, no. 1–2, pp. 31–52, Oct. 2008.
[49]E. Hacker and O. Gottlieb, “Internal Resonance Based Sensing in Non-Contact Atomic Force Microscopy,” *Appl. Phys. Lett.*, vol. 101, no. 5, p. 053106, Jul. 2012.
[50]S. Souayeh and N. Kacem, “Internal Resonances in Nonlinear Nanocantilever Arrays Under Electrostatic Actuation,” in *1st Euro-Mediterranean Conference on Structural Dynamics and Vibroacoustics (MEDYNA 2013)*, France, 2013, pp. 1–4.
[51]S. Gutschmidt and O. Gottlieb, “Nonlinear Internal Resonances of a Microbeam Array Near the Pull-In Point,” presented at the 6th EUROMECH Nonlinear Dynamics Conference (ENOC 2008), 2011.
[52]P. A. Hassanpour, E. Esmailzadeh, W. L. Cleghorn, and J. K. Mills, “Nonlinear Vibration of Micromachined Asymmetric Resonators,” *J. Sound Vib.*, vol. 329, no. 13, pp. 2547–2564, Jun. 2010.
[53]M. I. Younis and A. H. Nayfeh, “A Study of the Nonlinear Response of a Resonant Microbeam to an Electric Actuation,” *Nonlinear Dyn.*, vol. 31, no. 1, pp. 91–117, Jan. 2003.

[54] C. van der Avoort *et al.*, “Amplitude Saturation of MEMS Resonators Explained by Autoparametric Resonance,” *J. Micromechanics Microengineering*, vol. 20, no. 10, p. 105012, 2010.
[55] M. F. Daqaq, E. M. Abdel-Rahman, and A. H. Nayfeh, “Towards a Stable Low-Voltage Torsional Microscanner,” *Microsyst. Technol.*, vol. 14, no. 6, pp. 725–737, Jun. 2008.
[56] L. O. Thielman, S. Bennett, C. H. Barker, and M. E. Ash, “Proposed IEEE Coriolis Vibratory Gyro Standard and Other Inertial Sensor Standards,” in *2002 IEEE Position Location and Navigation Symposium (IEEE Cat. No.02CH37284)*, 2002, pp. 351–358.
[57] C. Acar, S. Eler, and A. M. Shkel, “Concept, Implementation, and Control of Wide Bandwidth MEMS Gyroscopes,” in *Proceedings of the 2001 American Control Conference. (Cat. No.01CH37148)*, 2001, vol. 2, pp. 1229–1234 vol.2.
[58] E. Netzer and I. Porat, “A Novel Vibratory Device for Angular Rate Measurement,” *J. Dyn. Syst. Meas. Control*, vol. 117, no. 4, pp. 585–591, Dec. 1995.
[59] A. A. Trusov, A. R. Schofield, and A. M. Shkel, “A Substrate Energy Dissipation Mechanism in In-Phase and Anti-Phase Micromachined z-axis Vibratory Gyroscopes,” *J. Micromechanics Microengineering*, vol. 18, no. 9, p. 095016, 2008.
[60] C. Acar and A. M. Shkel, “An Approach for Increasing Drive-Mode Bandwidth of MEMS Vibratory Gyroscopes,” *J. Microelectromechanical Syst.*, vol. 14, no. 3, pp. 520–528, Jun. 2005.
[61] D. Joachim and L. Lin, “Characterization of Selective Polysilicon Deposition for MEMS Resonator Tuning,” *J. Microelectromechanical Syst.*, vol. 12, no. 2, pp. 193–200, Apr. 2003.
[62] D. Joachim and L. Lin, “Selective Polysilicon Deposition for Frequency Tuning of MEMS Resonators,” in *Technical Digest. MEMS 2002 IEEE International Conference. Fifteenth IEEE International Conference on Micro Electro Mechanical Systems (Cat. No.02CH37266)*, 2002, pp. 727–730.
[63] K. Tanaka *et al.*, “A Micromachined Vibrating Gyroscope,” *Sens. Actuators Phys.*, vol. 50, no. 1, pp. 111–115, Aug. 1995.
[64] V. P. Veiko, “Laser-Assisted Microshaping,” in *Laser-Assisted Microtechnology 2000*, 2001, vol. 4157, pp. 93–105.
[65] T. Lam and R. B. Darling, “Modeling of Focused Ion Beam Trimming of Cantilever Beams,” in *In Proc. 3rd Int. Conf. Modeling and Simulation of Microsystems.*, 2000.
[66] T. Remtema and L. Lin, “Active Frequency Tuning for Micro Resonators by Localized Thermal Stressing Effects,” *Sens. Actuators Phys.*, vol. 91, no. 3, pp. 326–332, Jul. 2001.
[67] S. Park and R. Horowitz, “Adaptive Control for the Conventional Mode of Operation of MEMS Gyroscopes,” *J. Microelectromechanical Syst.*, vol. 12, no. 1, pp. 101–108, Feb. 2003.
[68] Y. Oh *et al.*, “A Surface-Micromachined Tunable Vibratory Gyroscope,” in *Proceedings IEEE The Tenth Annual International Workshop on Micro Electro Mechanical Systems. An Investigation of Micro Structures, Sensors, Actuators, Machines and Robots*, 1997, pp. 272–277.
[69] S. E. Alper and T. Akin, “A Symmetric Surface Micromachined Gyroscope with Decoupled Oscillation Modes,” *Sens. Actuators Phys.*, vol. 97–98, pp. 347–358, Apr. 2002.
[70] W. Geiger, B. Folkmer, U. Sobe, H. Sandmaier, and W. Lang, “New Designs of Dicromachined Vibrating Rate Gyroscopes with Decoupled Oscillation Modes,” *Sens. Actuators Phys.*, vol. 66, no. 1, pp. 118–124, Apr. 1998.
[71] Y. Mochida, M. Tamura, and K. Ohwada, “A Micromachined Vibrating Rate Gyroscope with Independent Beams for the Drive and Detection Modes,” *Sens. Actuators Phys.*, vol. 80, no. 2, pp. 170–178, Mar. 2000.

[72]F. Ayazi and K. Najafi, “A HARPSS Polysilicon Vibrating Ring Gyroscope,” *J. Microelectromechanical Syst.*, vol. 10, no. 2, pp. 169–179, Jun. 2001.
[73]S. S. Baek *et al.*, “A Symmetrical z-Axis Gyroscope with a High Aspect Ratio Using Simple and New Process,” in *Technical Digest. IEEE International MEMS 99 Conference. Twelfth IEEE International Conference on Micro Electro Mechanical Systems (Cat. No.99CH36291)*, 1999, pp. 612–617.
[74]W. Geiger *et al.*, “Decoupled Microgyros and the Design Principle DAVED,” *Sens. Actuators Phys.*, vol. 95, no. 2, pp. 239–249, Jan. 2002.
[75]C. Acar and A. M. Shkel, “Nonresonant Micromachined Gyroscopes with Structural Mode-Decoupling,” *IEEE Sens. J.*, vol. 3, no. 4, pp. 497–506, Aug. 2003.
[76]A. Sharma, M. F. Zaman, and F. Ayazi, “A Sub-0.2 deg/hr Bias Drift Micromechanical Silicon Gyroscope With Automatic CMOS Mode-Matching,” *IEEE J. Solid-State Circuits*, vol. 44, no. 5, pp. 1593–1608, May 2009.
[77]W. T. Sung, J. Y. Lee, J. G. Lee, and T. Kang, “Design and Fabrication of Anautomatic Mode Controlled Vibratory Gyroscope,” in *19th IEEE International Conference on Micro Electro Mechanical Systems*, 2006, pp. 674–677.
[78]S. Park, R. Horowitz, and C.-W. Tan, “Dynamics and Control of a MEMS Angle Measuring Gyroscope,” *Sens. Actuators Phys.*, vol. 144, no. 1, pp. 56–63, May 2008.
[79]S. Sung, W. T. Sung, C. Kim, S. Yun, and Y. J. Lee, “On the Mode-Matched Control of MEMS Vibratory Gyroscope via Phase-Domain Analysis and Design,” *IEEEASME Trans. Mechatron.*, vol. 14, no. 4, pp. 446–455, Aug. 2009.
[80]M. Fazlyab, M. Z. Pedram, H. Salarieh, and A. Alasty, “Parameter Estimation and Interval Type-2 Fuzzy Sliding Mode Control of a z-Axis MEMS Gyroscope,” *ISA Trans.*, vol. 52, no. 6, pp. 900–911, Nov. 2013.
[81]Y. X. Liu *et al.*, “Design of a Digital Closed Control Loop for the Sense Mode of a Mode-Matching MEMS Vibratory Gyroscope,” in *The 9th IEEE International Conference on Nano/Micro Engineered and Molecular Systems (NEMS)*, 2014, pp. 199–203.
[82]W.-T. Sung, J. G. Lee, J. W. Song, and T. Kang, “H-infinity Controller Design of MEMS Gyroscope and Its Performance Test,” in *PLANS 2004. Position Location and Navigation Symposium (IEEE Cat. No.04CH37556)*, 2004, pp. 63–69.
[83]Q. Zheng, L. Dong, D. H. Lee, and Z. Gao, “Active Disturbance Rejection Control for MEMS Gyroscopes,” in *2008 American Control Conference*, 2008, pp. 4425–4430.
[84]R. P. Leland, “Adaptive Control of a MEMS Gyroscope Using Lyapunov Methods,” *IEEE Trans. Control Syst. Technol.*, vol. 14, no. 2, pp. 278–283, Mar. 2006.
[85]S. Park, R. Horowitz, S. K. Hong, and Y. Nam, “Trajectory-Switching Algorithm for a MEMS Gyroscope,” *IEEE Trans. Instrum. Meas.*, vol. 56, no. 6, pp. 2561–2569, Dec. 2007.
[86]A. A. Trusov, I. P. Prikhodko, D. M. Rozelle, A. D. Meyer, and A. M. Shkel, “1 PPM Precision Self-Calibration of Scale Factor in MEMS Coriolis Vibratory Gyroscopes,” in *2013 Transducers Eurosensors XXVII: The 17th International Conference on Solid-State Sensors, Actuators and Microsystems (TRANSDUCERS EUROSENSORS XXVII)*, 2013, pp. 2531–2534.
[87]A. R. Schofield, A. A. Trusov, and A. M. Shkel, “Micromachined Gyroscope Design Allowing for Both Robust Wide-Bandwidth and Precision Mode-Matched Operation,” in *2008 IEEE Sensors*, 2008, pp. 654–657.
[88]A. R. Schofield, A. A. Trusov, and A. M. Shkel, “Multi-Degree of Freedom Tuning Fork Gyroscope Demonstrating Shock Rejection,” in *2007 IEEE Sensors*, 2007, pp. 120–123.

[89]K. Sahin, E. Sahin, S. E. Alper, and T. Akin, “A Wide-Bandwidth and High-Sensitivity Robust Microgyroscope,” *J. Micromechanics Microengineering*, vol. 19, no. 7, p. 074004, 2009.
[90]C. W. Tsai, K. h Chen, C. K. Shen, and J. c Tsai, “A MEMS Doubly Decoupled Gyroscope with Wide Driving Frequency Range,” *IEEE Trans. Ind. Electron.*, vol. 59, no. 12, pp. 4921–4929, Dec. 2012.
[91]W. Wang, X. Lv, and D. Xu, “Design of Multi-Degree-of-Freedom Micromachined Vibratory Gyroscope with Double Sense-Modes,” *Measurement*, vol. 58, pp. 6–11, Dec. 2014.
[92]A. Esmaeili, M. Aghanouri Kupaei, H. Faghihian, and H. R. Mirdamadi, “An Adaptable Broadband MEMS Vibratory Gyroscope by Simultaneous Optimization of Robustness and Sensitivity Parameters,” *Sens. Actuators Phys.*, vol. 206, pp. 132–137, Feb. 2014.
[93]C. Acar and A. M. Shkel, “Inherently Robust Micromachined Gyroscopes with 2-DOF Sense-Mode Oscillator,” *J. Microelectromechanical Syst.*, vol. 15, no. 2, pp. 380–387, Apr. 2006.
[94]M. Song, B. Zhou, T. Zhang, B. Hou, and R. Zhang, “Parametric Drive of a Micro Rate Integrating Gyroscope Using Discrete Electrodes,” in *2017 IEEE International Symposium on Inertial Sensors and Systems (INERTIAL)*, 2017, pp. 70–73.
[95]P. M. Polunin and S. W. Shaw, “Self-Induced Parametric Amplification in Ring Resonating Gyroscopes,” *Int. J. Non-Linear Mech.*, vol. 94, pp. 300–308, Sep. 2017.
[96]W. Zhang, R. Baskaran, and K. L. Turner, “Effect of Cubic Nonlinearity on Auto-Parametrically Amplified Resonant MEMS Mass Sensor,” *Sens. Actuators Phys.*, vol. 102, no. 1, pp. 139–150, Dec. 2002.
[97]L. A. Oropeza-Ramos, C. B. Burgner, and K. L. Turner, “Inherently Robust Micro Gyroscope Actuated by Parametric Resonance,” in *2008 IEEE 21st International Conference on Micro Electro Mechanical Systems*, 2008, pp. 872–875.
[98]L. A. Oropeza-Ramos and K. L. Turner, “Parametric Resonance Amplification in a MEMGyroscope,” in *IEEE Sensors, 2005.*, 2005, pp. 4 pp.-.
[99]M. Sharma, E. H. Sarraf, and E. Cretu, “Parametric Amplification/Damping in MEMS Gyroscopes,” in *2011 IEEE 24th International Conference on Micro Electro Mechanical Systems*, 2011, pp. 617–620.
[100] M. Sharma, E. H. Sarraf, R. Baskaran, and E. Cretu, “Parametric Resonance: Amplification and Damping in MEMS Gyroscopes,” *Sens. Actuators Phys.*, vol. 177, pp. 79–86, Apr. 2012.
[101] W. Zhang, R. Baskaran, and K. Turner, “Tuning the Dynamic Behavior of Parametric Resonance in a Micromechanical Oscillator,” *Appl. Phys. Lett.*, vol. 82, no. 1, pp. 130–132, Dec. 2002.
[102] A. Marzouk, “Utilization of Internal Resonance in Gyroscope Design,” Thesis, Applied Sciences: School of Mechatronic Systems Engineering, 2014.
[103] Ali H. Nayfeh and Dean T. Mook, *Nonlinear Oscillations*. Wiley.
[104] M. F. Golnaraghi, F. C. Moon, and R. H. Rand, “Resonance in a High-Speed Flexible-Arm Robot,” *Dyn. Stab. Syst.*, vol. 4, no. 3–4, pp. 169–188, Jan. 1989.
[105] W. K. Lee and H. D. Park, “Chaotic Dynamics of a Harmonically Excited Spring-Pendulum System with Internal Resonance,” *Nonlinear Dyn.*, vol. 14, no. 3, pp. 211–229, Nov. 1997.
[106] A. Alasty and R. Shabani, “Chaotic Motions and Fractal Basin Boundaries in Spring-Pendulum System,” *Nonlinear Anal. Real World Appl.*, vol. 7, no. 1, pp. 81–95, Feb. 2006.
[107] A. Vyas, “Microresonator Designs Based on Nonlinear 1:2 Internal Resonance Between Flexural-Flexural and Torsional -Flexural Structural Modes,” *Theses Diss. Available ProQuest*, pp. 1–213, Jan. 2008.

[108] A. Vyas, A. K. Bajaj, A. Raman, and D. Peroulis, “Nonlinear micromechanical filters based on internal resonance phenomenon,” in *Digest of Papers. 2006 Topical Meeting on Silicon Monolithic Integrated Circuits in RF Systems*, 2006, pp. 4 pp.-.
[109] S. W. Yoon, S. Lee, and K. Najafi, “Vibration-Induced Errors in MEMS Tuning Fork Gyroscopes,” *Sens. Actuators Phys.*, vol. 180, pp. 32–44, Jun. 2012.
[110] M. S. Weinberg and A. Kourepenis, “Error Sources in In-Plane Silicon Tuning-Fork MEMS Gyroscopes,” *J. Microelectromechanical Syst.*, vol. 15, no. 3, pp. 479–491, Jun. 2006.
[111] S.-R. Chiu, C.-Y. Sue, C.-H. Lin, and Y.-K. Su, “Dual-Axis Tuning Fork Vibratory Gyroscope with Anti-Phase Mode Vibration Mechanism,” *Microsyst. Technol.*, vol. 20, no. 12, pp. 2173–2184, Dec. 2014.
[112] “MIDIS Platform for Motion Sensors - Teledyne DALSA Inc.” [Online]. Available: http://www.teledynedalsa.com/semi/mems/applications/midis/. [Accessed: 02-Jun-2017].
[113] G. Xereas and V. P. Chodavarapu, “Ultraclean Wafer-Level Vacuum-Encapsulated Silicon Ring resonators for Timing and Frequency References,” *J. MicroNanolithography MEMS MOEMS*, vol. 15, no. 3, p. 035004, Sep. 2016.